A neuro-immune interface in glioblastoma

Dissertation
for
the doctoral degree of
Dr. rer. nat.

from the Faculty of Biology
University of Duisburg-Essen
Germany

Submitted by

Celia Christina Dobersalske

Born in Duisburg

July 2024

The experiments underlying the present work were conducted at the DKFZ-Division of Translational Neurooncology at the West German Cancer Center (WTZ), University Medicine Essen.

1. Examiner: Prof. Dr. Björn Scheffler
2. Examiner: Prof. Dr. Barbara Grünwald
3. Examiner: Prof. Dr. Guido Reifenberger

Chair of the Board of Examiners: Prof. Dr. Sven Brandau

Date of the oral examination: 30. Oktober 2024

Table of Contents

List of Abbreviations

5-ALA	5-aminolevulinic acid
AC	Astrocyte-like
APCs	Antigen-presenting cells
CAR	Chimeric antigen receptor
CB	Cranial bone
CCL5	CC-chemokine ligand 5
CNS	Central nervous system
CSF	Cerebrospinal fluid
CTLA4	Cytotoxic T lymphocyte-associated protein 4
CXCL12	C-X-C motif chemokine ligand 12
DCs	Dendritic cells
EGFR	Epidermal growth factor receptor
EGFRvIII	EGFR variant III
GB	Glioblastoma
Glymphatic	Glial-lymphatic
HSCs	Hematopoietic stem cells
HSPCs	Hematopoietic stem and progenitor cells
IDH	Isocitrate dehydrogenase
IDH-WT	IDH wild type
IDO	Indoleamine 2,3-dioxygenase
IL-10	Interleukin-10
IL-6	Interleukin-6
IL-8	Interleukin-8
MES	Mesenchymal-like
MGMT	O^6-methylguanine-DNA methyltransferase
MHC	Major histocompatibility complex
MRI	Magnetic resonance imaging
NPC	Neural progenitor-like
NSCLC	Non-small cell lung cancer
OPC	Oligodendrocyte progenitor-like
PD-L1	Programmed cell death ligand 1
PD1	Programmed cell death 1
PDGFR	Platelet-derived growth factor receptor
RTK	Receptor tyrosine kinases
scRNAseq	Single-cell RNA sequencing
SLYM	Subarachnoid lymphatic-like membrane
SOC	Standards of care
TAMs	Tumor associated macrophages
TCR	T cell receptor
TERT	Telomerase reverse transcriptase
TLS	Tertiary lymphoid structures

TME	Tumor microenvironment
TMZ	Temozolomide
WHO	World Health Organization

List of Figures

Summary

The treatment of glioblastoma needs groundbreaking advancements. Even with considerable progress in state-of-the-art techniques for most sophisticated molecular characterization of tumor tissue, the standard of care (SOC) in newly diagnosed disease has remained largely unchanged for decades.

In this work, we report the discovery of hematopoietic stem and progenitor cells (HSPCs) present in the brain parenchyma of patients with glioblastoma. Their accumulation within the tumor tissue correlated with worse clinical outcomes, and in *in-vitro* models of disease, we determined that physical contact of HSPCs with tumor cells facilitated the increase of tumor-promoting features. The unexpected presence of cellular progeny of the hematopoietic system in the brain tumor then instructed an investigation of their potential roots of origin at the central nervous system (CNS) borders.

Specifically, recent research has exposed guardian immune cells residing in the meninges, as well as around the dural venous sinus, and within the skull bone. As evident from preclinical models, these immune cells form a widespread yet local neuro-immune interface that responds to signals from the brain in conditions of injury or inflammation. This interface is connected via osseous liquor channels to the overlying cranial bone (CB), which acts as a locoregional source for immune cells of the meningeal sheets of the brain. The role of this structure in patients with glioblastoma, however, remains unknown. While searching for HSPCs, we discovered an unexpected niche of tumor-reactive, cytotoxic CD8$^+$ T lymphocytes in the CB. These immune cells are capable to recognize and to respond in an anti-tumoral manner to the tumor cells from the glioblastoma parenchyma.

It is remarkable that current SOC procedures in patients with brain tumors involve, as a first step of diagnosis and treatment, the disconnection of the CB. Our data suggest that this standard procedure may potentially harm the antitumor immune cell force. In light of these findings, future neoadjuvant settings of immunotherapies should be more focused on allowing the stimulation of potent cytotoxic immune responses before initiation of invasive treatment options.

Zusammenfassung

Die Behandlung von Patienten mit Glioblastom erfordert dringend grundlegende Fortschritte. Obwohl Verbesserungen aktueller Analysetechniken ein tieferes Verständnis der molekularen Zusammensetzung des Tumors ermöglichen, bleibt die Standardtherapie bei neu diagnostizierten Patienten mit Glioblastom größtenteils unverändert.

Im Rahmen unserer Studie, haben wir hämatopoetische Stamm- und Vorläuferzellen (*hematopoietic stem and progenitor cells*, HSPCs) im Gehirngewebe von Patienten mit Glioblastom nachgewiesen. Ihre Anhäufung im Tumorgewebe ist mit einer schlechteren Prognose assoziiert, und ihr direkter Kontakt mit Tumorzellen führte in *in-vitro* Ko-Kultur Modellen zu einer Erhöhung tumorunterstützender Faktoren. Die unerwartete Präsenz hämatopoetischer Vorläufer im Tumorparenchym initiierte Forschungsarbeiten zu ihrem potentiellen Ursprung an den Rändern des zentralen Nervensystems (ZNS).

Aktuelle Studien haben die Ansammlung von Wächterimmunzellen an den Rändern des ZNS beschrieben, in den Hirnhäuten, den großen venösen Blutleitern der Dura, oder im Schädelknochen. In präklinischen Modellen konnte gezeigt werden, dass diese Immunzellen ein lokales Netzwerk, das *neuro-immune interface*, bilden und auf Signale des Gehirns, wie Verletzungen oder Entzündungen, reagieren können. Dieses immunologische Netzwerk ist über knöcherne Liquor-Spalten mit dem darüber befindlichen kranialen Knochen (*cranial bone*, CB) verbunden, welcher als örtliche Quelle für Immunzellen der meningealen Hüllstrukturen des Gehirns dient. Die Rolle dieser Struktur bei Patienten mit Glioblastom ist jedoch unbekannt. Die Suche nach HSPCs offenbarte im CB eine unerwartete Nische tumorreaktiver, zytotoxischer CD8^{+} T-Lymphozyten, die in der Lage sind, Tumorzellen des Glioblastom-Parenchyms zu erkennen und anti-tumoral zu reagieren.

Es ist beachtenswert, dass das Standardvorgehen der Therapie von Patienten mit Hirntumoren die Durchtrennung der Knochenstruktur als ersten Schritt zur Diagnosesicherung und Tumorentfernung umfasst. Unsere Daten suggerieren, dass dieser Eingriff, die anti-tumoralen Immunzellen schädigen könnte. In Anbetracht unserer Ergebnisse sollte eine neoadjuvante Applikation von zukünftigen Immuntherapien bei neu-diagnostizierten Patienten mit Glioblastom intensiver untersucht werden, um vor der Initiierung invasiver Therapieoptionen eine potentiell potente zytotoxische Antwort von T-Zellen des CBs zu stimulieren.

Introduction

Glioblastoma

Glioblastoma (GB), the most common malignant brain cancer of the adult, presents with a pressing demand for innovative therapies. Despite aggressive standards of care (SOC), involving surgery, chemo- and targeted radiotherapy [1], as well as an optional use of tumor-treating fields [2, 3], patients show a median overall survival of only 15-21 months [1, 4, 5]. Currently, there are no standardized therapeutic approaches at the time of tumor relapse, which further darkens patient's outcome, with a 5-year survival rate noted below 7% [6, 7].

GB accounts for approximately half of all primary malignant brain tumors and typically manifests at the median age of 66, with a slight predominance in males [6]. Patients present with a wide range of neurological symptoms, such as visual field defects, seizures or headaches, depending on the location of the tumor [7, 8]. Contrast-enhanced magnetic resonance imaging (MRI) provides an overall picture of the primarily affected brain region, but less evident individual tumor cells also diffusely infiltrate the neighboring structures and surrounding brain tissue [9, 10]. The resulting extension of the tumor parenchyma beyond clearly distinguishable margins ultimately complicates surgical resection, even with advanced surgical techniques involving functional imaging, neuronavigation, awake craniotomy, and fluorescence-guided neurosurgery [11, 12]. The latter utilizes 5-aminolevulinic acid (5-ALA), a fluorescent metabolic precursor that accumulates in tumor cells, improving the distinction and delineation of tumor tissue under specific lighting conditions [13, 14]. This allows safe maximum resection to improve patient outcome [13, 15, 16], however, a complete removal of the tumor from the brain remains unachievable.

Immediately after resection, the tumor tissue is classified and graded by board-certified neuropathologists. The traditional diagnostic approach relied on histology identifying typical morphological features of GB, including tumor cell mitoses, microvascular proliferations, and focal necrosis. The most recent version of the World Health Organization (WHO) classification of central nervous system tumors [17] centers around molecular analyses, to extract data correlated with the clinical disease course. Isocitrate dehydrogenase (*IDH*) wildtype (IDH-WT) glioblastoma WHO grade 4 can be diagnosed by the presence of typical molecular features, such as mutations of the *IDH* 1/2 genes or the telomerase reverse transcriptase (*TERT*) promotor, amplification of the epidermal growth factor receptor (*EGFR*), as well as chromosome +7/-10 copy

number alterations, which together can outweigh histological observations and grading [17]. Furthermore, the methylation status of the DNA repair enzyme O^6-methylguanine-DNA methyltransferase (MGMT) remains a corner stone in the diagnostic guidelines [12, 17]. Its promotor methylation status serves as a prognostic and also as a predictive biomarker, as silencing of the *MGMT* repair gene is associated with a favorable outcome of patients with GB exposed to alkylating chemotherapy [1, 7].

Therapeutic interventions and immunotherapy

The SOC protocol for patients with newly-diagnosed glioblastoma, particularly at good physical health and under the age of 70 years, has remained largely unchanged for the last two decades. Patients undergo craniotomy for the classification and surgical resection of the tumor, followed by combined irradiation and a regimen of concomitant and adjuvant chemotherapy using the alkylating agent temozolomide (TMZ) [1, 12].

The lack of effective targeted treatment options for patients with newly diagnosed GB is surprising, considering the exhaustive genetic profiling that has been conducted in the past to uncover candidate therapeutic targets [18-21]. Research centers, for example, on the receptor tyrosine kinases (RTK) and their downstream signaling pathways, e.g. [22, 23]. Targets preferably considered within this strategy are mutated or aberrantly expressed in tumor cells, for example the EGFR or the platelet-derived growth factor receptor (PDGFR), both known for their critical roles in cellular proliferation and tumor propagation [20, 24, 25]. However, their targeting has not led to breakthrough treatment regimens, which was attributed to the abundant tumor heterogeneity that can be observed in GB [24, 26].

The introduction of immunotherapies has significantly transformed the SOC management of various malignant and advanced cancers. Strategies such as immune checkpoint blockade and tumor vaccines activate the patient's own immune cells, enhancing their ability to recognize and eliminate cancer cells perceived as foreign antigens [27, 28]. In the context of immune modulation, T lymphocytes, that is T cells, remain a subject of sustained interest, due to their pivotal role in the adaptive antitumor immune response [29]. Originating in the bone marrow, T cells mature in the thymus where they differentiate into CD4+ or CD8+ T cell classes, according to their affinity to the major histocompatibility complex (MHC) [30]. T cells carry a unique receptor on their surface, that was randomly generated by gene rearrangement [30]. To ensure that

the T cell receptor (TCR) specifically recognizes foreign antigens while preventing auto-reactivity, T cells undergo a positive and a negative selection process to ensure a functional immune response and induce self-tolerance [29, 30]. Following thymic selection, naïve T cells circulate in the periphery and can differentiate into distinct effector and memory T cell subsets upon antigenic threat [31]. Cancer immunity takes place as a cyclic process (Figure 1), which amplifies T cell responses in the process of anti-tumor surveillance [32, 33].
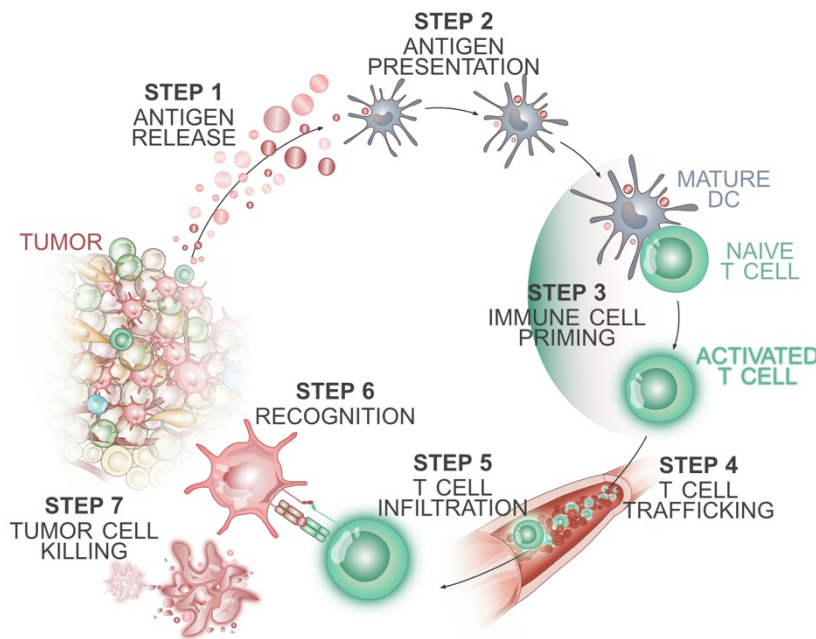

Figure 1: The cancer-immunity cycle; adapted from [32, 33]. The seven fundamental steps of cancer immunity, initiated by the release of tumor antigens and finally resulting in the destruction of cancer cells by activated, primed T cells.

Free peptide antigens, representing degraded tumor proteins, are captured by antigen-presenting cells (APCs) (Step 1). APCs, such as dendritic cells (DCs), elicit an immune response in presence of immunogenic signals, such as proinflammatory cytokines. Presentation of tumor peptides is carried out via the cell surface MHC class II or I molecules, recognized by CD4$^+$ or CD8$^+$ T cells, respectively (Step 2). The recognition by the specific TCR on the naïve T cell surface, along with co-stimulatory signals, is necessary for T cell activation and proliferation (Step 3). This process, also known as immune cell priming, can for example take place in tumor draining lymph nodes. Activated T cells would then traffic to the tumor (Step 4), where they infiltrate (Step 5), recognize, and bind to an individual tumor cell via the TCR (Step 6), and ultimately killing the target cell – and many more thereafter (Step 7) [32, 33].

The cancer-immunity cycle can be influenced by specific factors that either stimulate or inhibit immunity [29, 33]. Central negative regulators include inhibitory molecules or "checkpoints", circumventing T cell hyperactivation [29]. Among these negative regulators are prominent inhibitory molecules, which are also key targets in

immunotherapy, such as programmed cell death 1 (PD1) or cytotoxic T lymphocyte-associated protein 4 (CTLA4) [29]. Therapeutic administration of antibodies that block these immune regulatory checkpoints, e.g., PD-1 or its programmed cell death ligand 1 (PD-L1), have already entered clinical routine [34, 35]. Significantly improved survival rates in otherwise devastating cancers, like non-small cell lung cancer (NSCLC) [36], or melanoma [37] have raised hopes for a path of translation. However, checkpoint inhibition has, so far, not proven its promise in the treatment of glioblastoma [38, 39]. An alternative approach is the application of chimeric antigen receptor (CAR) T cells, which involves the re-engineering of the patient's own T cells outside the body (*ex vivo*) for subsequent re-introduction into the patient to target and destroy tumor cells in an antigen-dependent manner [40]. The approach of CAR T cells has successfully transitioned into the clinical treatment of hematological malignancies [41, 42], and it is thought to repeat its success in solid cancers, for example in extracranial tumors of the gastrointestinal tract [43] or in prostate cancer [44]. Pilot studies on CAR T cells in the clinical settings of malignant intracranial tumors, likewise, show promising first results, but tumor recurrence remains an issue [45, 46]. For example, a recent approach simultaneously targeting multiple GB surface antigens by combining a secreted T cell engaging antibody against EGFR and CAR T cells engineered against EGFR variant III (EGFRvIII), led to tumor progression in two out of three patients [47]. Taken together, even the most promising immunotherapeutic alternatives to current SOC treatments have not yet overcome the inherent challenges of intracranial clinical disease and the sophisticated resistance mechanisms characteristic of glioblastoma.

The tumor microenvironment in the context of therapy resistance

As gene sequencing technologies have advanced, traditional transcriptomic study in glioblastoma research transcended from bulk analysis towards more detailed single-cell RNA sequencing (scRNAseq) [48-50]. This technique facilitates an in-depth transcriptional characterization of thousands of individual cells from a unique sample, helping to dissect the complexity of the glioblastoma tumor microenvironment (TME) at initial diagnosis or at recurrence [49-51]. Albeit the original term "glioblastoma multiforme" has been outdated, the TME is highly heterogeneous, encompassing multiple cellular phenotypes, dynamic cellular states [48, 52, 53], and a wide range of infiltrating immune cells [50, 54].

A major component of therapy resistance in glioblastoma is thought to stem from an extensive inter- and intra-tumoral heterogeneity in glioblastoma. The tumor's neoplastic cellular population comprises a wide range of cancer cells, which can present with mutations or aberrant expression of cell surface receptors [24], as described in the previous section. Both, cellular plasticity and intra-tumor heterogeneity enable GB to quickly adapt to therapeutic challenges [24, 26]. The composition of tumor cell states in glioblastoma has been categorized into four major classes, namely, neural progenitor-like (NPC), oligodendrocyte progenitor-like (OPC), astrocyte-like (AC), and mesenchymal-like (MES) [48]. Current research has dissected this classification to extended detail, considering the spatial organization and the influence of therapeutic pressure [49, 52]. Intriguingly, it was reported, that tumor cells are embedded in local niches of stromal cells, contacting and merging with integrated networks of active neurons and astrocytes, and collectively contributing to treatment resistance and tumor progression [55, 56].

Despite these efforts, to dissect the neoplastic components and their synaptic integration within the TME, the overall advances in the field have not led to more effective strategies to therapeutically counter tumor heterogeneity on clinical grounds. Notably, immune cells residing in the microenvironment have also been identified as contributors to treatment failure [38, 39]. A substantial portion of the tumor mass consists of macrophages or brain-resident microglia [57, 58], collectively referred to as tumor-associated macrophages (TAMs), which can contribute to immunosuppression [38, 58, 59]. TAMs have been reported to drive T cell exhaustion considerably, a state that is characterized by decreased cytotoxic effector function, reduced proliferative capacity, and an upregulation of inhibitory receptors [60]. This cellular state can be induced, for example, by the secretion of immunosuppressive cytokines from TAMs, such as interleukin-10 (IL-10) [54, 61]. Not surprisingly, tumor cells actively add to this environment by the expression of additional immunosuppressive factors such as indoleamine 2,3-dioxygenase (IDO) [62] and by the upregulation of immune checkpoints like PD-L1 on their surface [63]. Collectively, immunological dysfunction in glioblastoma has been described as a consequence of immunosuppressive cytokines, an interaction of T cells with inhibitory surface molecules [39, 64], and as a result of systemic immunosuppression, evidenced by lymphopenia in glioblastoma patients [65]. The immunosuppressive state exposed by patients with glioblastoma has also been attributed to sequestration of T cells to the bone marrow, preventing their effective contribution to the antitumor immune response [66].

Immune cells play a fundamental role in the TME of patients with glioblastoma, either by directly mediating antitumor responses or, conversely, by contributing to an immunosuppressive environment. Yet, in terms of their recruitment, the involvement of tumor-adjacent structures, particularly the neuro-immune interface remains largely unexplored in the context of brain tumors.

The neuro-immune interface

The accessibility of the brain to immune cells has been subject of intense debate and (re-)interpretation [67-70]. The presence of the blood-brain barrier, restricting the access to the central nervous system (CNS), as well as the lack of evidence for a lymphatic system, contributed to the now rejected concept of immune privilege [39, 69].

The CNS is still regarded as immunologically distinct [38], as recent research provides evidence for the presence of guardian immune cells at the brain's borders [69]. These cells have been described in the choroid plexus, which produces the cerebrospinal fluid (CSF), in and around the dural sinus, and within the surrounding membranous layers, the meninges [67, 71-73]. Traditionally, the meninges have been considered to be comprised by the outer dura mater and the inner arachnoid and pia mater. However, attributed to the reinterpretation of brain immunity from mouse studies, the presence of a fourth meningeal layer, that is, the subarachnoid lymphatic-like membrane (SLYM) has been proposed [68]. It represents a local niche, hosting a substantial portion of immune cells and thereby contributing to the concentrated immune presence at the CNS borders [68, 69].

Based on accumulating evidence, it is proposed that guardian immune cells are replenished from the skull, which is directly connected to the underlying brain-surrounding meningeal sheets by osseous channels [74, 75]. The anatomical position of the immune cells allows them to directly respond to local signals. A mechanism that can be instructed through lymphatic [76] or CSF drainage [77] from the brain. Specifically, the glial-lymphatic (glymphatic) system, which is the CNS' waste clearance mechanism, facilitates the drainage of brain-derived antigens into the CSF [69, 77]. The drained CSF can furthermore directly access the skull bone marrow and locally instruct cranial hematopoiesis by mobilization of hematopoietic stem cells (HSCs) in response to brain-derived signals [78]. Immune cells then efflux from the

bone to replenish the immune cell niche within the meninges [75, 78, 79]. Together, the skull bone marrow and the meninges provide immune cells at the CNS borders that maintain homeostasis, or rapidly respond to local threats, such as inflammation and injury [68, 71, 74]. Despite our growing understanding of the immune surveillance in these conditions, we lack comprehensive knowledge about the role of the neuro-immune interface in malignant CNS tumors, such as glioblastoma.

Outline of the thesis

Glioblastoma remains a lethal disease, characterized by robust immunosuppressive properties of the tumor tissue and by a fundamental resistance to advanced immunotherapies. Despite substantial advancements in molecular diagnostics, and the adoption of state-of-the-art discovery tools, which have enhanced our understanding of the tumor's molecular landscape, therapeutic options have largely remained unchanged. The overall aim of this thesis was to unravel the yet uncharacterized spatial arrangement and composition of the immune system connecting the brain tumor to its adjacent borders. The underlying goal of the approach was to rethink starting points of immunotherapy treatment in glioblastoma, implementing recent preclinical findings on the brain's neuro-immune interface.

The first part of the thesis centers around the presence of hematopoietic stem and progenitor cells (HSPCs) within the tumor tissue of glioblastoma patients. To generate robust research hypotheses using publicly available datasets, this work is initiated with the development of Syllogist, a reference map-based deconvolution algorithm. Syllogist can be utilized to identify a broad range of immune cell types, including less abundant subtypes such as HSPCs. Through unbiased characterization of the cellular landscape inferred from bulk RNA sequencing data, a significant association of the HSPC signature with the high tumor grade of glioblastoma is found as part of this work. Presence and relevance of HSPCs are further confirmed in sophisticated *in-vitro* and *in-silico* experiments, ultimately revealing a positive correlation of HSPCs with immunosuppression and a negative association with patient outcome.

The second part of the thesis addresses recent advancements in the understanding of the neuro-immune interface. Previous research has focused on its role in immunosurveillance under physiological conditions or during brain inflammation. A potential disruption of the neuro-immune interface during CNS malignancy has not yet

been studied. There is no data available from tumor-models of disease, and there is no information on human intracranial tumors. This study investigates and uncovers yet uncharacterized immune cell populations adjacent to the tumor, specifically within the marrow of the cranial bone (CB). As part of a multidisciplinary approach, active, tumor-reactive CD8$^+$ T cell clonotypes are detected within the CB, which are also present in the tumor. In addition to mapping the trajectory of CD8$^+$ T cell differentiation within the bone, this work provides first evidence on the relevance of this niche for the progression-free survival of glioblastoma patients. Based on the collected evidence, it must be considered that the integrity of the CB, in close anatomical connection to the tumor, may be pivotal for future directions in glioblastoma immunotherapy.

Contributed Articles

The presented thesis consists of two original articles. In the context of this doctoral work, the following article was published in *Nature Communications*:

I. I-Na Lu*, **Celia Dobersalske***, Laurèl Rauschenbach, Sarah Teuber-Hanselmann, Anita Steinbach, Vivien Ullrich, Shruthi Prasad, Tobias Blau, Sied Kebir, Jens T. Siveke, Jürgen C. Becker, Ulrich Sure, Martin Glas, Björn Scheffler[#] & Igor Cima[#].

Tumor-associated hematopoietic stem and progenitor cells positively linked to glioblastoma progression. *Nature Communications* **12**, 3895 (2021). https://doi.org/10.1038/s41467-021-23995-z

* Contributed equally
[#] These authors jointly supervised

In the context of this doctoral work, the following article has been accepted for publication in *Nature Medicine*:

II. **Celia Dobersalske**, Laurèl Rauschenbach, Yichao Hua, Christoph Berliner, Anita Steinbach, Anika Grüneboom, Konstantinos D. Kokkaliaris, Dieter H. Heiland, Pia Berger, Sarah Langer, Chin L. Tan, Martin Stenzel, Somaya Landolsi, Flora Weber, Marvin Darkwah Oppong, Rudolf A. Werner, Hanah Gull, Thomas Schröder, Thomas Linsenmann, Andreas Buck, Matthias Gunzer, Martin Stuschke, Kathy Keyvani, Michael Forsting, Martin Glas, Jonathan Kipnis, Dennis A. Steindler, Hans Christian Reinhardt, Edward W. Green, Michael Platten, Alpaslan Tasdogan, Ken Herrmann, Florian Rambow[#], Igor Cima[#], Ulrich Sure[#], Björn Scheffler[#]

Cranioencephalic functional lymphoid units in glioblastoma. *Nature Medicine,* **accepted version**

[#] These authors jointly supervised

Cumulative Thesis/Extent of Contribution

Cumulative thesis of Ms. Celia Dobersalske

Author contributions

Title:

Tumor-associated hematopoietic stem and progenitor cells positively linked to glioblastoma progression

Authors:

I-Na Lu*, Celia Dobersalske*, Laurèl Rauschenbach, Sarah Teuber-Hanselmann, Anita Steinbach, Vivien Ullrich, Shruthi Prasad, Tobias Blau, Sied Kebir, Jens T. Siveke, Jürgen C. Becker, Ulrich Sure, Martin Glas, Björn Scheffler[#] & Igor Cima[#]

* Contributed equally

[#] These authors jointly supervised

Contributions:

- Conception - 50%: Contributed to the conception of Syllogist at initial stages of work, conception of experiments during revision of the work

- Conduction of experimental work - 50%: Bioinformatics and data processing, Immunofluorescence and immunohistochemistry, Flow cytometry, scRNAseq, and in-vitro experiments

- Data analysis - 50%: Analysis and interpretation of conducted experimental work

- Species identification – n/a

- Statistical analysis - 25%: Statistical analysis of collected experimental data

- Writing the manuscript - 50%: Original manuscript draft and editing

- Revision of the manuscript - 80%: Conducted experimental work, manuscript writing and editing during revision of the manuscript, creation of all figures

_____   _____
Signature of the Doctoral Candidate   Signature of the Doctoral Supervisor

ARTICLE

Check for updates

Tumor-associated hematopoietic stem and progenitor cells positively linked to glioblastoma progression

I-Na Lu[1,2,3,11], Celia Dobersalske [1,2,3,11], Laurèl Rauschenbach [1,3,4], Sarah Teuber-Hanselmann[5], Anita Steinbach[1,2,3], Vivien Ullrich[1,2,3], Shruthi Prasad[1,2,3], Tobias Blau[5], Sied Kebir[1,3,6], Jens T. Siveke[2,3,7,8], Jürgen C. Becker[2,3,9], Ulrich Sure[3,4], Martin Glas[1,3,6], Björn Scheffler [1,2,3,10,12] & Igor Cima [1,2,3,12✉]

Brain tumors are typically immunosuppressive and refractory to immunotherapies for reasons that remain poorly understood. The unbiased profiling of immune cell types in the tumor microenvironment may reveal immunologic networks affecting therapy and course of disease. Here we identify and validate the presence of hematopoietic stem and progenitor cells (HSPCs) within glioblastoma tissues. Furthermore, we demonstrate a positive link of tumor-associated HSPCs with malignant and immunosuppressive phenotypes. Compared to the medullary hematopoietic compartment, tumor-associated HSPCs contain a higher fraction of immunophenotypically and transcriptomically immature, CD38- cells, such as hematopoietic stem cells and multipotent progenitors, express genes related to glioblastoma progression and display signatures of active cell cycle phases. When cultured ex vivo, tumor-associated HSPCs form myeloid colonies, suggesting potential in situ myelopoiesis. In experimental models, HSPCs promote tumor cell proliferation, expression of the immune checkpoint PD-L1 and secretion of tumor promoting cytokines such as IL-6, IL-8 and CCL2, indicating concomitant support of both malignancy and immunosuppression. In patients, the amount of tumor-associated HSPCs in tumor tissues is prognostic for patient survival and correlates with immunosuppressive phenotypes. These findings identify an important element in the complex landscape of glioblastoma that may serve as a target for brain tumor immunotherapies.

[1] DKFZ-Division Translational Neurooncology at the West German Cancer Center (WTZ), University Hospital Essen/University of Duisburg-Essen, Essen, Germany. [2] German Cancer Research Center (DKFZ), Heidelberg, Germany. [3] German Cancer Consortium (DKTK), Partner site Essen/Düsseldorf, Germany. [4] Department of Neurosurgery and Spine Surgery, University Hospital Essen, Essen, Germany. [5] Institute of Neuropathology, University Hospital Essen, Essen, Germany. [6] Division of Clinical Neurooncology, Department of Neurology, University Hospital Essen, Essen, Germany. [7] Bridge Institute of Experimental Tumor Therapy, West German Cancer Center, University Hospital Essen, Essen, Germany. [8] DKFZ-Division of Solid Tumor Translational Oncology, West German Cancer Center, University Hospital Essen, Essen, Germany. [9] Translational Skin Cancer Research (TSCR), Department of Dermatology, University Medicine Essen, Essen, Germany. [10] Center of Medical Biotechnology (ZMB), University of Duisburg-Essen, Essen, Germany. [11] These authors contributed equally: I-Na Lu, Celia Dobersalske [12] These authors jointly supervised: Björn Scheffler, Igor Cima. ✉email: i.cima@dkfz.de

Glioblastoma is the most aggressive brain malignancy in adults, lacking effective treatments and leading to death within a median duration of 15–20 months after diagnosis, despite standard combination of surgery, radio- and chemotherapy[1,2]. Cancer immunotherapy, which aims to prime or boost the body's immune system against cancer cells, may improve the clinical course of glioblastoma. Targeting immune checkpoints in advanced malignancies such as melanoma, kidney and lung cancer, achieved impressive therapeutic effects, sparking new hopes for the treatment of brain tumors[3,4]. However, the glioblastoma microenvironment is characteristically immunosuppressive compared to other malignancies, owing to, at least in part, potent immunosuppressive cytokines such as TGF-β and IL-10[5], negative regulators of effector cell functions such as programmed death-ligand 1 (PD-L1), indoleamine 2,3-dioxygenase (IDO) and oncometabolites such as (R)-2-hydroxyglutarate[6,7]. Accordingly, the use of anti-PD-1 antibodies in recurrent glioblastoma failed to prolong patient overall survival[8]. Transfusion of a single dose of chimeric antigen receptor (CAR) T cells targeting EGFRvIII led to adaptive immunosuppression and therapy failure, indicating that the major barrier for immunotherapy of glioblastoma may lie on the inhibitory tumor microenvironment[9]. Nevertheless, Brown and colleagues observed sustained clinical response for 7.5 months in a patient with highly aggressive recurrent glioblastoma, after application of CAR T cells targeting interleukin-13 receptor alpha 2 (IL13Rα2)[10]. Further, a preliminary report on a phase III clinical trial of dendritic cell vaccine in glioblastoma patients reported a median overall survival of 23.1 months, compared to the 15–20 months achieved with the current standard of care[11] These studies remarkably document the challenging endeavors of immunotherapy in the treatment of glioblastoma.

The brain tumor immunosuppressive microenvironment is marked by the presence of several immune cell types including regulatory T cells and myeloid cells such as bone marrow-derived macrophages lacking T cell co-stimulatory molecules[5]. Glioblastoma-associated immune cells may not only create an immunosuppressive microenvironment but also directly promote malignancy[3,12]. For example, tumor-infiltrating neutrophils facilitated cancer stem cell accumulation through S100A4[13]. Despite efforts in decoding the complexity of the immune system's modus operandi during brain tumor progression, interactions between different cell types in glioblastoma are not yet fully understood. Moreover, knowledge aimed at modulating the immune system therapeutically and in a patient-specific setting is lacking. The systematic, discovery-driven screening of immune cell types in glioblastoma may help to uncover important immunologic targets and lead to the discovery of predictors of clinical outcomes.

Recent studies point in this direction: For example, Gentles et al.[14] profiled the occurrence of 18 distinct immune cell types in various cancer types, revealing unknown links of immune cell types with clinical outcomes. In brain cancers, the relative leukocyte composition was significantly different compared to non-brain solid tumors as exemplified by a decrease in B cell subsets and an increase of monocyte and neutrophil proportions. Furthermore, this report highlighted the discovery of favorable and adverse outcomes for various cell subsets in glioblastoma, demonstrating the benefits of a discovery-driven screening approach in the analysis of the tumor microenvironment.

Here, we have profiled the cellular landscape of brain cancers using a computational approach for transcriptome analysis, separating the signals of 43 different cell types, including 26 distinct immune cell types. We uncover and validate the presence of hematopoietic stem and progenitor cells within brain tumor samples and demonstrate a positive association of this cell population with glioblastoma malignancy and immunosuppression.

Results

Estimating the relative abundance of cell types using transcriptomes. To infer the cellular landscape of brain tumor tissues from transcriptome data, we established Syllogist, a reference-based algorithm for cell type estimation (Fig. 1a, Methods). To this end, we employed a validated gene expression matrix containing cell type-specific transcriptomes[15]. We next extracted data for 43 different cell types, including a selection of 26 immune cell types, similarly to previous studies[16,17]. For each cell type we determined a signature of the top 80 specific genes by calculating specificity indices based on a Shannon entropy-based statistic introduced by Shug et al.[18] (Supplementary Data 1). We next computed the presence of each 80-gene signature in query transcriptomes and compared them with a null model comprising 1000 simulations by Fisher's exact test. The resulting odds ratios were used as proxy for the relative amount of a target cell type to be compared between samples (intersample comparison). The algorithm was validated using a set of previously published positive controls. Each positive control produced specific signals in the corresponding reference samples but not in cells from different ontogenies (Fig. 1b). We also analyzed specific cell types that were not directly represented by our references. For example, freshly isolated glioblastoma cells were specifically assigned to the astrocytic references and neurons to the neuronal lineages. Cancer-associated fibroblasts (CAFs) were distinct from normal fibroblasts and their signals associated with mesenchymal stem cell signatures. Microglia-derived transcriptomes associated with both monocyte and macrophage references (Supplementary Fig. 1).

To test the performance of Syllogist and benchmark it with reported computational methods, we investigated publicly available transcriptome datasets with available paired immunophenotyping data[19]. To this end, we analyzed publicly available PBMC transcriptomes with paired mass cytometry data of 24 immune cell subsets that were previously used for the validation of a similar cell type estimation method[20]. When correlating cell type signals with immunophenotyping data, Syllogist performed similarly to CIBERSORT[21], xCell[20], QuanTIseq[22] and EPIC[23] on 8 commonly detected immune cell subsets (Fig. 1c). In addition, Syllogist performed similarly to all tested methods in estimating CD4 and CD8 T cell subsets in transcriptome data of melanoma and lung cancer tissues paired with quantitative immunofluorescence data[22] (Fig. 1d). To benchmark Syllogist with other established methods for the analysis of brain tissue transcriptomes, we quantified common cell types for all methods and compared the results using correlation matrices for each cell type. This analysis showed that Syllogist was always in agreement with at least two other methods (Fig. 1e).

To specifically interrogate intersample differences in brain tissue cellular composition, we performed 2-sample paired comparisons between 100 brain tissue transcriptomes[24] with and without in silico spike-in transcriptomes for various immune cell types at various ratios (Fig. 1f). A selected number of cell types could be detected at percentages down to 0.05%. For example, brain samples with 0.05% in silico-spiked plasmacytoid dendritic cell (pDC) or naïve CD4 T cell transcriptomes were significantly different from the same brain transcriptomes without spiking. On the other hand, cell types such as naïve B cells could only be detected when spiked at frequencies above 0.8% (Fig. 1f).

These results indicate that Syllogist is able to estimate the relative quantity of 43 distinct cell types from bulk RNA sequencing data. Our algorithm performs similarly to known deconvolution and gene enrichment methods[20–23] in intersample comparisons and it can detect the relative amount of cell types in brain tissue transcriptomes with a limit of detection below 1% when using 2-sample hypothesis testing.
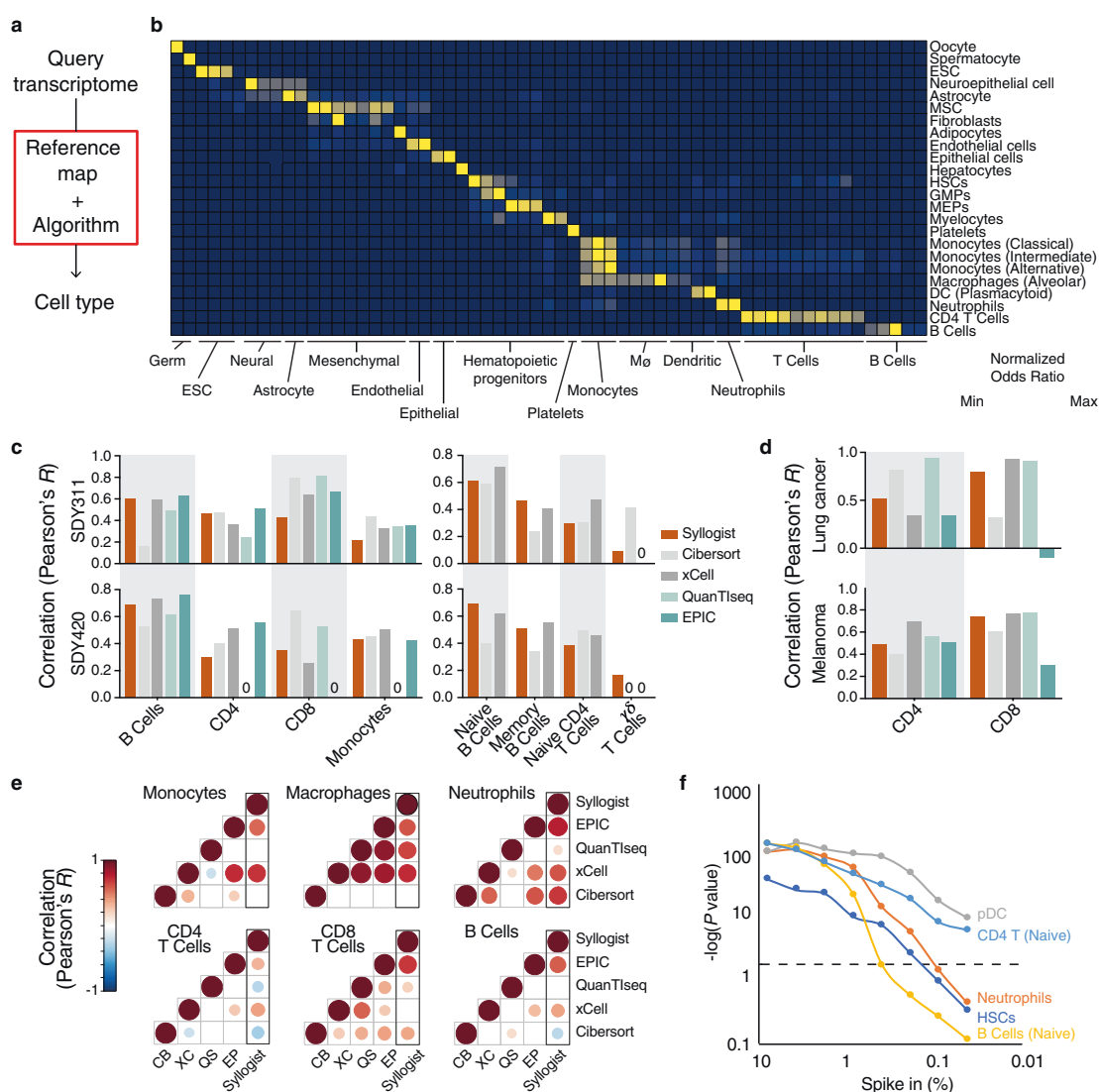
Fig. 1 Cell type estimation using transcriptomes. a Simplified workflow of Syllogist for detection and relative quantitation of cell types from bulk tissue transcriptomes. **b** Heat map comparing the number of genes enriched for each published positive control sample (rows) and cell type (columns) over random enrichment. Each colored box represents a normalized odds ratio of the respective Fisher's exact test ranging from 0 (blue) to 1 (yellow). ESC Embryonic stem cell, MSC Mesenchymal stem cell, HSCs Hematopoietic stem cells, GMPs Granulocyte–monocyte progenitors, MEPs Megakaryocyte–erythroid progenitors, DC Dendritic cell. **c** Comparison of Syllogist with CIBERSORT, xCell, QuanTIseq and EPIC. Bar plots represent the Pearson correlation coefficients calculated by comparing the Syllogist odds ratios, the CIBERSORT, xCell, QuanTIseq, and EPIC scores with the quantitative data of PBMC fractions measured by CyTOF (SDY311 [https://www.immport.org/shared/study/SDY311], $n = 61$ patients and SDY420 [https://www.immport.org/shared/study/SDY420], $n = 104$)[19]. **d** same as (**c**), applying melanoma ($n = 32$ samples) and lung cancer ($n = 8$) datasets with paired quantitative data of CD4 and CD8 T cells by immunofluorescence[22]. **e** Correlation matrices represent the agreement of Syllogist with four established computational methods for the indicated immune cell types. Pearson correlation coefficients with $p < 0.05$ are shown as circles, with circle size and color matching Pearson correlation coefficients from −1 (blue) to 1 (dark red). Empty squares represent correlation coefficients of $p \geq 0.05$. CB Cibersort; QS QuanTIseq, XC xCell, EP EPIC. p values determined using a two-tailed Student's t-test. **f** Line chart represents −log10 (p values) obtained by comparing paired samples with and without spike-in for the indicated cell types at various percent spike-in ($n = 200$ brain tissue transcriptomes, two-tailed paired Student's t-test). pDC plasmacytoid dendritic cells, HSCs Hematopoietic stem cells. The horizontal dashed line indicates the threshold considered for significance ($p = 0.05$). Source data of (**c**), (**d**) and (**f**) are provided as a Source Data file.
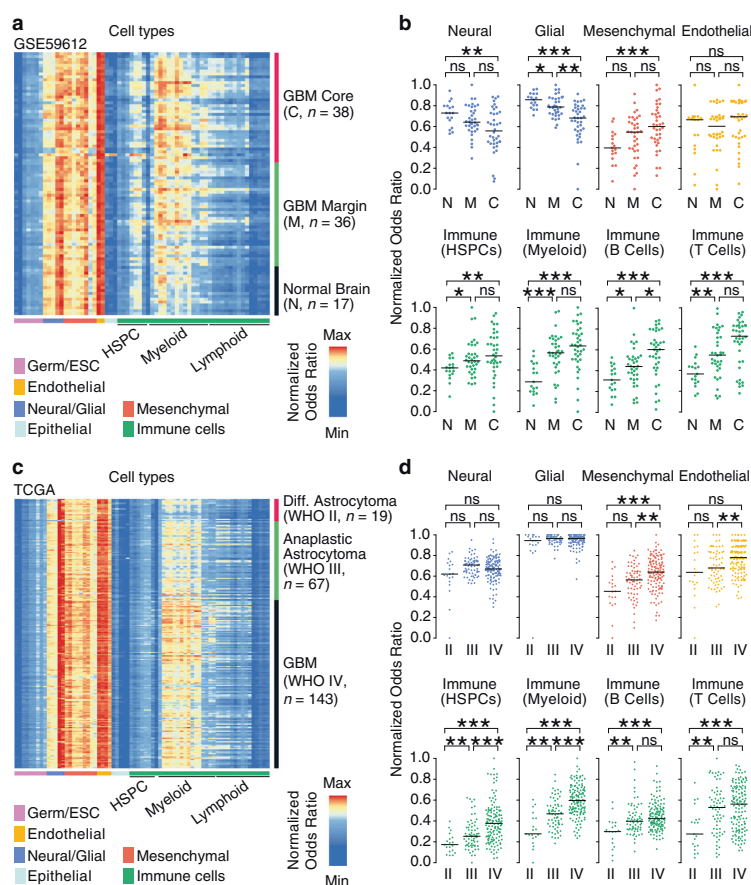
Fig. 2 HSPCs are enriched in glioblastoma and associate with tumor grade. a Heatmap represents Syllogist signals for each cell type (columns) and patient samples (rows) for data derived from Gill et al.[26], including core, margin and normal brain tissue samples ($n = 91$ samples). GBM Glioblastoma, HSPC Hematopoietic stem and progenitor cell, ESC Embryonic stem cell, Mø Macrophages. **b** Association of brain sample locations with Syllogist normalized odds ratios of eight selected cellular compartments. Dot plots represent the samples from normal brains (N, $n = 17$ samples), glioblastoma margins (M, $n = 36$), and cores (C, $n = 38$). **c** Heatmap represents Syllogist signals for each cell type (columns) and patient samples for the LGG-glioblastoma cohorts[29,30] ($n = 229$ samples). **d** Association of tumor grade with normalized odds ratios of eight main cellular compartments. Dot plots represent the samples from diffuse astrocytoma (WHO grade II, $n = 19$ samples), anaplastic astrocytoma (WHO grade III, $n = 67$) and glioblastoma (WHO grade IV, $n = 143$). p values were determined by 2-tailed, unpaired Student's t-test with correction by the Benjamini–Hochberg procedure. *, $p < 0.05$; **, $p < 0.01$; ***, $p < 0.001$; ns not significant. For (**b**) and (**d**), the exact p values are reported in Supplementary Data 2 and 3, respectively. Source data of (**b**) and (**d**) are provided as a Source Data file.

The cellular landscape of brain tumors. Residual tumor cells in glioblastoma remain consistently scattered beyond the surgical margin, facilitating rapid recurrence of disease[25]. The study of glioma cells and their microenvironment at the surgical margin is therefore of utmost clinical relevance as this region represents the target of post-surgical therapies, including immunotherapies. We were therefore interested in profiling the cellular landscapes of glioblastoma cores and their margins. To this end, we used the dataset from Gill et al.[26], which includes samples from both tumor centers and margins, as well as normal brain samples. In tumor cores ($n = 38$ samples) and margins ($n = 36$) we observed an increase in myeloid and lymphoid cell types compared to normal brains ($n = 17$), matched by a decrease in neural and glial cell proportions (Fig. 2a, b and Supplementary Data 2). Surprisingly, we also detected increasing signals derived from hematopoietic stem and progenitor cells (HSPCs) in the tumor margins and cores compared to normal brains ($p = 0.018$ and $p = 0.005$,

respectively, Student's t-test) indicating that HSPCs might reside in glioblastoma cores and margins (Fig. 2b). For example, among HSPC subsets, we observed an enrichment of hematopoietic stem cells (HSC, $p = 0.024$), granulocyte-monocyte progenitors (GMP, $p = 0.009$), promyelocytes ($p = 0.009$) and myelocytes ($p = 1.46 \times 10^{-5}$) in the glioblastoma margins compared to normal brains. Enrichment of HSPC subsets were also significant in the glioblastoma cores compared to normal brains (HSC, $p = 0.022$, GMP, $p = 0.001$, promyelocytes ($p = 0.0006$) and myelocytes, $p = 4.83 \times 10^{-6}$) (Supplementary Fig. 2a and Supplementary Data 2). Based on these results we hypothesize that HSPCs infiltrate glioblastoma and are enriched not only at the tumor cores but also at their margins. These cells may, therefore, persist in the postsurgical cavity after resection.

The pathology of lower grade isocitrate dehydrogenase (*IDH*) wildtype astrocytoma is difficult to interpret, because *IDH* wildtype diffuse or anaplastic astrocytomas (WHO grade II and

III, respectively) may have clinical courses similar to glioblastoma (WHO grade IV)[27,28]. We were therefore interested in profiling the cellular landscape of these tumors by analyzing the cell type content of the TCGA lower grade glioma (LGG) and glioblastoma cohorts[29,30]. We identified 19 diffuse astrocytomas, 67 anaplastic astrocytomas and 143 glioblastomas, all harboring *IDH1/2* wildtype genotypes. In this data, we detected several differences in the cellular landscapes of astrocytomas between WHO grades (Fig. 2c, d and Supplementary Data 3) and once more, we detected signals derived from various HSPC subsets. In glioblastoma, HSPC signals were significantly higher compared to grade II and III astrocytomas ($p = 2.14 \times 10^{-7}$, and $p = 5.84 \times 10^{-6}$, respectively) (Fig. 2d). In particular, we observed an enrichment of HSCs ($p = 2.82 \times 10^{-7}$), GMPs ($p = 5.68 \times 10^{-7}$), common myeloid progenitors (CMP, $p = 2.34 \times 10^{-5}$), promyelocytes ($p = 2.49 \times 10^{-5}$), myelocytes ($p = 3.55 \times 10^{-6}$) and megakaryocyte–erythroid progenitors (MEP, $p = 0.041$) in glioblastoma compared to grade III tumors. Similar results were obtained when comparing glioblastoma vs grade II tumors (Supplementary Fig. 2b and Supplementary Data 3). A specific subset of myeloid-derived suppressor cells characterized by a phenotype of immature or "early stage" myeloid cells (eMDSCs, Lin⁻HLA-DR⁻CD33⁺)[31] may be responsible, at least in part, for signals detected in the HSPC compartment by Syllogist. However, eMDSCs associated uniquely with the CD14⁺ monocyte references and not with progenitors of the hematopoietic lineages (Supplementary Fig. 3).

Together, we profiled 43 different cell types in 217 glioblastomas, 86 WHO grade II and III astrocytomas and 17 normal brain tissue samples by gene enrichment analysis. Our results indicate that several HSPC subsets, while expected to reside in the bone marrow or the peripheral blood[32], are detected in brain tumors at their cores and margins. In addition, HSPC signals positively associate with the presence and histological grade of brain tumors.

HSPCs populate brain tumor tissues. The detection of endogenous hematopoietic progenitors in human brain tissues represents an intriguing finding which, to our knowledge, has not yet been reported. To test if HSPCs can be identified in glioblastoma tissues by classical immunofluorescence, we determined the status of CD34 and CD45 in paraffin embedded formalin fixed glioblastoma tissues ($n = 4$ patients). In all patients, we detected CD45⁺CD34⁺ double positive cells (Fig. 3a). To further study HSPCs in brain tumors, we analyzed a set of 12 fresh surgical tissue samples derived from 12 patients using flow cytometry (7 primary *IDH* wildtype glioblastoma tissues, 4 lower grade gliomas and 1 non-small cell lung cancer brain metastasis, Supplementary Data 4). We interrogated the presence of 7 HSPC subsets[33] in cell suspensions obtained from these tissues and compared them with healthy bone marrow-derived mononuclear cells. All samples stained positive for HSPCs as defined by lineage (Lin) negative and CD34 positive events (Fig. 3b–d). In glioblastoma tissues, we detected a median of 1813 Lin⁻CD34⁺ HSPCs per million cells analyzed (range $n = 525$–8882); In lower grade glioma samples, 1617 HSPCs per million ($n = 47$–2707) in the metastatic sample we observed 296 HSPCs per million, compared to 7933 HSPCs per million derived from a healthy donor bone marrow sample (Fig. 3d). Interestingly, we observed a notable lineage bias of HSPC subsets in glioblastoma compared to bone marrow-derived mononuclear cells or lower grade gliomas. In glioblastoma samples we recorded an increase in hematopoietic stem cell proportions (HSCs, Lin⁻CD34⁺CD38⁻CD45RA⁻CD90⁺) ranging from 43.0% to 67.5% of total HSPCs compared to 2.6–23.6 % in lower grade gliomas ($p = 4.83 \times 10^{-4}$, two-tailed Student's *t*-test) and

1.9% in the bone marrow sample (Fig. 3d). Multipotent progenitors (MPPs), defined by the expression of Lin⁻CD34⁺CD38⁻CD45RA⁻CD90⁻ were also overrepresented in brain tumor tissues compared to the healthy bone marrow sample. These results indicated that immature HSPC subsets, in particular HSCs and MPPs, were enriched in glioma tissue samples and a brain metastasis sample (Fig. 3d). These data were also in line with the detection limit of Syllogist for HSCs reported in Fig. 1f (~1200 cells/million). In addition, our results were not biased by contamination from circulating HSPCs, as the proportion of HSCs in glioblastoma tissue cell suspensions was 4–37.5 fold higher compared to the known proportion of HSCs in the peripheral blood mononuclear cells[34]. Analysis of circulating and tissue-associated HSCs from paired samples confirmed this enrichment ($n = 2$ samples from one patient, Supplementary Fig. 4a). Also, the presence of non-hematopoietic progenitors expressing CD34 such as endothelial and tumor cells[35,36] may have been excluded from our analysis by lineage markers such as CD14[37,38] or CD56[39,40]. In this line, adding an endothelial-specific antibody in our lineage cocktail (anti-CD144) did not change the flow cytometric profiles of HSPCs in glioblastoma cell suspensions (Supplementary Fig. 4b). Similarly, the preferential accumulation of immature HSPC subsets in glioblastoma samples could also be observed when gating for CD45 positive cells to exclude potential contaminants of non-hematopoietic origin (Supplementary Fig. 4c). We next asked if HSPCs could be detected in a publicly available dataset of single cell RNA-Seq from glioblastoma patients[41]. In all samples analyzed, we annotated various HSPC subsets, in particular HSCs and MEPs. Interestingly, in accordance to the flow cytometric profiles, we also noted increased proportions of immature progenitors compared to two healthy bone marrow samples[42] used as positive controls (Supplementary Fig. 4d).

To test the proliferative capacity and lineage commitment of tumor-associated HSPCs, we performed colony-forming cell (CFC) assays using cell suspensions derived from 14 brain tumor surgical specimens cultured in semi-solid media (eight glioblastomas, four lower grade gliomas, and two brain metastases, Supplementary Data 4). We observed hematopoietic colonies in 7/8 glioblastoma patient specimens (median, $n = 6.5$ colonies/sample, range, $n = 0$–13), whereas colonies derived from lower grade gliomas or metastasis could be observed only in 1 ganglioglioma case (median $n = 0$, range $n = 0$–2) (Fig. 3e, f). In glioblastoma-derived cultures we observed a spectrum of CFU-GEMM, CFU-GM and BFU-E colonies, confirming that HSPCs from brain tumor tissues can proliferate and differentiate into myeloid lineages (including erythroid cells). This data supported again our earlier observations consistently indicating the presence of HSPCs in glioblastoma. Furthermore, the colony-forming activity was significantly higher in glioblastoma compared to the non-glioblastoma tumor entities ($p = 0.025$, Fisher's exact test) (Fig. 3f). Moreover, CFU-GEMM colonies, which derive from more primitive HSPCs, were detected exclusively in glioblastoma-derived cultures (Fig. 3f), indicating the presence of more immature HSPC subsets in glioblastoma samples compared to other brain tumor entities. These results were also in agreement with the flow cytometry data reported in Fig. 3d, showing an enrichment of immature hematopoietic progenitors within the glioblastoma microenvironment.

To test if tumor-associated HSPCs displayed similar potency between patients, we selected glioblastoma samples with similar flow cytometric HSPC profiles (Fig. 3d, Patient 3, 8 and 14) and compared their colony formation ex vivo (Fig. 3f). All three patients produced distinct CFC profiles under identical conditions, suggesting heterogeneous potency of tumor associated HSPCs in vivo.
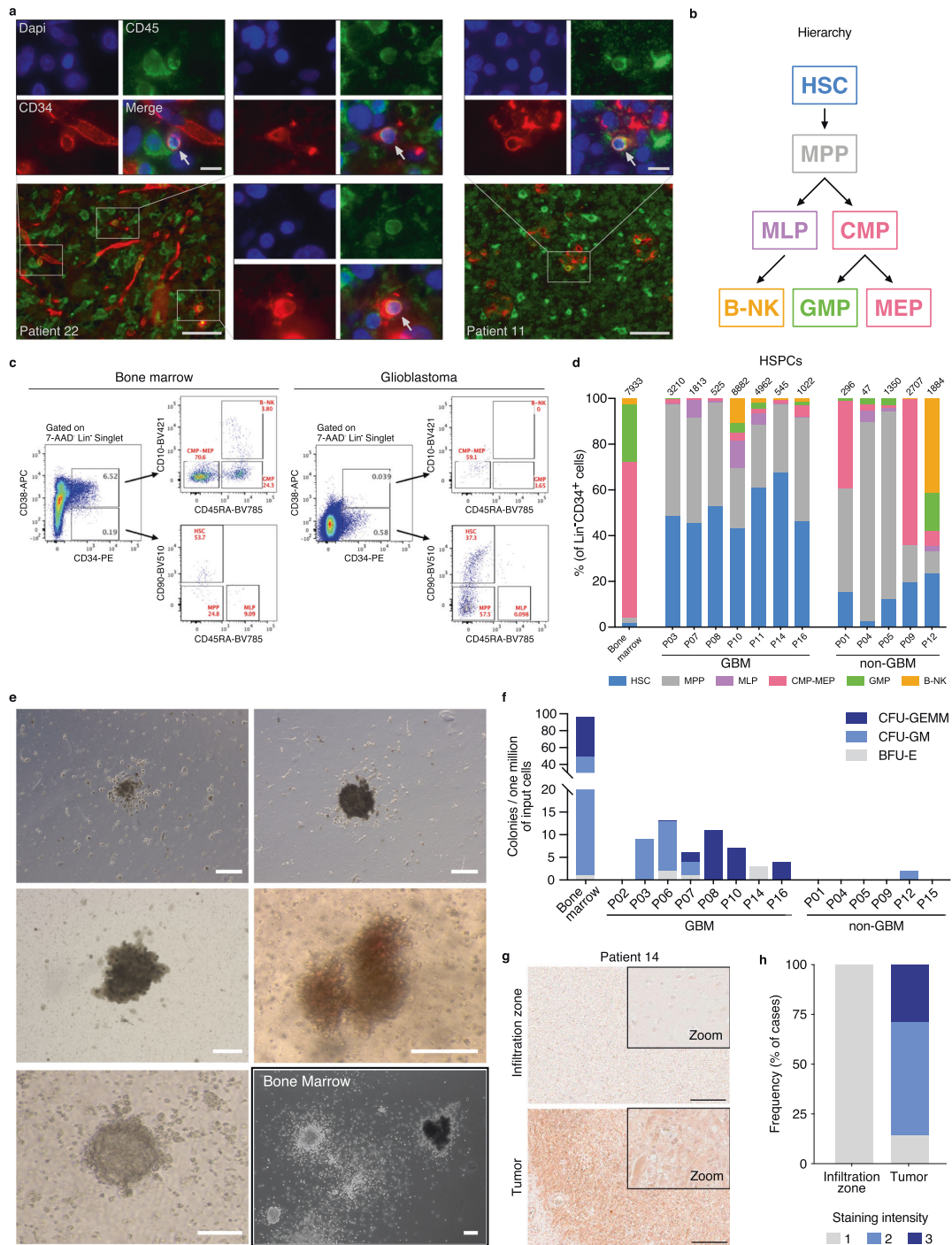
The lineage fate and function of HSPCs in the bone marrow depend on specialized factors such as the CXC chemokine ligand (CXCL) 12, which signals through the CXCR4 receptor to induce HSPC niche colonization, proliferation and differentiation[43]. To test if tumor-associated HSPCs reside in a similar microenvironment, we examined CXCL12 expression in tissue sections from 7

glioblastoma patients, in both the tumor core and the infiltration zone by immunohistochemistry. We observed increased CXCL12 expression in 6/7 glioblastoma tumor cores compared to the peripheral infiltration zone in the same section (Fig. 3g, h). Specifically, CXCL12 was prominently detected in tumor cells with uniform staining patterns within samples. Tumor cells may

Fig. 3 Characterization of tumor-associated HSPCs in human glioblastoma tissues. a Representative immunofluorescence appearance of CD34$^+$ (red)/ CD45$^+$ (green) cells (arrows) in formalin-fixed, paraffin-embedded glioblastoma tissue sections from two patients (out of four analyzed, all with similar results). Nuclei were counterstained with DAPI (blue). Scale bars = 50 μm (overview) and 10 μm (insets). **b** Diagram describes the hierarchy of HSPC subsets analyzed in this study by flow cytometry. HSC Hematopoietic stem cell, MPP Multipotent progenitor, MLP Multi-lymphoid progenitor, CMP–MEP Common myeloid progenitor and megakaryocyte-erythroid progenitor, GMP Granulocyte–Monocyte Progenitor, B-NK B-NK progenitor. **c** Representative flow cytometry profiles of human bone marrow and glioblastoma tissue, gated for seven HSPC subsets. Cellular frequencies are highlighted in red. **d** Stacked barplot of seven HSPC subsets observed in glioblastoma (GBM, n = 7), non-glioblastoma tumor tissues (non-GBM, n = 5, Supplementary Data 4) and a healthy donor bone marrow sample by flow cytometry. **e** Representative colony morphologies from CFC assays of glioblastoma cell suspensions derived from a total of eight patients, and from bone marrow-derived mononuclear cells. Scale bars = 100 μm. **f** Barplot indicating number and types of colonies in CFC assays derived from bone marrow, glioblastoma (GBM, n = 8 patients) and non-glioblastoma (non-GBM, n = 6 patients) cell suspensions. CFU Colony forming unit, -GEMM Granulocyte, erythrocyte, monocyte, megakaryocyte, -GM Granulocyte, monocyte, -E, Erythroid. **g** CXCL12 staining of the infiltration zone (upper panel) and the tumor (lower panel) of the same tissue section. Scale bars = 200 μm. One representative staining of eight shown. **h** Barplot showing percent CXCL12 staining intensity (1 = weakly positive, 2 = moderately positive, 3 = strongly positive) of tumor core and infiltration zones from glioblastoma (n = 16 samples from eight patients). Source data of (**a**), (**d**), (**f**), (**g**), and (**h**) are provided as a Source Data file.

therefore provide the necessary microenvironment for HSPC colonization and multilineage differentiation in glioblastoma.

Tumor-associated HSPCs show distinct phenotypes compared to bone marrow-derived and circulating HSPCs. To compare the phenotype of tumor-associated HSPCs with canonical HSPC subsets, we obtained single cell transcriptomes from magnetically enriched CD34+CD45+ *IDH* wt glioblastoma cells (n = 660 cells) derived from a fresh surgical specimen. For comparison, we used transcriptomes derived from bone marrow (n = 549), blood (n = 283) and a fresh tumor-free brain sample (n = 105) that were processed with an identical protocol (Fig. 4a and Supplementary Data 4). In the glioblastoma sample, Uniform Manifold Approximation and Projection (UMAP) and graph-based clustering unraveled 6 clusters (Fig. 4b). Cluster 3 significantly overexpressed the HSPC gene *SPINK2*[44] compared to all other clusters (Supplementary Fig. 5a). Independent annotation using a published reference-based algorithm[45] uncovered the same cluster as containing HSPCs (Fig. 4c). The remaining clusters were annotated as containing mainly myeloid cell types (monocytes, macrophages) or non-immune cells (Fig. 4c). Expression of known progenitor and myeloid markers confirmed our annotation. In particular, the HSPC cluster contained cells expressing *PTPRC* (CD45), cells exclusively expressing *CD34* and hemato-poietic progenitor markers *SPINK2* and *GATA2*[44], but lacked expression of myeloid lineage markers *CD14*, *ITGAM* (CD11b), microglia-specific markers (*TMEM119*) or myeloid markers typically expressed by immature (lin-) myeloid-derived sup-pressor cells (*CD33*) (Fig. 4d). The HSPC cluster also lacked expression of markers specific for lymphoid, endothelial, mesenchymal, astrocytic or neural populations (Supplementary Fig. 5b), confirming the enrichment of our targeted population. In the glioblastoma sample, we annotated a total of 126 tumor-associated HSPC transcriptomes subdivided as follows: HSC (n = 15 transcriptomes), MPP (n = 28), CMP (n = 2), GMP (n = 29), CLP (n = 14) and MEP (n = 38). Notably, in the sample derived from a tumor-free brain region, we failed to detect HSPC-typic transcriptomes, further substantiating a preferential accumulation of HSPCs in tumor tissues. In cells enriched from a healthy bone marrow and blood sample that were used as positive controls, we annotated 500 and 174 HSPCs, respectively (Fig. 4e). We next compared the transcriptomes of tumor-associated HSPCs with our control samples. Comparison was conducted in a normalized, combined dataset to interrogate proliferative states and to determine differentially expressed genes in HSPC subsets between glioblastoma and controls. UMAP plotting of HSPC tran-scriptomes from glioblastoma, bone marrow and blood clustered within a common region (Fig. 4f). In this topological repre-sentation, expression of marker genes for bone marrow-derived

HSPC subsets[46] and our annotated bone marrow sample matched specific regions of the graph. This was mirrored by the same subsets (except for CLP) annotated in the glioblastoma sample, indicating, at least for the HSC, MPP, GMP and MEP subsets, strong similarities between bone marrow and tumor-derived HSPC subsets (Supplementary Fig. 5c, d). Next, for these HSPC subsets, we scored non-cycling or cycling cells using an estab-lished algorithm[47]. The proportion of cell cycle phases in HSPCs from the bone marrow sample were in agreement with previously reported data[48,49]. However, we noted a significant increase of cycling MPP in the glioblastoma sample when compared to healthy bone marrow (Fig. 4g). In addition, the number of tumor associated HSPCs with an active cycling profile were pro-portionally higher compared to differentiated myeloid and lym-phoid cells within the same glioblastoma sample (Supplementary Fig. 5e, f). These data suggest that tumor-associated HSPC sub-sets, in particular MPPs, GMPs and MEPs may proliferate in situ. We next analyzed differential gene expression between HSPC subsets in our combined dataset. We selected genes that were consistently regulated between tumor-associated HSPCs and bone marrow or blood-derived HSPCs (Fig. 4h and Supplementary Data 5–8), for each subset with sufficient cells available. Inter-estingly, among the top upregulated genes in tumor-associated HSPCs, we noticed genes coding for proteins that were previously shown to impact on hematopoietic stem cell maintenance and cell cycle progression (e.g., *HMGB1*, *SOX4* and *STMN1*, in both HSCs and MPPs[50–52]) or to mediate tumor progression such as *TMSB10*[53]. In conclusion, single cell RNA-Seq analysis of tumor-associated HSPCs confirmed preferential enrichment of these population within glioblastoma compared to normal brain. Moreover, tumor-associated HSPC transcriptomes contained signatures associated with active cell cycle phases and showed enrichment of genes affecting hematopoietic progenitor main-tenance and tumor progression, when comparing with healthy bone marrow-derived and circulating HSPCs.

HSPCs promote a malignant and immunosuppressive pheno-type in glioblastoma. To investigate if hematopoietic progenitors can alter glioblastoma progression and/or immunosuppression, we co-cultured bone marrow-derived HSPCs with three fluores-cently labeled glioblastoma cell lines (T98G, LN229, U87) and monitored their proliferation and PD-L1 expression by flow cytometry. After 48 hours, we observed increased proliferation in all three cell lines tested in the presence of HSPCs compared to cultures without HSPCs (Fig. 5a–c). For example, 43.2% of T98G cells underwent at least one cellular division in the presence of HSPCs, compared to 23.4% in the control samples. Besides, we noted a proportion of tumor cells exhibiting accelerated cell cycle progression in the presence of HSPCs (Fig. 5b, d) as 16.7% of
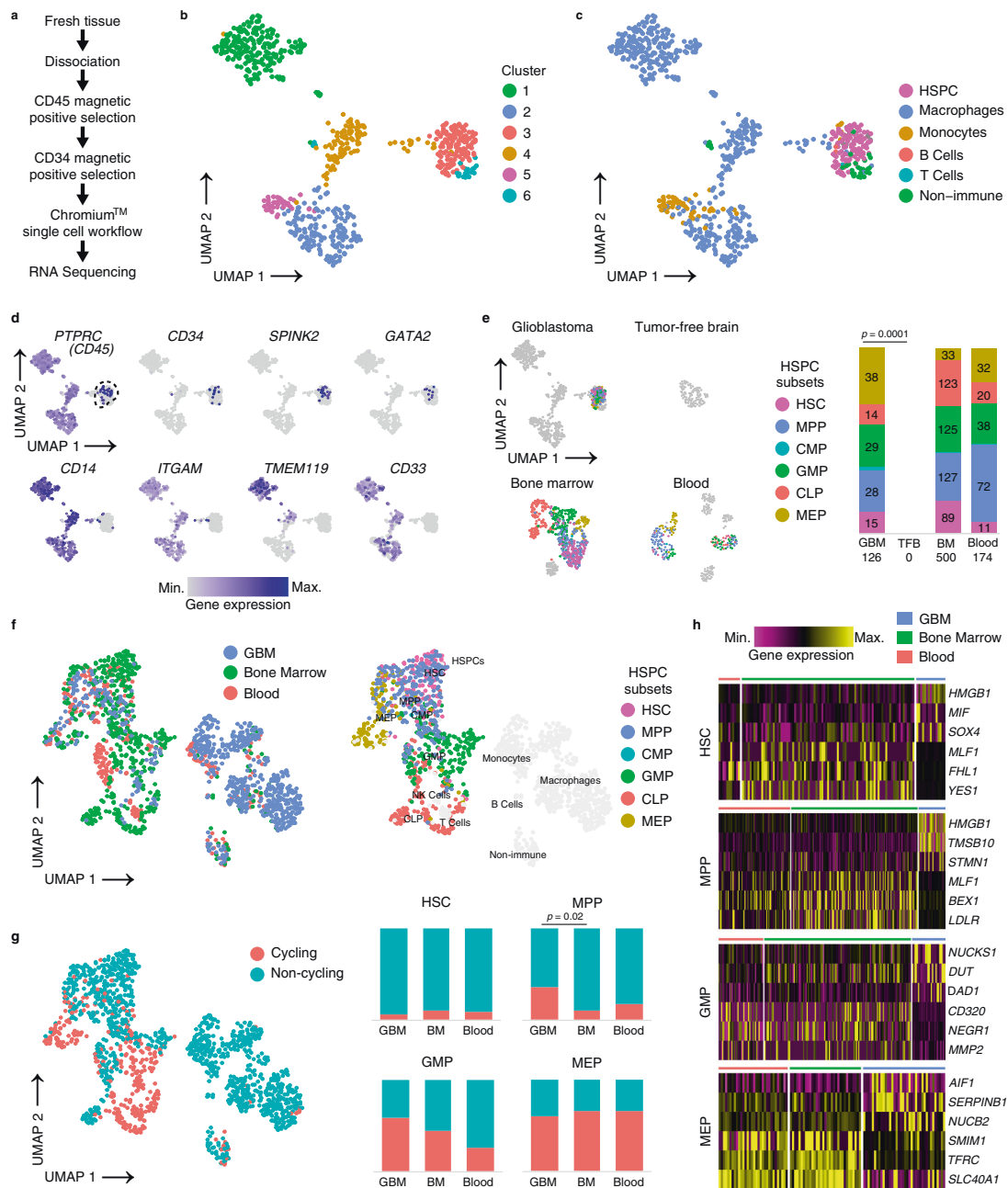
T98G underwent ≥2 division rounds within 48 h, compared to 0% in the absence of HSPCs. In both T98G and U87 co-cultured with HSPCs, we also observed an increase in cell-surface expression of PD-L1 (Fig. 5c), indicating that HSPCs may contribute to the immunosuppressive environment in glioblastoma progression by inducing the expression of immune checkpoint molecules on glioma cells. To test if proliferation and PD-L1 upregulation in tumor cells were caused by a soluble factor or by cell-cell contact, we incubated T98G cells with HSPCs or their conditioned media. The proliferation and PD-L1 expression were induced only in the

presence of HSPCs, indicating the requirement for direct cell-cell contact (Fig. 5e). Interestingly, in the presence of HSPCs, PD-L1 expression was upregulated exclusively in the T98G cells that underwent at least 2 divisions but not in the parental cells.

Neural stem cells (NSCs) carrying driver mutations have been proposed as cells of origin for glioblastoma. NSCs has also been showed to preferentially migrate and invade developing gliomas, promoting malignant progression[54,55]. To test if HSPCs may contribute to NSC recruitment in gliomas, we applied an invasion assay using human hippocampal adult human neural progenitors

Fig. 4 Comparing tumor-associated HSPCs with canonical hematopoietic progenitors by scRNA-Seq. a Enrichment protocol for derivation of single cell suspensions from biosamples. **b** UMAP projection of CD45+CD34+-enriched glioblastoma cells, color coded for graph-based clusters. **c** Cell type annotation by SingleR in the CD34+CD45+-enriched glioblastoma sample. HSPC Hematopoietic stem and progenitor cell. **d** Marker expression for immune (*PTPRC*), HSPCs (*CD34, SPINK2, GATA2*), and myeloid lineages (*CD14, ITGAM, TMEM119, CD33*) in the glioblastoma dataset. Dashed line indicates the HSPC cluster defined in (**c**). **e** SingleR annotation of HSPC subsets in glioblastoma (GBM), tumor-free brain (TFB), bone marrow (BM), and blood samples magnetically enriched by CD34+CD45+ are shown as UMAP projections. Stacked barplot indicates fractions of HSPC subsets as annotated in the four datasets with absolute numbers shown within bars. *p* value determined by a two-tailed Fisher's exact test. HSC Hematopoietic stem cell, MPP Multipotent progenitor, CMP Common myeloid progenitor, GMP Granulocyte–monocyte progenitor, CLP Common lymphoid progenitor, MEP Megakaryocyte–erythroid progenitor. **f** The left panel shows UMAP projection of the integrated dataset used for cell cycle and differential gene expression analysis. Cells derived from each sample are displayed by different color-coding. Right panel: singleR annotation of HSPC subsets in the integrated dataset are highlighted on the UMAP plot by the corresponding colors shown in the legend. NK cells Natural killer cells. **g** UMAP plot of cycling and non-cycling cells computed by Seurat. Stacked barplots show the proportion of cycling and non-cycling HSPC subsets in the glioblastoma (GBM), bone marrow (BM), and blood sample. *p* value determined by a two-tailed Fisher's exact test corrected by the Benjamini Hochberg procedure. **h** Heatmaps show a selection of top differentially expressed genes between bone marrow-resident and circulating HSPC subsets vs tumor-associated HSPCs as computed by MAST. The complete dataset is provided in the Supplementary Data 5–8. Source data are provided as a Source Data file.

(AHNPs)[56,57] cultured in the presence of HSPC-conditioned or control media. In this model, AHNPs showed a preferential migration towards HSPC conditioned media ($p < 0.05$), indicating a potential effect of tumor-associated HSPCs on NSC migration and recruitment in glioblastoma (Supplementary Fig. 6).

Patient-derived organoids are increasingly recognized as robust preclinical models for the study of cancer and response to therapy[58,59]. We cultured pure tumor cells from 3 primary glioblastoma patients and grew 3D organoids in the presence or absence of HSPCs, using a previously established protocol[60]. In two cases, 3D organoids could be maintained for >3 weeks in culture. As early as on day 4, we observed a significant increase in colony-forming activity of glioma cells co-cultured with HSPCs compared to controls (Fig. 5f, g). Furthermore, on day 10 after seeding, colonies in the presence of HSPCs formed long interconnections reminiscent of microtube networks reported by Oswald et al.[61] (Fig. 5f). Organoids supplied with HSPCs grew significantly larger when compared to cultures without HSPCs (Fig. 5h). Interestingly, patient-derived glioblastoma cells could stably maintain HSPC subsets for at least 20 days, in contrast to HSPC cultures seeded in the absence of tumor cells (Fig. 5i). These data suggest favorable conditions for the maintenance of HSPCs in glioblastoma. In addition, we noticed an expansion of a CD45+CD34− immune cell population within the organoid cultures, indicating that a subset of HSPCs are differentiating in the presence of patient-derived glioblastoma cells (Fig. 5i). However, PD-L1 expression was not differentially regulated in these experiments (Supplementary Fig. 7). To further characterize the relationship of HSPCs and glioblastoma cells during organoid expansion, we used a multiplex enzyme-linked immunosorbent assay (ELISA) to investigate the conditioned media for 30 different cytokines and growth factors. Interestingly, after 20 days of co-culture, we detected a significant increase of tumor-promoting cytokines such as interleukin 6 (IL-6)[62] and IL-8[63] ($p = 7.5 \times 10^{-7}$ and $p = 0.0028$, respectively), or positive regulators of immunosuppression such as chemokine ligand 2[64] (CCL2, $p = 0.035$) when compared to cultures containing tumor cells or HSPCs alone (Fig. 5j). In addition to these cytokines, we also detected a significant increase of soluble tumor necrosis factor α receptor 1 (sTNF-R1) ($p = 0.004$) and CCL4 ($p = 0.006$), after 9 and 20 days respectively. Other cytokines that were detected in the supernatants by this assay did not display significant changes between the different culture conditions (Supplementary Fig. 8).

In summary, using three in vitro and two ex vivo models, we observed consistent increase in tumor cell proliferation when cells were co-cultured with HSPCs. In T98G and LN229 cells, we detected a concurrent increase of PD-L1 expression on a

subpopulation of proliferating cells. HSPC-conditioned media promoted migration of AHNPs in vitro and co-cultures with patient-derived glioblastoma cells induced the secretion of tumor-promoting cytokines such as IL-6 and IL-8 or the immunosuppressive-related chemokine CCL2, indicating a potential role of HSPCs in promoting both, immunosuppression and malignancy phenotypes during glioblastoma progression.

Tissue-associated HSPCs predict patient's survival, correlate with hematopoietic niche factors and immunosuppressive markers. Next, we applied Syllogist to test the association of cellular composition with clinical outcome of 159 glioblastoma patients with follow-up clinical data available (TCGA)[31]. All tumor tissues were derived from previously untreated, primary glioblastoma patients undergoing standard surgery, radio- and adjuvant temozolomide therapy. Variables known to be associated with survival and therapy responses such as O^6-Methyl-guanine-DNA Methyltransferase (*MGMT*) promoter methylation[65], *IDH* mutation without 1p/19q codeletion[66] and biological subtypes[67,68] were also included in the analysis. By applying the random forest classifier[69], which can be employed to select for the best predictive variables within our dataset, we surprisingly identified three HSPC subsets, namely HSCs, CMPs, and promyelocytes among the most important predictors for overall survival of glioblastoma patients (Fig. 6a). The variable importance of these HSPC subsets was comparable with the above-mentioned positive controls.

Kaplan-Meier estimator of HSC^high and HSC^low patients and univariate Cox regression confirmed that HSC signals were negatively associated with overall and progression-free survival (Fig. 6b–d). To adjust for potential confounders such as age, *MGMT* methylation and *IDH* mutations, we fitted a multivariable Cox regression model of HSC signals for both, overall and progression-free survival. This model showed again a significant association of HSC with overall survival. In particular, our result indicated that in the TCGA cohort, at a given instant in time, a glioblastoma patient exhibiting an HSC signal ≥0.54 was 88% as likely to die as someone showing an HSC signal <0.54, adjusting for age, *MGMT* promoter methylation and *IDH* mutations (Fig. 6e and Supplementary Fig. 9). In our analysis, Syllogist did also detect a weak association of macrophages with overall survival, but, this result was not significant after correction for multiple testing (Supplementary Data 9).

In addition to survival, HSPC subsets significantly associated with signals from differentiated myeloid and lymphoid cell types (Supplementary Fig. 10). Interestingly, HSC^high glioblastoma samples significantly associated as well with increased expression levels of *TGFB1* and *IL10*, two genes coding for classical immunosuppressive

26
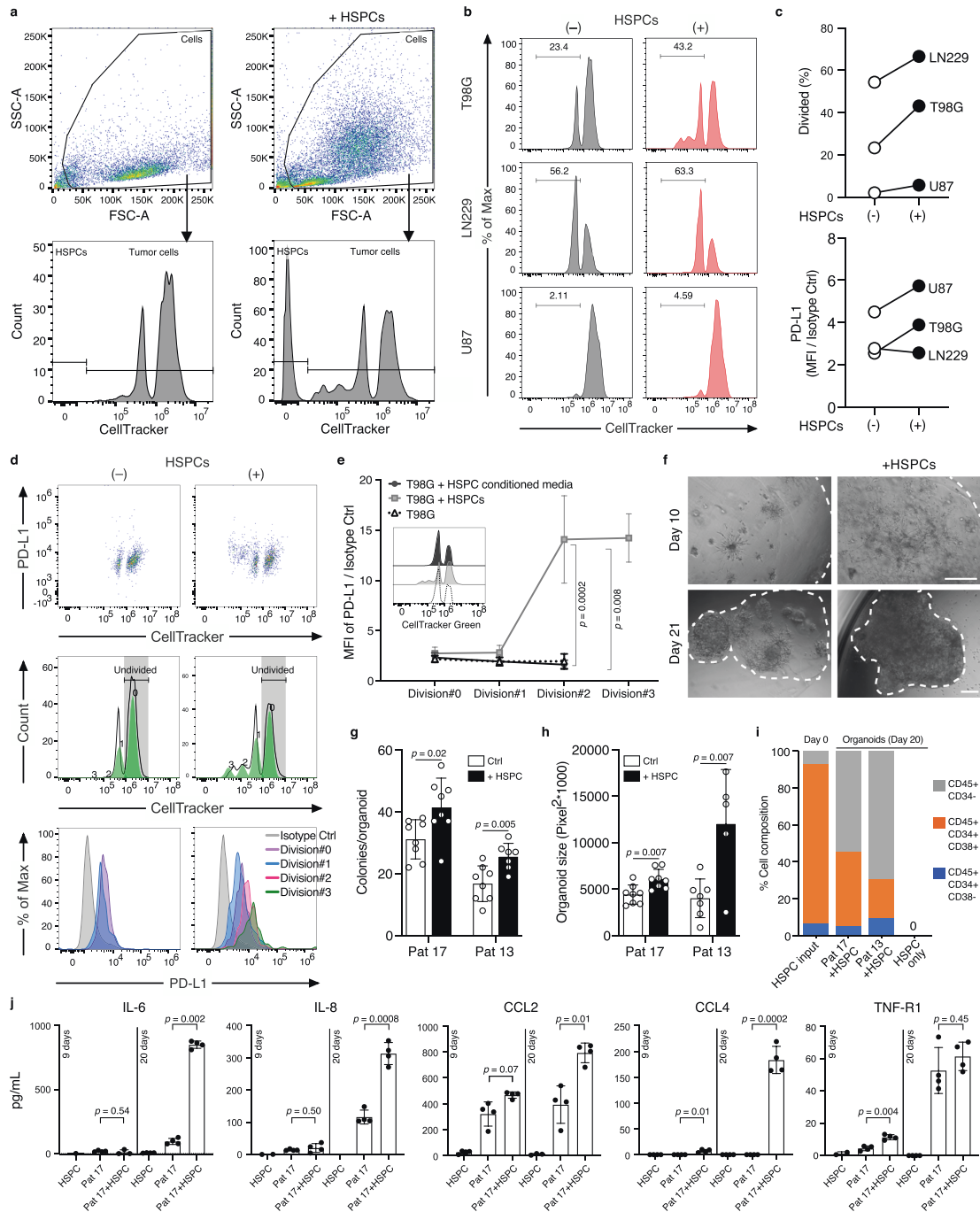
cytokines ($p = 1.4 \times 10^{-7}$, and $p = 9.7 \times 10^{-12}$ respectively, Student's t-test), but not with expression of proinflammatory cytokine genes such as *IL2*, *IFNG*, *IL12* or *IL17*. An exception to this were *TNF* and *IL6*[62,70], which positively associated with the HSC[high] samples (Fig. 6f and Supplementary Fig. 11a). Furthermore, HSC[high] glioblastoma samples associated with the expression of immune checkpoint molecules, including PD-1 (*PDCD1*, $p = 2.7 \times 10^{-4}$), PD-L1 (*CD274*,

$p = 0.016$), and PD-L2 (*PDCD1LG2*, $p = 0.003$) (Fig. 6g). Moreover, HSC[high] glioblastoma samples also exhibited significantly higher expression of chemokines such as *IL8*, *CCL2* and *CCL4*, in agreement with our organoid co-culture experiments shown in Fig. 5j (Supplementary Fig. 11b) or niche factors such as *CXCL12*, *LEPR* (leptin receptor), and *FN1* (fibronectin) (Fig. 6h)[32]. These results demonstrated that, in a dataset of 159 patients, tumor-associated

Fig. 5 HSPCs promote glioblastoma cell proliferation and PD-L1 expression. a Representative flow cytometry profiles of T98G cells in presence or absence of Hematopoietic stem and progenitor cells (HSPCs) with CellTracker Green staining and gating strategy used to distinguish glioblastoma cells from co-incubated HSPCs. **b** Representative histogram of tumor cell proliferation of T98G, LN229, and U87 glioblastoma cell lines, co-cultured with/ without bone marrow-derived HSPCs (ratio = 1:1) for 48 h. Tumor cell proliferation was assessed by CellTracker Green CMFDA dilution measured by flow cytometry. **c** Comparison of the percentage of cells that underwent at least one cell division (% Divided), and comparison of the tumor surface PD-L1 expression determined by the fold-changes of Median fluorescence intensity (MFI) from Isotype Control (Ctrl). ($n = 3$ cell lines, one representative experiment of two shown. (**d**) Representative flow cytometry profiles (out of three experiments) using combined stain of CellTracker Green CMFDA and PE-PD-L1 in T98G cells co-cultured with/without HSPCs. **e** PD-L1 expression in T98G cells co-cultured with HSPCs, HSPC conditioned media or control media for the indicated cell divisions. Results are presented as mean ± standard deviation ($n = 3–6$ technical replicates, one representative experiment of two shown). Two-tailed unpaired Student's t-test. Inset: representative flow cytometric profile of CellTracker Green CMFDA staining for the three conditions tested. **f** Representative images of organoids from patient 17 (Pat 17) cultured with and without HSPCs at day 10 and 21 post seeding, scale bar = 100 µm. **g** Barplot represents number of colonies/organoid measured on day 4 (Pat 17) and day 14 (Pat 13) post seeding. **h** Barplot represents organoid size measured on day 14 (Pat 17) and day 21 (Pat 13) after seeding. In (**g**) and (**h**), p values determined by two-tailed, unpaired Student's t-test. Results are presented as mean ± standard deviation ($n = 5–8$ organoids for each condition and time point). Three patients tested, one patient excluded from this analysis as we did not achieve sustained growth. **i** Maintenance of HSPC phenotype in organoid culture alone or in co-culture with patient tumor cells (Pat 17 and 13), a representative experiment of two is shown. **j** Barplots represent cytokine concentration (pg/mL) measured in conditioned media of organoids derived from patient 17 in the presence or absence of HSPCs, or in HSPCs cultured alone in 3D Matrigel. Conditioned media were collected after 9 and 20 days. Data are presented as mean ± standard deviation, $n = 1–4$ technical replicates from one representative experiment of two. p values determined using unpaired, two-tailed Student's t-test corrected with the Benjamini–Hochberg procedure. IL-6, IL-8 Interleukin-6 and -8, CCL2, CCL4 CC-chemokine ligand 2 and 4, TNF-R1 tumor necrosis factor receptor 1. Source data of (**c**), (**e**), (**g**), (**h**), (**i**), and (**j**) are provided as a Source Data file.

HSPC subsets are predictive for clinical outcomes in glioblastoma, associate with an immunosuppressive phenotype, with hematopoietic niche factors and with specific cancer-promoting cytokines and chemokines.

Discussion

Using Syllogist, we could determine the relative abundance of 43 different cell types in glioblastoma tissues using a gene enrichment approach. While other methods may have superior precision in the quantification of cell type proportions within a sample[71] they are restricted to a limited number of cell types. Syllogist can be useful in detecting multiple cell types, including hematopoietic progenitors, leveraging on a robust and validated reference transcriptome dataset[15].

Intending to characterize the cellular landscape of brain tumor tissues using a systematic and unbiased computational method, we identified HSPC transcriptomic signatures as markedly associated with brain tumors compared to normal brains and significantly enriched in glioblastoma when compared to lower grade *IDH* wildtype astrocytomas. Through a series of bioinformatic, flow cytometric, immunohistochemical and functional assays, we validated our initial working hypothesis and determined that HSPCs are infiltrating brain tumor tissues for the large proportion as immature progenitors. This is at first glance surprising because the bone marrow is the primary site of hematopoiesis in the adult. However, extramedullary hematopoiesis, especially in the liver and spleen, can sometimes be detected as a conserved physiological mechanism to maintain immunity under chronic anemias and myeloproliferative disorders[72]. Extramedullary HSPCs have also been detected under physiological conditions in several murine organs[73,74]. In addition, intravenously-injected HSPCs efficiently migrate to and infiltrate experimental rat[75] and mouse[76] gliomas, possibly by a CXCL12-dependent mechanism. Collectively, these data, together with our observations, may explain the enrichment of HSPCs in glioblastoma

Our findings suggest that HSPC subsets in brain tumors are positively associated with immunosuppressive and tumor-promoting phenotypes and negatively associated with patient survival. It is known that during cancer progression, bone marrow-derived HSPCs commit preferentially towards immunosuppressive lineages such as MDSCs induced by the tumor-derived cytokines granulocyte-macrophage colony-stimulating

factor (GM-CSF) and granulocyte colony-stimulating factor (G-CSF)[77]. Tumor-associated HSPCs may, therefore, be instructed by malignant cells to differentiate towards immunosuppressive myeloid cells. However, in murine models testing the effect of intravenously injected HSPCs, these cells were shown to replace local immunosuppressive myeloid cells with antigen-presenting cells, resulting in cytotoxic anti-tumor responses and tumor eradication[78]. In Flores *et al.*[79], ectopic injection of Lin⁻CCR2⁺ myeloid progenitors exhibited specific tropism to brain tumors and differentiated into antigen-presenting cells, cross-presenting to T cells in secondary lymphoid organs. These data indicate that tumor-associated HSPCs display a remarkable impact on the immunoregulation of the glioblastoma microenvironment: Contrary to observations in animal models that report favourable outcomes of intravenously injected HSPCs, our data reveal rather a cancer-promoting phenotype of the endogenous HSPCs that populate the human glioblastoma microenvironment. Therefore, remodeling of the lineage fate of tumor-associated HSPCs in humans may represent a potential therapeutic strategy to overcome immunosuppression and to provide the essential microenvironment for targeted immunotherapies. For example, blockade of the colony-stimulating factor (CSF) 1 - CSFR1 axis interfered with the maturation of bone marrow-derived hematopoietic progenitors into immunosuppressive myeloid cells[80] and reduced the pool of immunosuppressive myeloid cells in the brain[81]. Further, combining CSFR1 inhibition with PD-1/PD-L1 blocking antibodies resulted in superior tumor control compared to checkpoint inhibition alone in a mouse model of spontaneous neuroblastoma[82].

Our data suggest the requirement of cell-to-cell contact between HSPCs and glioblastoma cells for increased tumor cell proliferation and PD-L1 expression. Furthermore, patient-derived organoids revealed that glioblastoma cells can maintain HSPCs for extended periods of time in vitro, resulting in the secretion of cytokines and chemokines previously shown to promote tumor progression. These findings support the in vivo observations on the association with patient outcomes and immunosuppressive phenotypes.

However, our study presents with some limitations: Detailed investigation is needed to further understand the molecular mechanisms of our observations and to determine the role of the subpopulations responsible for the monitored effects. It is conceivable that some of the observed phenotypes are mediated by
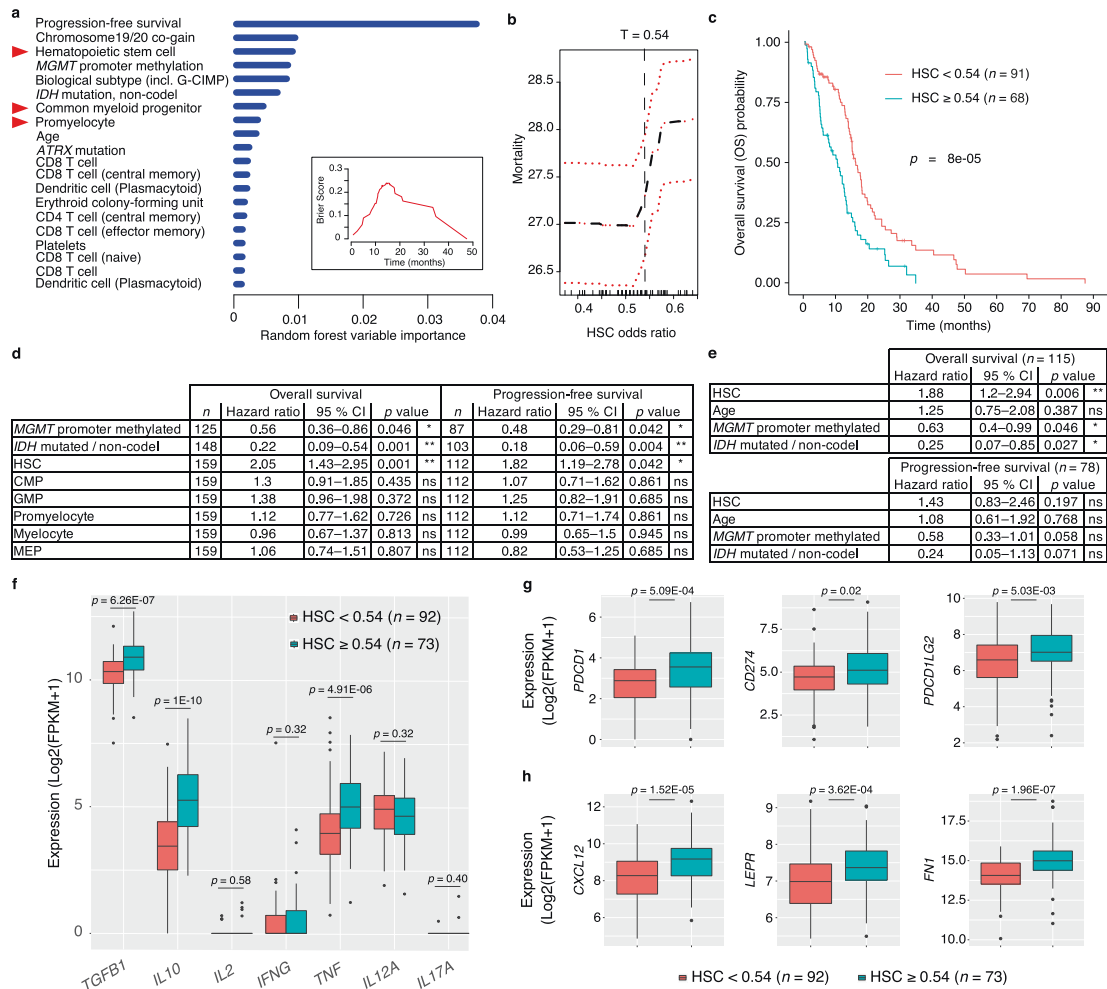
28

Fig. 6 HSPCs predict clinical outcomes in glioblastoma and associate with an immunosuppressive phenotype and stem cell niche factors. a Bar plot representing the top 20 predictors of glioblastoma overall survival in decreasing order of importance computed by the random forest classifier. Red triangles highlight HSPC subsets. Inset, Brier score indicates error rate of random forest classifier results as function of survival time (Brier score 0 = 0 % error, 1 = 100% error). MGMT O(6)-Methylguanine-DNA methyltransferase, G-CIMP Glioma CpG island methylator phenotype, IDH Isocitrate dehydrogenase. Source data are provided as a Source Data file. **b** Mortality rate as a function of hematopoietic stem cell (HSC) odds ratios derived by Syllogist and used to determine threshold separating HSC[high] (n = 63) and HSC[low] (n = 76) patients. Red lines represent 95% CI. **c** Kaplan–Meier plot of HSC[high] and HSC[low] patients using the threshold T = 0.54 selected from (**b**). Two-tailed logrank test. **d** Univariate Cox regression analysis of selected variables for overall survival and progression-free survival data. **e** Multivariable Cox proportional hazards model of the HSC subset and potential confounders (Age, MGMT methylation, and IDH mutations) for overall and progression-free survival. In (**d**) and (**e**), we used a two-tailed likelihood-ratio test corrected by the Benjamini–Hochberg procedure. All variables satisfied the proportionality hazards assumption (Methods). CMP Common myeloid progenitor, GMP Granulocyte–Monocyte progenitor, MEP Megakaryocyte–Erythroid progenitor. **f** Boxplots represent the expression of pro- and anti-inflammatory cytokines in HSC[high] (n = 73) and HSC[low] (n = 92) patient samples. TGFB1 Transforming growth factor beta 1, IL10, IL2 Interleukin 10 and 2, INFG Interferon gamma, TNF Tumor necrosis factor, IL12A Interleukin 12 subunit alpha, IL17A Interleukin 17A. **g** Boxplots represent the expression of the immune checkpoint markers PD-1 (PDCD1), PD-L1 (CD274), and PD-L2 (PDCD1LG2) in HSC[high] and HSC[low] samples. **h** Boxplots represent the expression of hematopoietic stem cell niche factors C-X-C motif chemokine 12 (CXCL12), leptin receptor (LEPR), and fibronectin (FN1) in HSC[high] and HSC[low] samples. In (**f–h**), boxplots are drawn with boxes representing the interquartile range (IQR), a line across the box indicating the median, and whiskers indicating 1.5 × IQR. Outliers are shown as closed dots. p values determined using a two-tailed Wilcoxon–Mann–Whitney U test corrected with the Benjamini–Hochberg procedure.

immune cells differentiating from local tumor-associated HSPCs and not by HSPCs themselves. In addition, our single cell data, while confirming presence of HSPCs and providing insights on their transcriptional profiles, represents a pilot study requiring follow up studies with a larger cohort.

In conclusion, the presence of multipotent HSPCs within the brain cancer microenvironment allows unconventional and straightforward access to an otherwise restricted immune compartment. Direct modulation of the lineage fate of tissue-associated HSPCs may represent a significant therapeutic

strategy to overcome immunosuppression or glioblastoma progression and warrants further studies. Flow cytometry-based analysis of hematopoietic progenitors in fresh tissue biopsies may furthermore serve as a prognostic factor in future clinical trials.

Methods

Cell type estimation using transcriptomes. Cell type-specific signals were determined similarly to Cima I et al.[16]. First, we generated a map of specific genes for each cell type of interest using the primary cell atlas[15], a gene expression matrix containing information on $n = 20969$ gene transcripts. Technical replicates were averaged. For each gene, g, in each cell type, or 'lineage', l, a 'specificity index', S, was calculated based on Shannon entropy and the Q statistics introduced by Schug et al.[18],

$$S_{(l|g)} = -\sum_{l=1}^{N} p_{(l|g)} \cdot \log_2(p_{(l|g)}) - \log_2(p_{(l|g)})$$

where $p_{(l,|g)}$ is the relative expression of gene g in lineage l. For each cell type, the top 80 genes with the highest specificity index ('specific genes') were selected and reported in Supplementary Data 1. This table represents the map of specific genes for each cell type of interest in decreasing order of specificity index. Next, for each RNA-Seq query sample, we predefined a threshold to define the set of expressed genes. Next, in the query RNA-Seq list of expressed genes, we counted the occurrences of the top 80 specific genes for each cell type present in our map of specific genes. To determine if the number of enriched genes was different from enrichment by chance, we generated 1,000 lists of 80 randomly selected genes from a comprehensive list of human genes derived from our reference transcriptomes and counted the average number of genes present by chance in each experimental RNA-Seq profile for each cell type. Finally, for each cell type in each experimental sample, a Fisher's exact test was applied to determine whether the number of enriched specific genes was equal to the number of randomly enriched genes. The resulting odds ratios were used in intersample comparisons to generate hypotheses on the differential content of cell types present in bulk tissues. In some experiments, we benchmarked Syllogist with previously published algorithms using TIMER 2.0 with default parameters[83].

Tissue collection. Biosamples were obtained from 29 patients after informed consent at the Departments of Neurosurgery of the University Hospitals Bonn and Essen. At each site, the local ethics committees approved the study (University Bonn #182/08; University of Duisburg-Essen, #19_8706_BO). Human biological samples and related data collected in Essen were provided by the Westdeutsche Biobank Essen (WBE, University Hospital Essen, University of Duisburg-Essen, Germany, approval 19_WBE_074). Baseline data for all patients are listed in Supplementary Data 4.

Immunohistochemistry/immunofluorescence studies. CXCL12 immunohistochemistry was performed on formalin-fixed, paraffin-embedded glioblastoma tissues obtained at the time of surgery. For antigen retrieval, slides with 2 μm-thick sections were pretreated boiling in sodium citrate buffer (pH = 6.0) for 30 min at 100 °C. Anti-CXCL12 antibody (Abcam ab9797, 1:600) was used to detect CXCL12 protein expression, and antibody-bound CXCL12 was then detected using the chromogen 3,3′-diaminobenzidine (DAB). Staining intensity was scored using a four-point scale from 0–3: 0 = no staining; 1 = cells weakly positive; 2 = cells moderately positive; 3 = cells strongly positive.

CD34 / CD45 immunofluorescence analysis was performed on formalin-fixed, paraffin-embedded glioblastoma tissues obtained at the time of surgery. 2 μm FFPE tissue sections were pretreated as described above. Anti-CD34 (Leica Biosystems, NCL-L-END, 1:250) and anti-CD45 (Abcam, ab10559, 1:250) antibodies were incubated 1 h at room temperature and slides washed three times before the respective secondary antibodies (cross-adsorbed anti-rabbit Alexa 488 and anti-mouse Alexa 555, 1:800, Life Technologies) were applied for 1 h at room temperature. Slides were mounted with Vectashield Antifade Mounting Medium with DAPI (Vector Laboratories) before imaging on a ZEISS ApoTome.2 Microscope (Zeiss) with the Zeiss ZEN 2.3 Imaging Software.

Tissue dissociation. Fresh surgical tissue was placed in ice-cold Dulbecco's Modified Eagle Medium (DMEM)/F12-based transport medium in the operating room and received on ice at the lab within 30 min thereafter. The tumor tissues were subsequently cut into small pieces and homogenized in Iscove's Modified Dulbecco's Medium (IMDM) with 0.11 DMC U/mL neutral protease (Nordmark Biochemicals) at 37 °C for 1–2 hour in a shaker-incubator. The homogenized tissues were centrifuged for 10 min at 300 g, resuspended in IMDM and filtered through a 40 μm cell strainer for the following FACS and CFC assays.

Flow cytometry. Tumor cell suspensions were incubated for 5 min with human Fc-gamma receptor (FcR)-binding inhibitor (1:50; BioLegend) and assayed for Hematopoietic Stem Cells (HSC: 7AAD−Lin−CD34+CD38−CD45RA−CD90+), Multi-Potent Progenitors (MPP: 7AAD−Lin−CD34+CD38−CD45RA−CD90−), Multi-

Lymphoid Progenitors (MLP: 7AAD−Lin−CD34+CD38+CD45RA+CD90−), Common Myeloid Progenitors and Megakaryocyte–Erythroid Progenitors (CMP-MEP: 7AAD−Lin−CD34+CD38+CD45RA−CD10−), Granulocyte–Monocyte Progenitors (GMP: 7AAD−Lin−CD34+CD38+CD45RA+CD10−), and B-NK Progenitors (B-NK: 7AAD−Lin−CD34+CD38+CD45RA+CD10+). For exclusion experiments of potential non-hematopoietic contaminants, tumor cell suspensions were additionally assayed for CD45 (PE/Cy7, 1:50, BioLegend). The immunofluorescent monoclonal antibodies BV421-CD10 (1:50), BV510-CD90 (1:50), BV711-CD135 (1:50), BV785-CD45RA (1:50), PE-CD34 (1:25), FITC-CD144 (1:25) and anti-Human Lineage Cocktail 1 (Lin 1, 1:25) were purchased from BD Biosciences. The APC-CD38 antibody (1:50) and 7-AAD (1:20) were purchased from eBioscience. For analysis of in vitro experiments, the tumor cell lines or cells from organoid experiments were assayed for PE-PD-L1 (1:100, BioLegend), BV510-CD45 (1:20, BioLegend) and BV786-CD56 (1:20, BD Biosciences) respectively, after co-culture with HSPCs. All the samples were analyzed on a FACS Celesta flow cytometer (BD Biosciences) using the FACS Diva v 8.0.1.1 software (BD Biosciences) and flow cytometry data were analyzed using FlowJo software, version 10.6.0 (Tree Star).

Colony-forming cell (CFC) assay. To observe hematopoietic colony-forming unit (CFU) formation, the cell suspension obtained from tumor tissue was seeded in methylcellulose media: (MethoCult H4230 and MethoCult SF H4236, Stemcell Technologies) according to manufacturer's protocol. Both media were supplemented with IL-3 (20 ng/mL), IL-6 (20 ng/mL), G-CSF (20 ng/mL), GM-CSF (20 ng/mL), SCF (50 ng/mL) and erythropoietin (3 units/mL). After incubation for 14–16 days at 37 °C with 5 % CO_2, the colonies were characterized and scored according to their morphology on a ZEISS AX10 Inverted Microscope (Zeiss).

Single Cell RNA Sequencing and analysis. $CD34^+$ and $CD45^+$ cells from two fresh glioblastoma tissues, one tumor-free region tissue, healthy bone marrow monoclear cells (CD34+ Lonza, 2M-101A) and one healthy PBMC sample (Lonza, 4W-270) were used for scRNA-Seq studies. Tissue samples were dissociated as previously described. $CD34^+/CD45^+$ positive magnetic selection was performed using the REAlease® CD45 (TIL) MicroBead Kit (Miltenyi Biotec, 130-121-563) and, immediately after removal of the CD45 complex, using the CD34 MicroBead Kit UltraPure (Miltenyi Biotec, 130-100-453) on the CD45 positively-selected samples, according to the manufacturer's instructions. After isolation, samples were stored at −80 °C in freezing medium (15% DMSO and 20% FBS in IMDM) until further processing. Before library preparation, samples were inspected for dead cells using trypan blue exclusion. At this stage, one glioblastoma sample was excluded from further analysis because of the presence of multicellular aggregates and 20% trypan blue positive cells. All other samples (Pat 24, Pat 25, bone marrow and PBMC sample) contained >92% viable cells without doublets, and were used for single cell sequencing. Next, library preparation was performed with all samples using the Chromium Next GEM Single Cell 3' Reagent Kits v3.1 (10x Genomics). Appropriate volume for the recovery of 770 cells was loaded onto a chip and DNA libraries were prepared according to the manufacturers protocol. Quality control of prepared libraries was performed using the Agilent 2100 Bioanalyzer prior to sequencing. Paired-end sequencing of all libraries was performed using the Illumina NovaSeq 6000 system on one flow cell lane. Illumina basecall (.bcl) data were converted and demultiplexed to FASTQ files using the bcl2fastq v2.20 software. Read alignment to the hg38 human reference genome, counts and cell-calling were computed using the 10x Genomics Cell Ranger 4.0.0 pipeline[84] for each sample with the "cellranger count" command and default parameters. Median UMI counts per cell in all samples ranged from 14,188 to 19,610. Count data were analyzed using Seurat[85] (v4.0). First, we removed cells with low counts (nFeature_RNA < 200) and high% of mitochondrial genes (>15%). Data were subsequently log-normalized before further analyses. Clustering was computed using the FindClusters function with parameter "resolution" set at 0.5. UMAP was computed using the first 30 dimensions as input. Annotation of cell types was performed using SingleR 1.4.1 with default parameters and the BlueprintEncodeData reference obtained from the celldex 1.0 package. The glioblastoma, bone marrow and blood samples were then integrated in one dataset for UMAP plotting, cell cycle and differential gene expression analysis. To this end, we used the default Seurat workflow on the log-normalized data and the IntegrateData function with the first 50 dimensions as input. Cell cycle analysis was performed using the CellCycleScoring function and the default list of cell cycle genes provided by Seurat 4.0 (cc.genes). Differential gene expression (DGE) was performed on the integrated dataset using the normalized and scaled data and the MAST[86] algorithm provided within the FindMarkers function with default parameters. For each HSPC subset, we selected genes with adjusted p value <0.05 that were commonly regulated between the glioblastoma-bone marrow and the glioblastoma-blood sample DGE analyses. The complete DGE results are reported in Supplementary Data 5–8.

In vitro HSPCs and tumor cell co-culture. Tumor cell lines T98G, LN229, and U87 (ATCC), were labeled with CellTracker Green CMFDA (5-chloromethyl-fluorescein diacetate, Thermo Fisher Scientific) at a final concentration of 1 μM for 15 min at 37 °C in darkness. After two washes with DMEM supplemented with 10 % FBS, the labeled tumor cells were combined with enriched bone marrow-derived HSPCs (Lonza Bioscience) in cell culture plates at 1:1 ratio or with the conditioned

medium derived from HSPC culture. After 48 h of co-incubation, supernatants were gently removed from the cell culture suspension and adherent tumor cells were detached with 0.11 DMC U/mL neutral protease (Nordmark Biochemicals) at 37 °C for 10 min and collected for immunofluorescent staining with PE-PD-L1. Flow cytometry analysis was performed to distinguish tumor cells from HSPCs and to monitor PD-L1 expression and proliferation in tumor cells by CMFDA dilution.

Patient-derived organoid co-culture. For organoid co-culture, patient-derived glioblastoma tumor cells (P13, P16, P17) were treated with 0.11 DMC U/mL neutral protease (Nordmark Biochemicals) at 37°C for 5 min at 400 g, and resuspended in Neurobasal-A medium (Life Technologies). After mixing with bone marrow-derived HSPCs at 1:1 ratio, cell suspensions were added into 4 times volume of Matrigel (Corning) in a separate tube kept on ice, and further transferred into a 96-well "droplet- forming plate" at a density of 2,000 cells per 20 µL, similarly as described in[60]. Each droplet was then transferred into an individual well of a 96-well plate and maintained in Neurobasal-A medium supplemented with 1% or 10% FBS, 50 U/mL penicillin, 50 mg/mL streptomycin, 0.5 mM glutamine, 10 µg/mL FGF, 10 µg/mL EGF at 37 °C with 5 % CO_2. Medium was exchanged every 2 days.

Multiplex ELISA array. Conditioned media from patient-derived organoids were assayed quantitatively for the following proteins: BDNF, CCL11, CCL17, CCL2, CCL24, CCL26, CCL4, CCL5, CNTF, CSF2, CXCL8, EGF, FAS, GDNF, IFNG, IL10, IL18, IL1A, IL1B, IL4, IL6, LIF, MMP2, MMP3, NGF, TGFB1, TIMP1, TNF, TNFRSF1A, VEGFA using a commercially available sandwich ELISA array kit (Quantibody® Human Neuro Discovery Array Kit, RayBiotech, QAH-NEU-1) according to the manufacturer's instructions and analyzed using the ImageJ Software v1.46r.

Invasion assay. To determine whether HSPCs recruit neural stem cells, a cell invasion assay was performed using Cytoselect™ 24 well collagen 1 colorimetric kit (Cell Biolabs). 250 µL cell suspension containing 0.5×10^6 cells/mL adult human neural progenitor cells (AHNPs[56,57]) were added to the upper chamber. Lower chambers were filled with 500 µL of CD34+ HSPC (Lonza) control or conditioned media. The cells were incubated for 24 h, 48 h, and 72 h at standard cell culture conditions (37°C, 5% CO_2). Non-invasive cells were removed from the upper chamber and invaded cells were stained and quantified by colorimetric measurement as described in the manufacturer's protocol.

Statistical analysis and random forest classifier. Statistical analyses were performed in the R environment (version 3.6.1)[87] or using the Prism software (v 8.4, GraphPad). Paired (Fig. 1f) and unpaired samples were tested using two-tailed Student's t-test. p values were adjusted by the Benjamini–Hochberg procedure in the case of multiple comparisons with control of the false discovery rate (FDR) at the 5 % level. Associations between categorical data were assessed using two-tailed Fisher's exact test. Correlations were described using Pearson's r. Kaplan–Meier estimators were compared using the log-rank test. In Fig. 6d, association of Syllogist signals with survival data were assessed by comparing univariate Cox proportional hazards models using the likelihood ratio test (p values corrected by the Benjamini–Hochberg procedure). To this end, all continuous variables were binned into two categories each using appropriate thresholds. This was necessary for the proportional hazard assumption to be met for all variables included in the analysis. This assumption was tested for each variable by the Schoenfeld individual test before fitting the models. To adjust for potential confounders, we used Cox multiple regression models. Box plots were drawn with boxes representing the interquartile range (IQR), a line across the box indicating the median, and whiskers indicating $1.5 \times$ IQR. The significance threshold was set at 0.05. For the random forest classifier we used the rfsrc function of the random forest package randomForestSRC with the following parameters: ntree = 1000, nsplit = 1, importance = "anti". Variable importance and estimation of the Brier score were reported in Fig. 6a.

Reporting summary. Further information on research design is available in the Nature Research Reporting Summary linked to this article.

Data availability
References to repositories for publicly available RNA-Seq datasets analyzed during the current study are listed in Supplementary Data 10. Single cell RNA-Seq data generated in this study (Fig. 4 and Supplementary Fig. 5) are available at the Gene Expression Omnibus under the accession number GSE165238. The source data underlying Figs. 1–6 and Supplementary Figures 2 and 4–8 are provided as a Source Data file. All the other data supporting the findings of this study are available within the article and its supplementary information files and from the corresponding author upon reasonable request. Source data are provided with this paper.

Code availability
R script and reference files used for transcriptome analyses are available at Zenodo with the identifier https://doi.org/10.5281/zenodo.4782282[88].

References
1. Stupp, R. et al. Radiotherapy plus concomitant and adjuvant temozolomide for glioblastoma. *N Engl. J. Med.* **352**, 987–996 (2005).
2. Stupp, R. et al. Effect of tumor-treating fields plus maintenance temozolomide vs maintenance temozolomide alone on survival in patients with glioblastoma: a randomized clinical trial. *JAMA* **318**, 2306–2316 (2017).
3. McGranahan, T., Therkelsen, K. E., Ahmad, S. & Nagpal, S. Current state of immunotherapy for treatment of glioblastoma. *Curr. Treat Options Oncol.* **20**, 24 (2019).
4. Lim, M., Xia, Y., Bettegowda, C. & Weller, M. Current state of immunotherapy for glioblastoma. *Nat. Rev. Clin. Oncol.* **15**, 422–442 (2018).
5. Brown, N. F., Carter, T. J., Ottaviani, D. & Mulholland, P. Harnessing the immune system in glioblastoma. *Br. J. Cancer.* **119**, 1171–1181 (2018).
6. Abedalthagafi, M., Barakeh, D. & Foshay, K. M. Immunogenetics of glioblastoma: the future of personalized patient management. *NPJ Precis. Oncol.* **2**, 27 (2018).
7. Bunse, L. et al. Suppression of antitumor T cell immunity by the oncometabolite (R)-2-hydroxyglutarate. *Nat. Med.* **24**, 1192–1203 (2018).
8. Filley, A. C., Henriquez, M. & Dey, M. Recurrent glioma clinical trial, CheckMate-143: the game is not over yet. *Oncotarget* **8**, 91779–91794 (2017).
9. O'Rourke DM, et al. A single dose of peripherally infused EGFRvIII-directed CAR T cells mediates antigen loss and induces adaptive resistance in patients with recurrent glioblastoma. *Sci. Transl. Med.* **9**, eaaa0984 (2017).
10. Brown, C. E. et al. Regression of glioblastoma after chimeric antigen receptor T-cell therapy. *N. Engl. J. Med.* **375**, 2561–2569 (2016).
11. Liau, L. M. et al. First results on survival from a large Phase 3 clinical trial of an autologous dendritic cell vaccine in newly diagnosed glioblastoma. *J Transl Med* **16**, 142 (2018).
12. Chen, Z. & Hambardzumyan, D. Immune microenvironment in glioblastoma subtypes. *Front. Immunol.* **9**, 1004 (2018).
13. Liang, J. et al. Neutrophils promote the malignant glioma phenotype through S100A4. *Clin. Cancer Res.* **20**, 187–198 (2014).
14. Gentles, A. J. et al. The prognostic landscape of genes and infiltrating immune cells across human cancers. *Nat. Med.* **21**, 938–945 (2015).
15. Mabbott, N. A., Baillie, J. K., Brown, H., Freeman, T. C. & Hume, D. A. An expression atlas of human primary cells: inference of gene function from coexpression networks. *BMC Genomics* **14**, 632 (2013).
16. Cima, I. et al. Tumor-derived circulating endothelial cell clusters in colorectal cancer. *Sci. Transl. Med.* **8**, 345ra389 (2016).
17. Li, H. et al. Reference component analysis of single-cell transcriptomes elucidates cellular heterogeneity in human colorectal tumors. *Nat. Genet.* **49**, 708–718 (2017).
18. Schug, J. et al. Promoter features related to tissue specificity as measured by Shannon entropy. *Genome Biol.* **6**, R33 (2005).
19. Bhattacharya, S. et al. ImmPort: disseminating data to the public for the future of immunology. *Immunol. Res.* **58**, 234–239 (2014).
20. Aran, D., Hu, Z. & Butte, A. J. xCell: digitally portraying the tissue cellular heterogeneity landscape. *Genome Biol.* **18**, 220 (2017).
21. Newman, A. M. et al. Robust enumeration of cell subsets from tissue expression profiles. *Nat. Methods* **12**, 453–457 (2015).
22. Finotello, F. et al. Molecular and pharmacological modulators of the tumor immune contexture revealed by deconvolution of RNA-seq data. *Genome Med* **11**, 34 (2019).
23. Racle J, de Jonge K, Baumgaertner P, Speiser DE, Gfeller D. Simultaneous enumeration of cancer and immune cell types from bulk tumor gene expression data. *Elife* **6**, e26476 (2017).
24. Miller JA, et al. Neuropathological and transcriptomic characteristics of the aged brain. *Elife* **6**, e31126 (2017).
25. Glas, M. et al. Residual tumor cells are unique cellular targets in glioblastoma. *Ann. Neurol.* **68**, 264–269 (2010).
26. Gill, B. J. et al. MRI-localized biopsies reveal subtype-specific differences in molecular and cellular composition at the margins of glioblastoma. *Proc. Natl. Acad. Sci. USA* **111**, 12550–12555 (2014).
27. Brat, D. J. et al. cIMPACT-NOW update 3: recommended diagnostic criteria for "Diffuse astrocytic glioma, IDH-wildtype, with molecular features of glioblastoma, WHO grade IV". *Acta. Neuropathol.* **136**, 805–810 (2018).
28. Hasselblatt, M. et al. Diffuse astrocytoma, IDH-Wildtype: a dissolving diagnosis. *J. Neuropathol. Exp. Neurol.* **77**, 422–425 (2018).
29. Cancer Genome Atlas Research N. et al.Comprehensive, integrative genomic analysis of diffuse lower-grade gliomas. *N. Engl. J. Med.* **372**, 2481–2498 (2015).

30. Brennan, C. W. et al. The somatic genomic landscape of glioblastoma. *Cell* **155**, 462–477 (2013).

31. Bronte, V. et al. Recommendations for myeloid-derived suppressor cell nomenclature and characterization standards. *Nat. Commun.* **7**, 12150 (2016).

32. Pinho, S & Frenette, P. S. Haematopoietic stem cell activity and interactions with the niche. *Nat. Rev. Mol. Cell Biol.* **20**, 303–320 (2019).

33. Velten, L. et al. Human haematopoietic stem cell lineage commitment is a continuous process. *Nat. Cell Biol.* **19**, 271–281 (2017).

34. Cimato, T. R., Furlage, R. L., Conway, A. & Wallace, P. K. Simultaneous measurement of human hematopoietic stem and progenitor cells in blood using multicolor flow cytometry. *Cytometry B. Clin. Cytom.* **90**, 415–423 (2016).

35. Siemerink, M. J. et al. CD34 marks angiogenic tip cells in human vascular endothelial cell cultures. *Angiogenesis* **15**, 151–163 (2012).

36. Mei, X., Chen, Y. S., Chen, F. R., Xi, S. Y. & Chen, Z. P. Glioblastoma stem cell differentiation into endothelial cells evidenced through live-cell imaging. *Neuro. Oncol.* **19**, 1109–1118 (2017).

37. Jersmann, H. P., Hii, C. S., Hodge, G. L. & Ferrante, A. Synthesis and surface expression of CD14 by human endothelial cells. *Infect. Immun.* **69**, 479–485 (2001).

38. Jersmann, H. P. Time to abandon dogma: CD14 is expressed by non-myeloid lineage cells. *Immunol. Cell Biol.* **83**, 462–467 (2005).

39. Hikawa, T., Mori, T., Abe, T. & Hori, S. The ability in adhesion and invasion of drug-resistant human glioma cells. *J. Exp. Clin. Cancer Res.* **19**, 357–362 (2000).

40. Gingras, M. C., Roussel, E., Bruner, J. M., Branch, C. D. & Moser, R. P. Comparison of cell adhesion molecule expression between glioblastoma multiforme and autologous normal brain tissue. *J. Neuroimmunol.* **57**, 143–153 (1995).

41. Neftel, C. et al. An integrative model of cellular states, plasticity, and genetics for glioblastoma. *Cell* **178**, 835–849 (2019). e821.

42. Han, X. et al. Construction of a human cell landscape at single-cell level. *Nature* **581**, 303–309 (2020).

43. Sugiyama, T., Kohara, H., Noda, M. & Nagasawa, T. Maintenance of the hematopoietic stem cell pool by CXCL12-CXCR4 chemokine signaling in bone marrow stromal cell niches. *Immunity* **25**, 977–988 (2006).

44. Popescu, D. M. et al. Decoding human fetal liver haematopoiesis. *Nature* **574**, 365–371 (2019).

45. Aran, D. et al. Reference-based analysis of lung single-cell sequencing reveals a transitional profibrotic macrophage. *Nat. Immunol.* **20**, 163–172 (2019).

46. Pellin, D. et al. A comprehensive single cell transcriptional landscape of human hematopoietic progenitors. *Nat. Commun.* **10**, 2395 (2019).

47. Butler, A., Hoffman, P., Smibert, P., Papalexi, E. & Satija, R. Integrating single-cell transcriptomic data across different conditions, technologies, and species. *Nat Biotechnol* **36**, 411–420 (2018).

48. Bjorn N, Jakobsen I, Lotfi K, Green H. Single-Cell RNA Sequencing of Hematopoietic Stem and Progenitor Cells Treated with Gemcitabine and Carboplatin. *Genes (Basel)* **11**, 549 (2020).

49. Canu, G. et al. Analysis of endothelial-to-haematopoietic transition at the single cell level identifies cell cycle regulation as a driver of differentiation. *Genome Biol.* **21**, 157 (2020).

50. Novershtern, N. et al. Densely interconnected transcriptional circuits control cell states in human hematopoiesis. *Cell* **144**, 296–309 (2011).

51. Machado-Neto, J. A., Saad, S. T. & Traina, F. Stathmin 1 in normal and malignant hematopoiesis. *BMB Rep.* **47**, 660–665 (2014).

52. Lee, G. et al. Fully reduced HMGB1 accelerates the regeneration of multiple tissues by transitioning stem cells to GAlert. *Proc. Natl. Acad. Sci. USA* **115**, E4463–E4472 (2018).

53. Zhang, X. et al. Thymosin beta 10 is a key regulator of tumorigenesis and metastasis and a novel serum marker in breast cancer. *Breast Cancer Res.* **19**, 15 (2017).

54. Aboody, K. S. et al. Neural stem cells display extensive tropism for pathology in adult brain: evidence from intracranial gliomas. *Proc. Natl. Acad. Sci. USA* **97**, 12846–12851 (2000).

55. Lee, J. H. et al. Human glioblastoma arises from subventricular zone cells with low-level driver mutations. *Nature* **560**, 243–247 (2018).

56. Glas, M. et al. Targeting the cytosolic innate immune receptors RIG-I and MDA5 effectively counteracts cancer cell heterogeneity in glioblastoma. *Stem Cells* **31**, 1064–1074 (2013).

57. Walton, N. M. et al. Derivation and large-scale expansion of multipotent astroglial neural progenitors from adult human brain. *Development* **133**, 3671–3681 (2006).

58. Vlachogiannis, G. et al. Patient-derived organoids model treatment response of metastatic gastrointestinal cancers. *Science* **359**, 920–926 (2018).

59. Fatehullah, A., Tan, S. H. & Barker, N. Organoids as an in vitro model of human development and disease. *Nat. Cell Biol.* **18**, 246–254 (2016).

60. Hubert, C. G. et al. A three-dimensional organoid culture system derived from human glioblastomas recapitulates the hypoxic gradients and cancer stem cell heterogeneity of tumors found in vivo. *Cancer Res.* **76**, 2465–2477 (2016).

61. Osswald, M. et al. Brain tumour cells interconnect to a functional and resistant network. *Nature* **528**, 93–98 (2015).

62. Weissenberger, J. et al. IL-6 is required for glioma development in a mouse model. *Oncogene* **23**, 3308–3316 (2004).

63. Brat, D. J., Bellail, A. C., Van & Meir, E. G. The role of interleukin-8 and its receptors in gliomagenesis and tumoral angiogenesis. *Neuro Oncol.* **7**, 122–133 (2005).

64. Chang, A. L. et al. CCL2 produced by the glioma microenvironment is essential for the recruitment of regulatory T cells and myeloid-derived suppressor cells. *Cancer Res.* **76**, 5671–5682 (2016).

65. Hegi, M. E. et al. MGMT gene silencing and benefit from temozolomide in glioblastoma. *N. Engl. J. Med.* **352**, 997–1003 (2005).

66. Ichimura, K. et al. IDH1 mutations are present in the majority of common adult gliomas but rare in primary glioblastomas. *Neuro. Oncol.* **11**, 341–347 (2009).

67. Verhaak, R. G. et al. Integrated genomic analysis identifies clinically relevant subtypes of glioblastoma characterized by abnormalities in PDGFRA, IDH1, EGFR, and NF1. *Cancer Cell* **17**, 98–110 (2010).

68. Noushmehr, H. et al. Identification of a CpG island methylator phenotype that defines a distinct subgroup of glioma. *Cancer Cell* **17**, 510–522 (2010).

69. Breiman, L. Random forests. *Mach. Learn.* **45**, 5–32 (2001).

70. West, A. J. et al. The role of interleukin-6-STAT3 signalling in glioblastoma. *Oncol. Lett.* **16**, 4095–4104 (2018).

71. Finotello, F., Rieder, D., Hackl, H. & Trajanoski, Z. Next-generation computational tools for interrogating cancer immunity. *Nat. Rev. Genet.* **20**, 724–746 (2019).

72. Sohawon, D., Lau, K. K., Lau, T. & Bowden, D. K. Extra-medullary haematopoiesis: a pictorial review of its typical and atypical locations. *J. Med. Imaging Radiat. Oncol.* **56**, 538–544 (2012).

73. Lefrancais, E. et al. The lung is a site of platelet biogenesis and a reservoir for haematopoietic progenitors. *Nature* **544**, 105–109 (2017).

74. Massberg, S. et al. Immunosurveillance by hematopoietic progenitor cells trafficking through blood, lymph, and peripheral tissues. *Cell* **131**, 994–1008 (2007).

75. Bryukhovetskiy, I. S. et al. Hematopoietic stem cells as a tool for the treatment of glioblastoma multiforme. *Mol. Med. Rep.* **14**, 4511–4520 (2016).

76. Tabatabai, G. et al. Lessons from the bone marrow: how malignant glioma cells attract adult haematopoietic progenitor cells. *Brain* **128**, 2200–2211 (2005).

77. Wu, W. C. et al. Circulating hematopoietic stem and progenitor cells are myeloid-biased in cancer patients. *Proc. Natl. Acad. Sci. USA* **111**, 4221–4226 (2014).

78. Wildes, T. J. et al. Cross-talk between T cells and hematopoietic stem cells during adoptive cellular therapy for malignant glioma. *Clin. Cancer Res.* **24**, 3955–3966 (2018).

79. Flores, C. T. et al. Lin(-)CCR2(+) hematopoietic stem and progenitor cells overcome resistance to PD-1 blockade. *Nat. Commun.* **9**, 4313 (2018).

80. Mao, Y. et al. Targeting suppressive myeloid cells potentiates checkpoint inhibitors to control spontaneous neuroblastoma. *Clin. Cancer Res.* **22**, 3849–3859 (2016).

81. Mossadegh-Keller, N. et al. M-CSF instructs myeloid lineage fate in single haematopoietic stem cells. *Nature* **497**, 239–243 (2013).

82. Cannarile, M. A. et al. Colony-stimulating factor 1 receptor (CSF1R) inhibitors in cancer therapy. *J. Immunother. Cancer* **5**, 53 (2017).

83. Li, T., et al. TIMER2.0 for analysis of tumor-infiltrating immune cells. *Nucleic Acids Res.* **48**, W509–W514 (2020).

84. Zheng, G. X. et al. Massively parallel digital transcriptional profiling of single cells. *Nat. Commun.* **8**, 14049 (2017).

85. Stuart, T. et al. Comprehensive Integration of Single-. *Cell Data. Cell* **177**, 1888–1902 (2019). e1821.

86. Finak, G. et al. MAST: a flexible statistical framework for assessing transcriptional changes and characterizing heterogeneity in single-cell RNA sequencing data. *Genome Biol* **16**, 278 (2015).

87. R Core Team. R: A language and environment for statistical computing. R Foundation for Statistical Computing, Vienna, Austria. Available online at https://www.R-project.org/ (2018).

88. Cima I, Dobersalske C, Scheffler B. Syllogist, a reference-based algorithm for cell type estimation (Version 0.1.0). Zenodo. https://doi.org/10.5281/zenodo.4782282 (2021, May 23).

Acknowledgements

Author contributions

Bioinformatics and data processing: C.D., S.K., I.C. Immunofluorescence and immuno-
histochemistry: I.L., C.D., S.T.H., T.B., I.C. Flow cytometry: I.L., C.D., V.U., I.C. Single
cell RNA-Seq: C.D., A.S., V.U., J.C.B., I.C. Patient-derived ex vivo and in vitro assays: I.L.,
C.D., S.P., I.C. Clinical samples, clinical data and guidance on clinical aspects of the
study: L.R., S.K., J.T.S., U.S., M.G., B.S. Manuscript draft: C.D., I.C. with input from I.L.,
L.R., S.T.H., V.U., S.P., S.K., J.T.S., B.S. Supervision, study design and funds acquisition:
B.S., I.C.

Funding

Competing interests

J.T.S.: Bristol-Myers Squibb, Celgene, Roche (Research Funding - outside of this study);
AstraZeneca, Bristol-Myers Squibb, Celgene, Immunocore, Novartis, Roche, Shire
(Consulting or advisory role); AstraZeneca, Aurikamed, Baxalta, Bristol-Myers Squibb,
Celgene, Falk Foundation, iomedico, Immunocore, Novartis, Roche, Shire (honoraria);
minor equity in FAPI Holding and Pharma15 (<3%) and member of the Board of
Directors for Pharma15 outside the submitted work. All other authors declare no
competing interests.

Additional information

Supplementary information The online version contains supplementary material
available at https://doi.org/10.1038/s41467-021-23995-z.

Correspondence and requests for materials should be addressed to I.C.

Peer review information *Nature Communications* thanks the anonymous reviewer(s) for
their contribution to the peer review of this work. Peer reviewer reports are available.

Reprints and permission information is available at http://www.nature.com/reprints

Publisher's note Springer Nature remains neutral with regard to jurisdictional claims in
published maps and institutional affiliations.

SUPPLEMENTARY INFORMATION

34

Tumor-associated hematopoietic stem and progenitor cells positively linked to glioblastoma progression.

I-Na Lu, Celia Dobersalske *et al.*
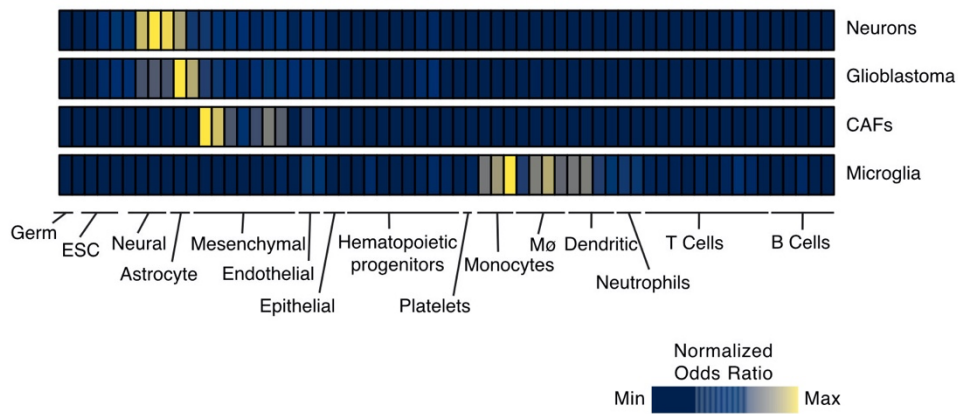
Supplementary Fig. 1: Additional cell types tested by Syllogist. Each colored box represents a normalized odds ratio ranging from 0 (blue) to 1 (yellow). Identifiers for publicly available datasets used in this analysis are reported in Supplementary Data 10. CAFs, Cancer Associated Fibroblasts; ESC, Embryonic Stem Cell, Mø, Macrophages.
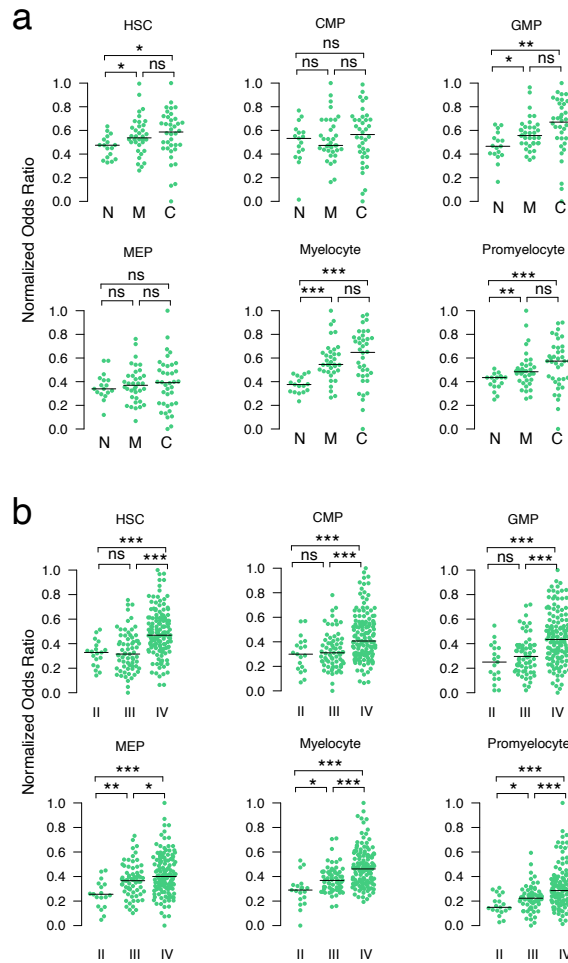
Supplementary Fig. 2: a Association of six HSPC subsets with brain tumor locations from normal brains (N, *n* = 17 samples), glioblastoma margins (M, *n* = 36) and cores (C, *n* = 38). **b** Association of six HSPC subsets with diffuse astrocytomas (WHO grade II, *n* =19 samples), anaplastic astrocytoma (WHO grade III, *n* = 67) and glioblastoma (WHO grade IV, *n* = *143*). Dot plots represent normalized odds ratios computed by Syllogist. Line across dot plots represent median values for each variable.For **a** and **b**, *p* values were determined by 2-tailed, unpaired Student's *t*-test with correction by the Benjamini-Hochberg procedure. *, *p* < 0.05; **, *p* < 0.01; ***, *p* < 0.001, ns, not significant. Exact *p* values are reported in Supplementary Data 2 and 3, respectively Source data are provided as a Source Data file. HSC, Hematopoietic Stem Cell; CMP, Common Myeloid Progenitor; GMP Granulocyte-Monocyte Progenitor; MEP, Megakaryocyte-Erythroid Progenitor.
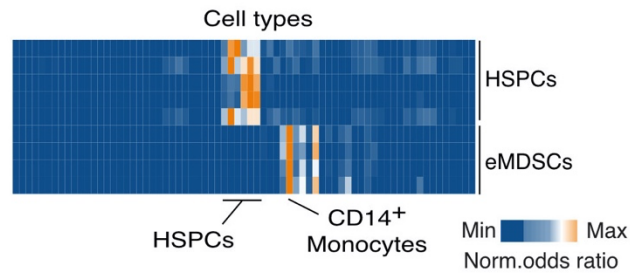
Supplementary Fig. 3: Syllogist transcriptome analysis of eMDSCs and HSPCs indicating distinct signals without overlap. Data were quantile normalized before analysis. Information about the publicly available datasets used in this analysis are reported in Supplementary Data 10.
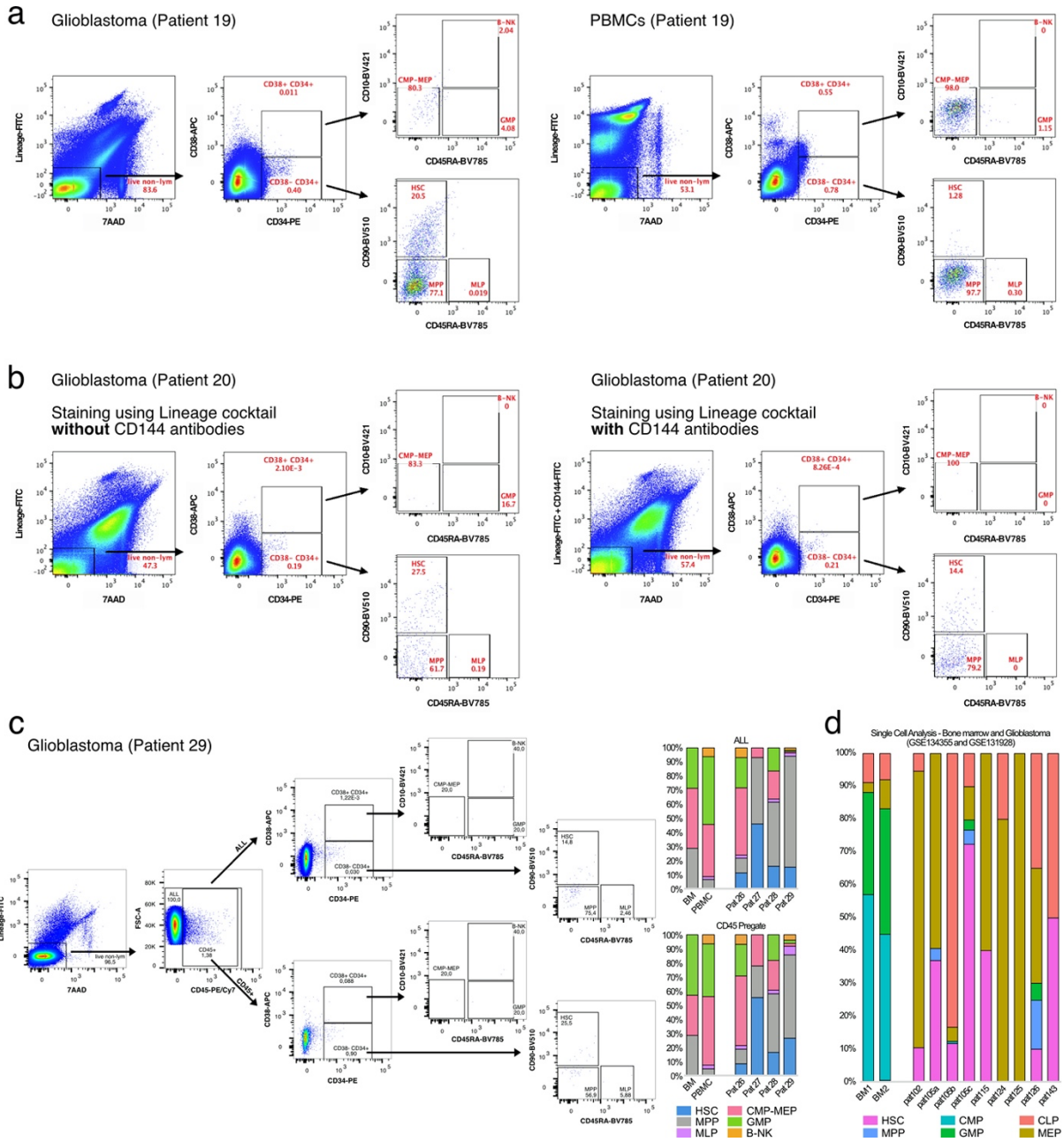
Supplementary Fig. 4: Flow cytometric analyses of circulating and tissue-associated HSPCs. **a** HSPCs subsets as shown in Fig. 3b were measured from samples of a glioblastoma single cell suspension (left panel) and PBMCs (right panel) from the same patient. Note the HSC gate in both samples indicating enrichment in glioblastoma compared to blood. **b** Glioblastoma cell suspensions were stained with a lineage marker cocktail with and without anti-CD144 antibodies (*n* = 1 patient). **c** Representative flow cytometry profile of glioblastoma tissue gated for HSPC subsets with and without CD45 pre-gating. Stacked barplot indicates proportions of HSPC subsets in PBMC (*n* = 1), BM (*n* = 1) and glioblastoma samples (*n* = 4) with and without

CD45 pre-gating. **d** Annotation of HSPC subsets in publicly available scRNA-Seq data of 9 glioblastoma samples (n = 7 patients) and 2 bone marrow samples. Source data of c and d are provided as a Source Data file. HSC, Hematopoietic Stem Cell; MPP, Multipotent Progenitor; MLP, Multi-Lymphoid Progenitor; CMP-MEP, Common Myeloid Progenitor and Megakaryocyte-Erythroid Progenitor; GMP, Granulocyte-Monocyte Progenitor; B-NK, B-NK Progenitor
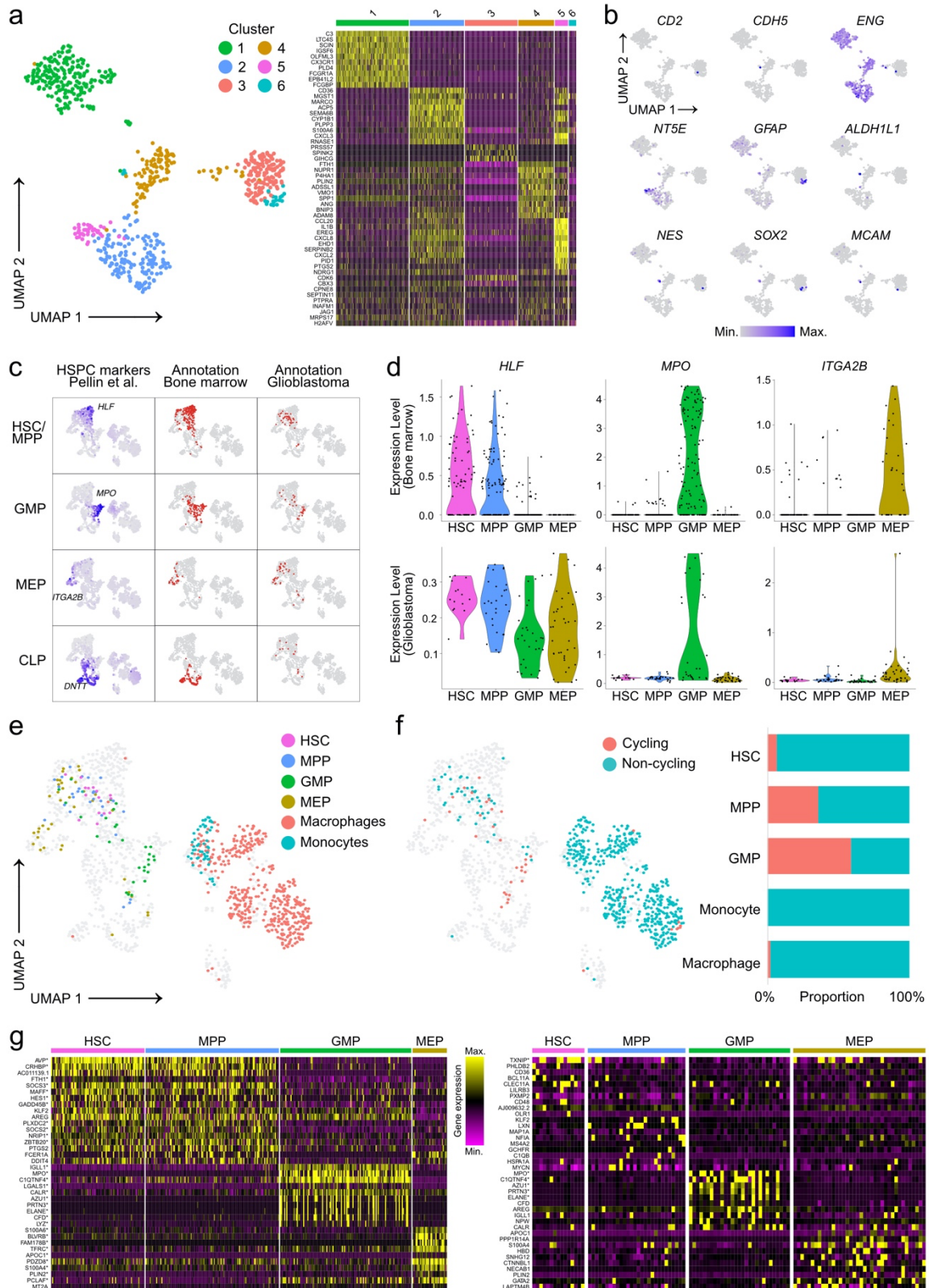
Supplementary Fig. 5: Comparison of tumor-associated HSPCs with canonical hematopoietic progenitors by scRNA-Seq

a Heatmap of differentially expressed genes between graph-based clusters in the CD45+CD34+-enriched glioblastoma dataset. **b** Marker expression for lymphoid

(*CD2*), endothelial (*CDH5, MCAM*), mesenchymal (*ENG, NT5E*), astrocytic (*GFAP, ALDH1L1*) and neuronal cells (*NES, SOX2*) of the glioblastoma dataset. **c** UMAP plots highlighting the expression of markers specific for the hematopoietic stem and progenitor cell (HSPC) subsets HSC/MPP (*HLF*), GMP (*MPO*), MEP (*ITGA2B*) and CLP (*DNTT*) in the integrated dataset (first column), and cells annotated by SingleR in the bone marrow (second column) and glioblastoma (third column) dataset. HSC, Hematopoietic Stem Cell; MPP, Multipotent Progenitor; GMP, Granulocyte-Monocyte Progenitor; MEP, Megakaryocyte-Erythroid Progenitor; CLP, Common Lymphoid Progenitor. **d** Violin plots showing selected marker expression from c in the bone marrow and glioblastoma HSPC subsets annotated by SingleR. **e** UMAP plot of the integrated dataset highlighting glioblastoma-annotated HSPCs by subset. **f** Cycling and non-cycling cells computed by Seurat for the glioblastoma HSPCs (left) and stacked barplots showing the respective cycling and non-cycling proportions for the indicated cell types (right). **g** Heatmaps showing the top overexpressed genes between HSPC subsets from the bone marrow (left) and the glioblastoma (right) dataset. Asterisks show genes significantly regulated after adjustment ($p < 0.05$, two-tailed Student's t-test with Bonferroni correction). Source data are provided as a Source Data file.
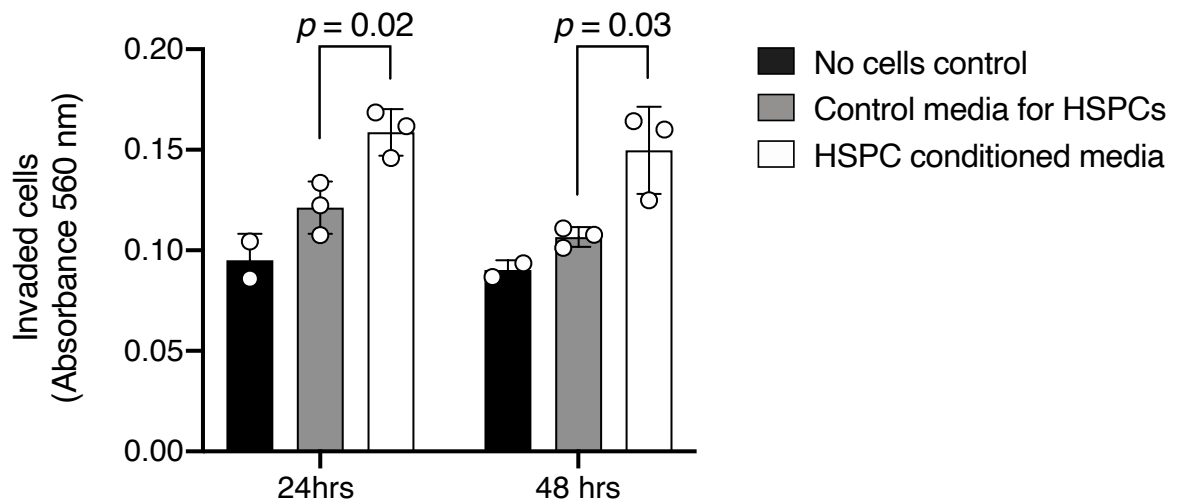
Supplementary Fig. 6: Invasion assay using hippocampus-derived adult human neural progenitor cells (AHNP) and control or hematopoietic stem and progenitor cell (HSPC) conditioned media. Invaded cells were stained and quantified by colorimetric measurement as described in the manufacturer's protocol. Results are presented as mean ± standard deviation. Statistics derived from *n* = 3 technical replicates from a representative experiment of 3. *p* values determined by unpaired two-tailed Student's *t*-test. Source data are provided as a Source Data file.
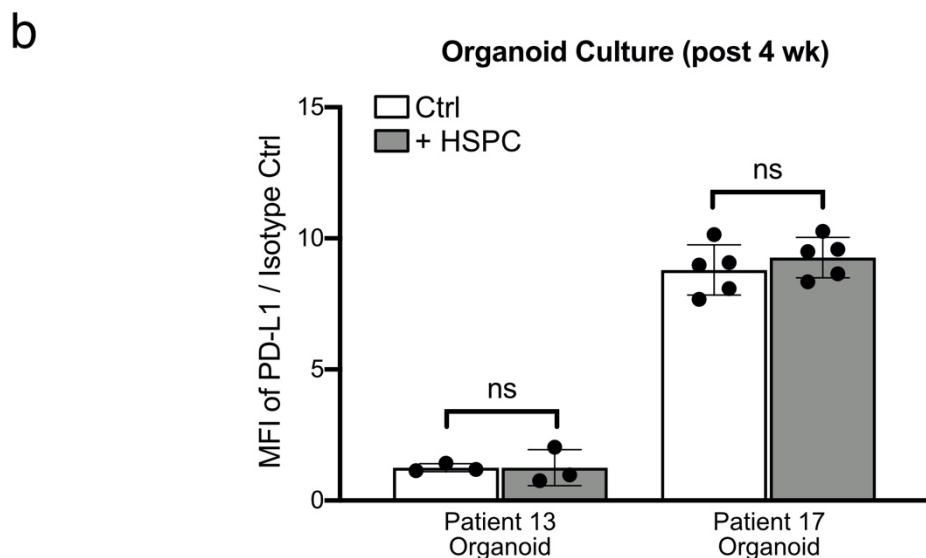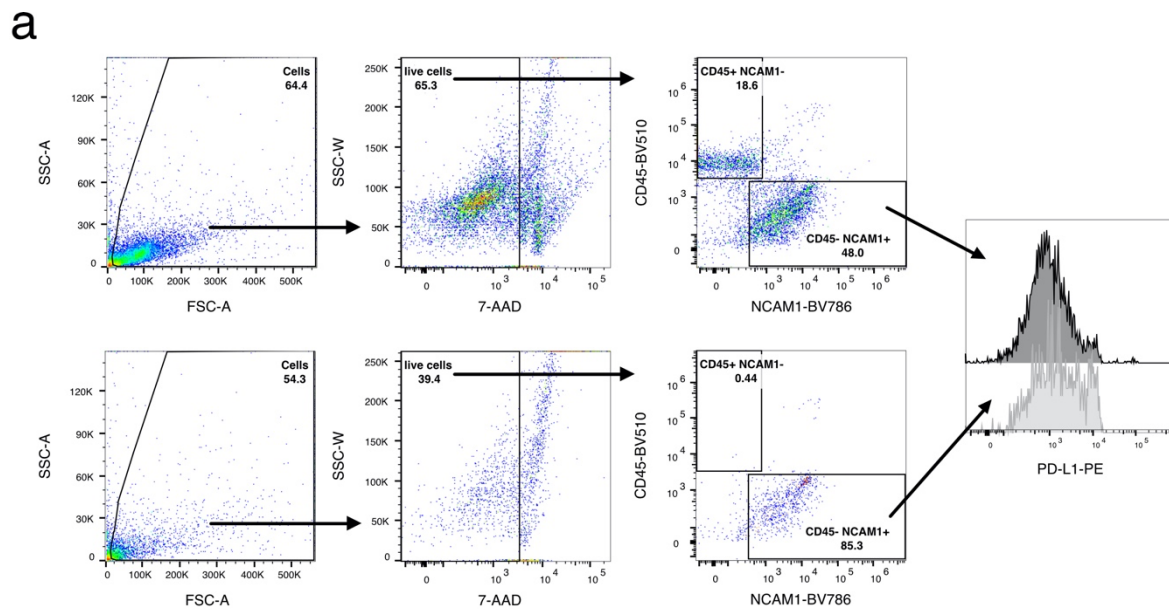
Supplementary Fig. 7: Co-culture of hematopoietic stem and progenitor cells (HSPCs) within organoids does not lead to PD-L1 upregulation. **a** Representative flow cytometry profiles of organoids with stainings and gatings used to distinguish HSPCs (7-AAD⁻CD45⁺NCAM1⁻) from tumor cells (7-AAD⁻CD45⁻NCAM1⁺). **b** Bar plot represents PD-L1 normalized mean fluorescence intensity (MFI) of tumor cells derived from organoids culture in the presence and absence of HSPC for two patients (patient 13, n = 3 technical replicates, patient 17, n = 5). Results are presented as mean ± standard deviation. ns, not significant, two-tailed, unpaired Student's t-test. Source data of b are provided as a Source Data file.
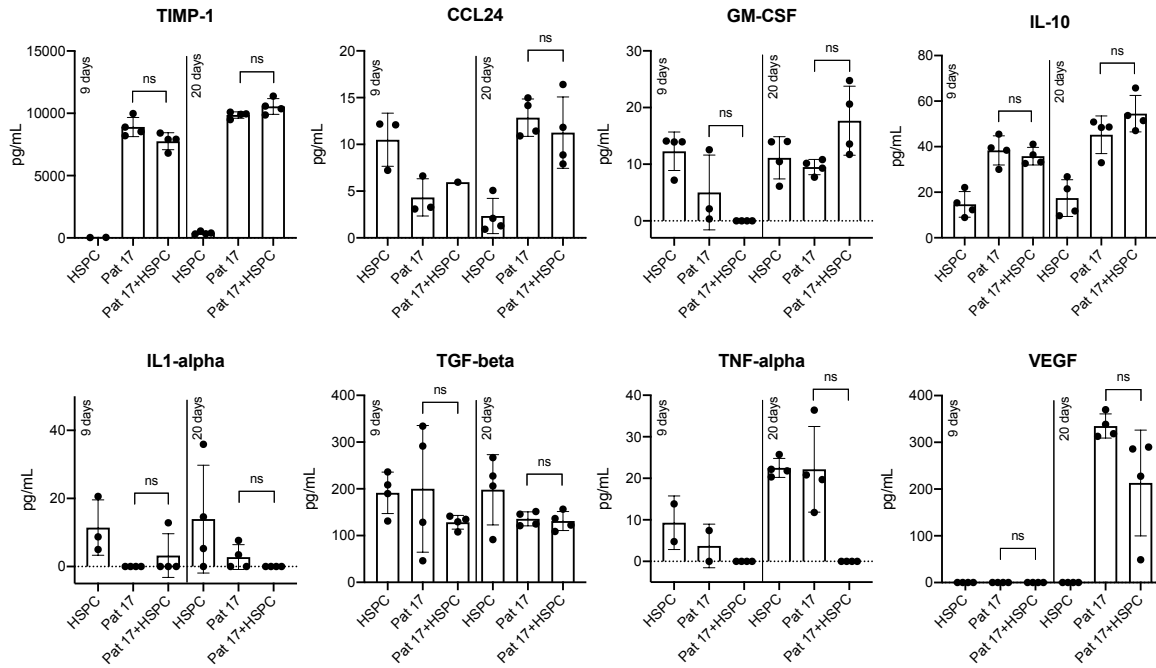
Supplementary Fig. 8: Cytokine ELISA array from conditioned media of co-cultured organoids from patient-derived glioblastoma cells (patient 17) in the presence or absence of hematopoietic stem and progenitor cells (HSPCs). Conditioned media was collected at day 9 and day 20 of co-culture. n = 1–4 technical replicates from one representative experiment of 2. Data are presented as mean ± standard deviation. p values were determined using two-tailed, unpaired Student's t-test corrected with the Benjamini-Hochberg procedure. Source data are provided as a Source Data file. TIMP-1, TIMP metallopeptidase inhibitor 1; CCL24, CC-chemokine ligand 24; GM-CSF, Granulocyte-Macrophage Colony-Stimulating Factor; IL-10, Interleukin-10; IL1-alpha, Interleukin 1 alpha; TGF-beta, Transforming Growth Factor Beta; TNF-alpha, Tumor Necrosis Factor; VEGF, Vascular Endothelial Growth Factor.
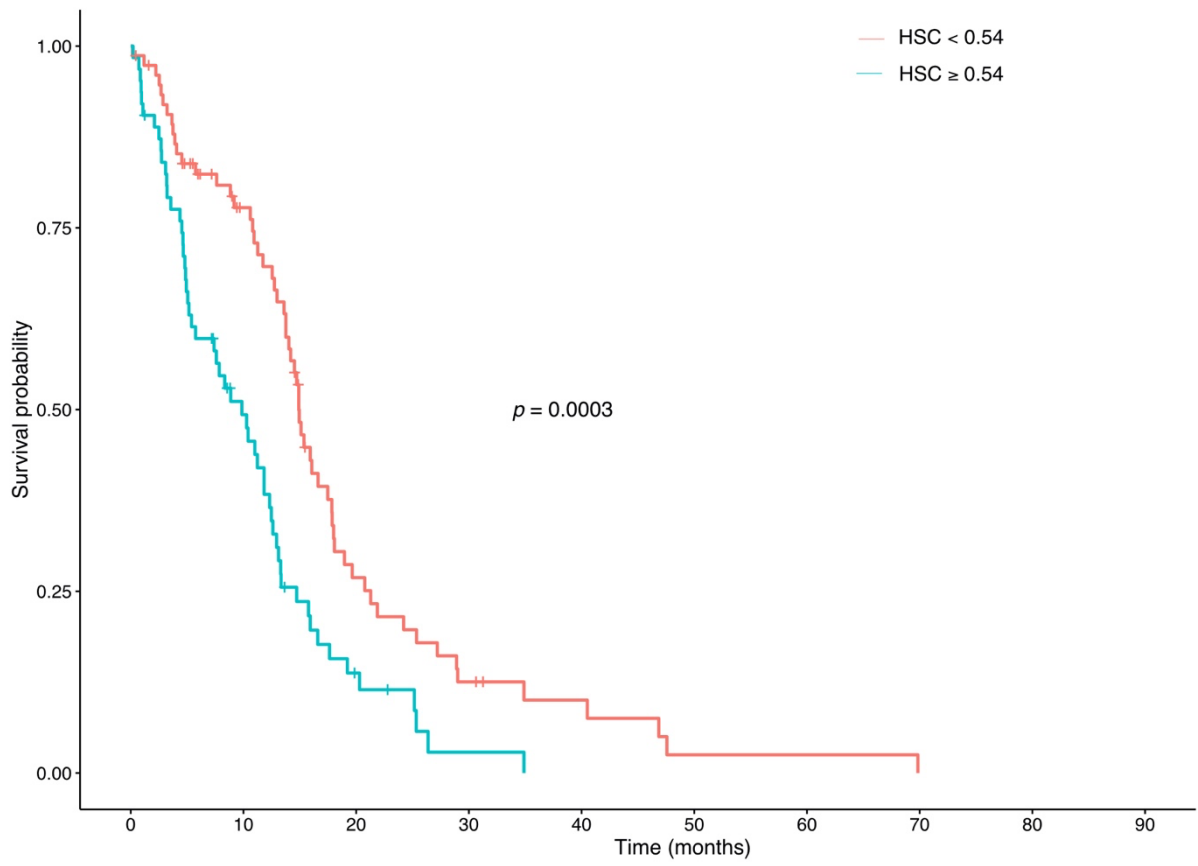
Supplementary Fig. 9: Kaplan-Meier plot of *IDH* wildtype glioblastoma for HSC[high] (*n* = 63) and HSC[low] (*n* = 76) patients using data reported in Figure 6. Two-tailed logrank test. HSC, Hematopoietic Stem Cell.
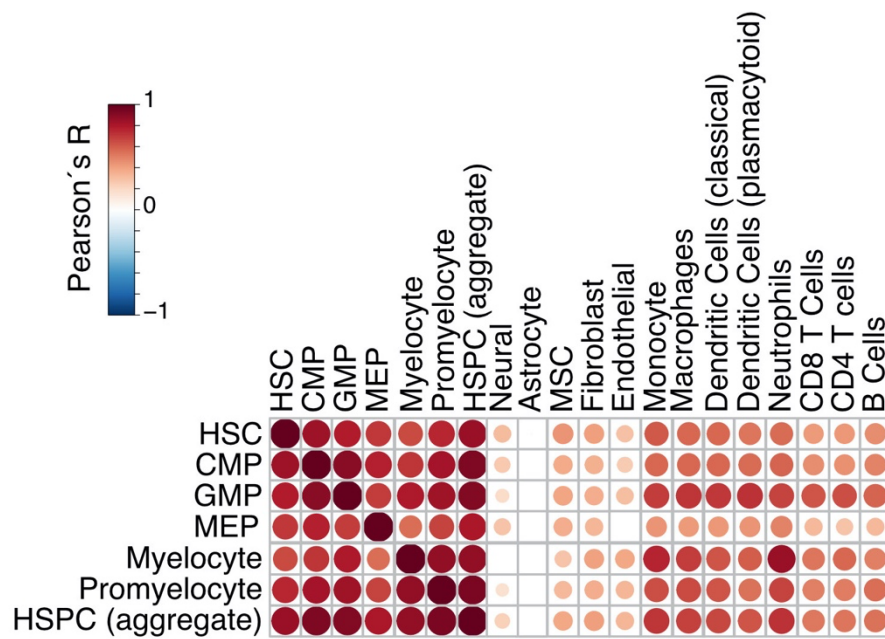
Supplementary Fig. 10: Correlation matrix of HSPC and mature immune cell subsets signals computed by Syllogist on the GBM TCGA dataset. Pearson correlation coefficients with significant values ($p < 0.05$, two-tailed Student's t-test) are shown as circles, with circle size and color matching Pearson correlation coefficients from -1 (blue) to 1 (dark red). Empty squares represent correlation coefficients with $p \geq 0.05$). HSC, Hematopoietic Stem Cell; CMP, Common Myeloid Progenitor; GMP, Granulocyte-Monocyte Progenitor; MEP, Megakaryocyte-Erythroid Progenitor; HSPC, Hematopoietic Stem and Progenitor Cell; MSC, Mesenchymal Stem Cell.

Supplementary Fig. 11: a Gene expression of IL-6 in HSC[high] (*n* = 73) and HSC[low] (*n* = 92) patient samples. **b** Expression of different chemokine ligands and the respective receptors in HSC[high] (*n* = 73) and HSC[low] (*n* = 92) patient samples. In **a** and **b**, boxplots are drawn with boxes representing the interquartile range (IQR), a line across the box indicating the median, and whiskers indicating 1.5 × IQR. Outliers are shown as closed dots. *p* values are determined using a two-tailed Wilcoxon-

Mann-Whitney U test corrected with the Benjamini-Hochberg procedure. HSC, Hematopoietic Stem Cell.

Cumulative Thesis/Extent of Contribution

Cumulative thesis of Ms. Celia Dobersalske

Author contributions

Title:

Cranioencephalic functional lymphoid units in glioblastoma

Authors:

Celia Dobersalske, Laurèl Rauschenbach, Yichao Hua, Christoph Berliner, Anita Steinbach, Anika Grüneboom, Konstantinos D. Kokkaliaris, Dieter H. Heiland, Pia Berger, Sarah Langer, Chin L. Tan, Martin Stenzel, Somaya Landolsi, Flora Weber, Marvin Darkwah Oppong, Rudolf A. Werner, Hanah Gull, Thomas Schröder, Thomas Linsenmann, Andreas Buck, Matthias Gunzer, Martin Stuschke, Kathy Keyvani, Michael Forsting, Martin Glas, Jonathan Kipnis, Dennis A. Steindler, Hans Christian Reinhardt, Edward W. Green, Michael Platten, Alpaslan Tasdogan, Ken Herrmann, Florian Rambow[#], Igor Cima[#], Ulrich Sure[#], Björn Scheffler[#]
[#] These authors jointly supervised

Contributions:

- Conception - 85%: Conception of the study, experiments, revision

- Conduction of experimental work - 80%: Processing of clinical samples, immunoprofiling, *in-vitro* experiments, scRNAseq, and analysis and interpretation

- Data analysis - 90%: Analysis of cells from clinical samples, results from flow cytometry experiments, scRNA analysis, and other collected evidence, creation of all figures

- Species identification – n/a

- Statistical analysis - 75%: Statistical analysis of collected experimental data

- Writing the manuscript - 65%: Original manuscript draft and editing

- Revision of the manuscript - 85%: Concepted and conducted experimental work, manuscript writing and editing during revision of the manuscript, creation of all figures

_____   _____
Signature of the Doctoral Candidate   Signature of the Doctoral Supervisor

Cranioencephalic functional lymphoid units in glioblastoma

Celia Dobersalske[1,2,3], Laurèl Rauschenbach[1,3,4,5,6], Yichao Hua[7], Christoph Berliner[8],

Anita Steinbach[1,2,3], Anika Grüneboom[9], Konstantinos D. Kokkaliaris[10,11,12], Dieter H. Heiland[13,14,15], Pia Berger[1,2,3], Sarah Langer[1,2,3], Chin L. Tan[16,17,18], Martin Stenzel[9], Somaya Landolsi[10,11,12], Flora Weber[9], Marvin Darkwah Oppong[5,6], Rudolf A. Werner[19,20,21], Hanah Gull[1,3,5,6], Thomas Schröder[22], Thomas Linsenmann[23], Andreas Buck[19], Matthias Gunzer[9,24], Martin Stuschke[1,4,25], Kathy Keyvani[26], Michael Forsting[27], Martin Glas[1,4,6,28], Jonathan Kipnis[29,30], Dennis A. Steindler[31,32], Hans Christian Reinhardt[1,4,22,37], Edward W. Green[16,17,18], Michael Platten[16,17,18,33,34,35], Alpaslan Tasdogan[1,4,36,37], Ken Herrmann[1,4,8],

Florian Rambow[1,7,37,38], Igor Cima[1,3,38], Ulrich Sure[1,4,5,6,38], Björn Scheffler[1,2,3,4,37,38]*

*Corresponding author. Email: b.scheffler@dkfz-heidelberg.de

Accepted version

Published version:

Affiliations:

[1]German Cancer Consortium (DKTK), partner site Essen/Düsseldorf, a partnership between DKFZ and University Hospital Essen, University Duisburg-Essen, Essen, Germany.

[2]German Cancer Research Center (DKFZ), Heidelberg, Germany.

[3]DKFZ Division Translational Neurooncology at the WTZ, University Medicine Essen, Essen, Germany.

[4]West German Cancer Center (WTZ), University Hospital Essen, Essen, Germany.

[5]Department of Neurosurgery and Spine Surgery, University Hospital Essen, Essen, Germany.

[6]Center for Translational Neuroscience and Behavioral Science (C-TNBS), University of Duisburg-Essen, Essen, Germany.

[7]Department of Applied Computational Cancer Research, IKIM, University Hospital Essen, Essen, Germany.

[8]Department of Nuclear Medicine, University Hospital Essen, Essen, Germany.

[9]Leibniz-Institut für Analytische Wissenschaften – ISAS – e.V., Dortmund, Germany.

[10]Dr. Senckenberg Institute of Pathology, University Hospital Frankfurt, Frankfurt am Main, Germany.

[11]DKTK, German Cancer Consortium, partner site Frankfurt/Mainz, Quantitative Spatial Cancer Biology Laboratory, University Hospital Frankfurt, Frankfurt am Main, Germany.

[12]Frankfurt Cancer Institute (FCI), Goethe University Frankfurt, Frankfurt am Main, Germany.

[13]DKTK, German Cancer Consortium, partner site Freiburg, Translational Neurosurgery, Microenvironment and Immunology Research Laboratory, University of Freiburg, Freiburg, Germany.

[14]Department of Neurosurgery, University Clinic Erlangen, Germany.

[15]Department of Neurological Surgery, Northwestern University Feinberg School of Medicine, Chicago, USA

[16]CCU Neuroimmunology and Brain Tumor Immunology, German Cancer Research Center, Heidelberg, Germany.

[17]DKTK, German Cancer Consortium, Core Center Heidelberg, Heidelberg, Germany.

[18]Department of Neurology, Medical Faculty Mannheim, Mannheim Center for Translational Neuroscience, Heidelberg University, Mannheim, Germany.

[19]Department of Nuclear Medicine, University Hospital Würzburg, Würzburg, Germany.

[20]University Hospital Frankfurt, Department of Nuclear Medicine, Clinic for Radiology and Nuclear Medicine, Frankfurt am Main, Germany.

[21]The Russell H. Morgan Department of Radiology, Division of Nuclear Medicine and Molecular Imaging, Johns Hopkins University School of Medicine, Baltimore, MD, USA.

[22]Department of Hematology and Stem Cell Transplantation, University Hospital Essen, Essen, Germany.

[23]Department of Neurosurgery, University Hospital Würzburg, Würzburg, Germany.

[24]Institute for Experimental Immunology and Imaging, University Hospital, University Duisburg-Essen, Essen, Germany.

[25]Department of Radiation Oncology, University Hospital Essen, Essen, Germany.

[26]Institute of Neuropathology, University Hospital Essen, Essen, Germany.

[27]Department of Diagnostic and Interventional Radiology and Neuroradiology, University Hospital Essen, Essen, Germany.

[28]Department of Neurology, Division of Neurooncology, University Hospital Essen, Essen, Germany.

[29]Brain immunology and Glia (BIG) Center, Washington University in St Louis, School of Medicine, St Louis, MO, USA.

[30]Department of Pathology and Immunology, Washington University in St Louis, School of Medicine, St Louis, MO, USA.

[31]Steindler Consulting, Boston, MA, USA.

[32]The Eshelman Institute for Innovation, The University of North Carolina at Chapel Hill, NC, USA.

[33]Immune Monitoring Unit, National Center for Tumor Diseases, Heidelberg, Germany.

[34]Helmholtz Institute for Translational Oncology, Mainz, Germany.

[35]German Cancer Research Center-Hector Cancer Institute at the Medical Faculty Mannheim, University of Heidelberg, Mannheim, Germany.

[36]Department of Dermatology, University Hospital Essen, Essen, Germany.

[37]Center of Medical Biotechnology (ZMB), University Duisburg-Essen, Essen, Germany.

[38]These authors jointly supervised this work.

Abstract

The brain tumor ecosystem is considered immunosuppressed, but current knowledge may be incomplete. Here, we analyzed clinical cell and tissue specimens derived from patients presenting with glioblastoma or non-malignant intracranial disease to report that the cranial bone marrow (CB) in juxtaposition to treatment-naive glioblastoma tumors harbors active lymphoid populations at the time of initial diagnosis. Clinical and anatomical imaging, single-cell molecular and immune cell profiling, and quantification of tumor-reactivity identified CD8^{+} T cell clonotypes in the CB that were also found in the tumor. These were characterized by acute and durable antitumor response rooted in the entire T cell developmental spectrum. In contrast to distal bone marrow, the CB niche proximal to the tumor showed increased frequencies of tumor-reactive CD8^{+} effector types expressing the lymphoid egress marker S1PR1. In line with this, cranial enhancement of CXCR4 radiolabel may serve as a surrogate marker indicating focal association with improved progression-free survival. Our data advocate preservation and further exploitation of these cranioencephalic units for the clinical care of glioblastoma.

Main Text

The classic perception of the brain as an immune privileged organ with very limited immune activity is outdated[1]. Recent research connects brain function and immunosurveillance to guardian immune cells assembling on the outer borders of the brain, and our overall view on how brain immunity works in health and disease is currently adjusted. Evidence continues to arise on innate and adaptive immune cells residing within the choroid plexus, the meninges, and the dural sinuses, together acting as neuro-immune interface[2-4]. These immune cells are strategically positioned to sense intracranial cues delivered via interstitial, cerebrospinal, and lymphatic fluid drainage from the brain[1,5]. There are also direct connections between the brain and the meninges provided by bridging veins that cross the intermediary barrier, forming designated arachnoid cuff exit points[6]. This allows immune cell trafficking and hence dynamic and remote control over brain function. As a further extension, the meninges are connected with the overlying skull bone marrow by osseous channels in the calvaria, the superior part of the skull bone[1,6]. These channels contain blood vessels that link the meningeal circulation to the sinusoidal vasculature of the bone marrow. Hematopoietic stem and progenitor cells in the perisinusoidal niches generate erythroid cells, together with lineages of myelocytes and lymphocytes that can traffic through these channels into the underlying meninges[7]. It is therefore not surprising that various intracerebral circumstances foster local hematopoietic responses. This is, for example, evident by the altered egress of myeloid and B cells from the skull bone marrow to the meningeal borders in animal models of brain injury, inflammation, and aging[1,7].

As our understanding of immunosurveillance in the brain continues to evolve, we can learn much from its disruption during malignant disease, for example from glioblastoma, the most malignant adult brain cancer, that remains uniformly lethal with a median survival of less than two years[8]. Immune checkpoint inhibiting immunotherapies have proven to be of limited effect in patients with glioblastoma. Several immunosuppressive resistance mechanisms are considered to be in place. These may involve systemic immunosuppression, including prevention of immune cell infiltration via the blood-brain-barrier, sequestration of immune cells in the bone marrow, or iatrogenic destruction of peripheral immune cells[9]. In addition, cycles of intrinsic, adaptive, and acquired mechanisms of immunotherapy resistance are discussed, based on the heterogeneous molecular subtypes of the tumor, the exhausted nature of infiltrating T cells, and the tumor-promoting effect to reprogram myeloid cells in the microenvironment[9,10]. While these factors are extensively studied within the tumor

parenchyma, the involvement of adjacent structures of the neuro-immune interface remains unknown. Specifically, the skull bone is less intensely studied in adult humans compared to animal models, and it is far more difficult to access than the marrow of routinely evaluated hip bone[11]. Because bone marrow sites shrink with increasing age in the human body[12],

40   substantial hematopoietic activity was per se not expected in the cranial bone of a disease that frequently affects advanced stages of life. In this study, we explored the immune cell repertoire within the marrow of the cranial bone (CB) to assess their prevalence and disease-related function as a cranioencephalic unit.

45   **Results**

Cranial enrichment of immune cells in glioblastoma

We used the radioligand [^{68}Ga]Ga-Pentixafor as a clinical surrogate marker of immune cell presence in the CB, as it is known to act as a CXCL12 analogue that binds the C-X-C motif chemokine receptor 4 (CXCR4) protein enriched in hematopoietic/immune cell niches *in*

50   *situ*[13].We analyzed 19 patients with glioblastoma (aged 50 to 83 years, median = 69 years; Supplementary Table 1) in a presurgical setting by positron emission tomography (PET). Comparing with PET data derived from six patients with Conn's syndrome (aged 42 to 67 years, median = 50 years; Supplementary Table 2) as a control, we noted a pronounced labeling in the CB of the patients with glioblastoma (Extended Data Fig. 1). This was contrary

55   to our expectation that the bone marrow of the older glioblastoma patient cohort would be populated by aged hematopoietic cells with a reduced regenerative potential and consequently lower CXCR4 levels[12]. The pattern of Pentixafor radiolabeling frequently extended from the known accumulation within the tumor parenchyma[14] to the adjacent tracer in the bone via ipsilateral association with bridging meningeal structures (Fig. 1a,b). Connections from the

60   various intracerebral tumor locations to the choroid plexus or the dural sinuses were not observed (Fig. 1c and Supplementary Video 1).

      Intrigued by this finding, we accessed surplus fragments of fresh bone chips derived from craniotomies under informed consent (Fig. 1d). The surgical approach of a craniotomy adjacent to the intracerebral tumor mass is indicated (i) to derive tissue for routine diagnosis

65   and (ii) for tumor resection according to the guideline-based standards of care[8]. We used whole-mount three-dimensional light-sheet fluorescence microscopy[15] to expose the spongy diploë within the flat bones in which marrow characteristically resides (Fig. 1e). Samples from patients with non-malignant intracerebral disease (n = 5, aged 50 to 83 years, median = 77 years; Supplementary Table 2) consistently displayed ageing marrow[12] (Fig.

70   1f,g; Supplementary Video 2 and Extended Data Fig. 2), while the diploë of patients with glioblastoma contrasted with aggregates of immune cells (n = 6, aged 45 to 80 years, median = 60 years; Supplementary Table 1). We observed extended patches of CD45$^+$ cells forming solid arrangements around microvessels in the cancellous bone (Fig. 1h,i and Supplementary Videos 3 and 4). Quantitative multiplex immunofluorescence imaging on

75   large tissue sections confirmed the observation and further revealed bone marrow-typic spatial vicinity of CXCR4 and CXCL12 in the CB (Fig. 1j,k and Extended Data Fig. 2). These data indicated a co-morbid process where immune cells accumulate nearby, in the proximal cranial bone of patients with glioblastoma.

80   *CD8$^+$ effector memory T cells delineate vivid immunopathology*

Prior landscape analyses of the glioblastoma microenvironment have not considered immune cell niches in the cranial bone, e.g.,[16-19]. Therefore, we extracted CD45$^+$ immune cells by magnetic-activated cell sorting from craniotomy-derived fresh surgical bone, and for comparison, from peripheral blood mononuclear cells (PBMC) and from fresh glioblastoma

85   tissue to obtain their single-cell RNA sequencing (scRNA-seq) profiles (Fig. 2a,b). The integrated space of scRNA-seq data served as a source for marker-based cell type annotation (Fig. 2c and Extended Data Fig. 3a-c). We complemented these data by flow cytometric immunoprofiling of freshly isolated CD45^{+} cells (Fig. 2d and Extended Data Fig. 4a). Considering the importance of myeloid cells in contributing to immunosuppression in

90   glioblastoma, and despite the preclinical evidence of skull bone marrow as a potential source of such cells[1,7], we could not identify increased frequencies of myeloid cells in the CB, whereas these were abundant in the tumor (Extended Data Fig. 4b). scRNA-seq data suggested that CB-derived myeloid cells were mostly naive monocytes, whilst those in the tumor were predominantly anti-inflammatory monocytes and macrophages (Extended Data

95   Fig. 5a-c), the latter consistent with recent findings[20,21]. Subsequent cytometry further confirmed a low proportion of potential monocytic-myeloid derived suppressor cells in CB samples (Extended Data Fig. 5d,e). By contrast, we surprisingly noted abundant T cell fractions among the immune cells derived from CB (Extended Data Fig. 4b).

100   We paired scRNA-seq and V(D)J sequencing (scVDJ) to our biosampling strategy and noticed shared clonotypes with the tumor along with an accumulation of effector-type CD8 transcripts within the CB (Fig. 2e,f). Quantitative phenotyping of CD8^{+} T cells confirmed consistently increased prevalence of effector memory (T_{EM}) phenotypes in CB (Fig. 2g-i; Extended Data Fig. 4c-e). Considering that bone marrow can be a priming site for T cell response[22] and speculating on a distinct spatial relationship of cranial CD8^{+} T cells with the

105   adjacent encephalic tumor mass, we asked if the proximal CB of patients with glioblastoma contained tumor-reactive cells. Hence, freshly isolated T cells were briefly expanded, magnetically sorted for CD8^{+} T cell populations and used in functional enzyme-linked immunospot (ELISpot) assays upon physical contact with autologous glioblastoma cells (Fig. 2j). Relying on the secretion of interferon-gamma (IFNγ) we repeatedly observed increased,

110   MHC-dependent tumor reactivity of cranial bone CD8^{+} T cells versus paired samples from tumor or peripheral blood (Fig. 2k,l). This indicated an increased presence of tumor-reactive CD8^{+} T cells in the proximal cranial bone, which together with abundant effector memory phenotypes might resemble an acute immunological response[23].

       However, the observation of lower responses from intra-tumoral CD8^{+} T cells

115   challenged our perception of re-circulating tumor-reactive T cells. Noting that tumor-derived T cells did not completely lack antigen specificity, however, we next considered the co-existence of increasingly exhausted T cell phenotypes from the tumor parenchyma in comparison to CB at the early stage of disease.

120   *Developmental trajectory of CD8^{+} T cell profiles*

    We compared intraindividual levels of T cell proliferative capacity and tumor reactivity using freshly isolated and expanded CD8^{+} T cells from tumor, CB, and peripheral blood of six patients with glioblastoma. In a pilot experiment, we monitored T cell aggregation as a hallmark of T cell activation observing that tumor-derived T cells were incapable of

125   expansion upon repeated stimulation while CB-derived samples maintained their proliferative potential (Fig. 3a). Standardized assessment established a resilience score for every sample indicating the continued reproductive capacity of T cell populations during three times of re-stimulation for 14 days, interrupted by resting periods of 7 days. Every CB-derived sample passed the test while 4/6 of the tumor-pendants failed (Fig. 3b). We noted comparable

130   resilience of CB- and PBMC-derived CD8^{+} T cells including a sustained ability to reproduce memory and effector T cell subsets in the experimental course (Fig. 3c and Extended Data Fig. 6a). Furthermore, we observed an endured antitumor response of cranial bone CD8^{+} T cells, evident by MHC-dependent tumor reactivity that continued to surpass the levels of

paired tumor- and PBMC-derived populations after rounds of re-stimulation in the assay (Fig. 3d).

To better comprehend the basis of resilience and durability of the cranial bone T cell response, we subclustered our scRNA-seq data focusing on the transcriptomes of n=18,973 CD8^{+} T cells collected from eight patients with glioblastoma and, as control, from five patients with non-malignant intracranial disease (Fig. 3e and Extended Data Fig. 3d-f; Supplementary Table 1 and 2). We found characteristic patterns of phenotypes by comparing the various sources of samples. In line with our hypothesis, we determined the exhausted phenotype in more than a third of tumor-derived CD8^{+} T cells, far more prominent than in the CB- or PBMC-populations. We also noted distinct cellular identities enriched in the CB of patients with glioblastoma (CBe; Fig. 3f). Further study of the cranial bone subspace (n = 6,743 cells) revealed the entire T cell developmental spectrum by Palantir. This employs diffusion map-based dimensionality reduction to better represent the differentiation trajectory of cells[25]. CytoTRACE and Pseudotime analyses, which are used to infer cellular differentiation states and dynamics of lineage specification[26,27], confirmed the impression. The CBe CD8^{+} T cells mapped along the entire axis of Palantir-ordered phenotypes (Fig. 3g). Speculating on the presence of a distinct functional state, we benchmarked our data to recently introduced comprehensively curated T cell gene profiles[28]. This revealed anti-apoptotic and stress-related signatures, particularly enhanced in the CBe CD8^{+} T cells from cranial bone and tumor niches (Fig. 3h). Comparable response states of tumor-infiltrating T cells were recently discussed in association with some of the most aggressive types of cancer[29]. By direct comparison, we found a broader developmental range of CD8^{+} T cell differentiation in the CB compared to tumor-derived samples, while CBe phenotypes from the two niches showed a similar distribution of developmental potential (Extended Data Fig. 7). The combined data suggested the CB as a unique niche in glioblastoma serving as a major site for differentiation of tumor-associated durable effector T cell subsets. In line with this assumption, we found an intriguing enrichment of the Activation:Effector function signature among the effector phenotypes in the CB (Fig. 3i), further promoting the concept of a locally driven acute CD8^{+} T cell response at this early stage of disease.

Antitumor effect of CD8^{+} T cells from proximal cranial bone

To substantiate our observation of accumulating activated effector T cell types in the tumor-adjacent CB, we next considered the potential formation of tertiary lymphoid structures (TLS). TLS are known to form in association with numerous cancer types[30]. The simultaneous presence of T cells and B cells was suggestive, but their weak structural organization in the diploë of patients with glioblastoma and the lack of characteristic single-cell gene signatures for the detection of fully developed TLS[30] did not support the premise (Extended Data Fig. 8). On the other hand, CXCR4-CXCL12 have recently been shown to contribute to enhanced bone marrow accumulation of CD8^{+} T_{EM} and other types of memory T cells, at least during transient nutritional stress periods[31]. To assess this aspect, we collected a limited set of additional samples from the distal hip bone marrow (dBM) during neurosurgery of treatment-naive, newly diagnosed patients with glioblastoma. Comparing acutely isolated samples derived from CB and dBM we found similar relative frequencies of T_{EM} while CD8^{+} T cell fractions were increased in the CB of patients with glioblastoma, albeit not significant (Fig. 4a). We next studied the presence of sphingosine 1-phosphate receptor 1 (S1PR1 or S1P1) by cytometry observing, in contrast to dBM, increased levels on T cells from the CB, particularly on the prominent CD8^{+} effector types. Among the memory-like T cells, S1PR1 was most abundant in T_{EM} (Fig. 4b,c and Extended Data Fig. 6b,c). This finding could not be anticipated from previous clinical evidence on naive T cells sequestering in the dBM at the initial stages of glioblastoma[11]. It rather suggested increased lymphoid egress[32] from the CB

(Fig. 4d) encouraging a more granular investigation of antitumor effects elicited by T cells from the cranial niche.

Comparing tumor-reactivity from bulk CD8$^+$ T cell populations of CB versus dBM, we noted intra-individual differences in IFNγ release and tumor cell-killing ability (Fig. 4e-g). Utilizing scVDJ data of acutely isolated samples (Extended Data Fig. 9), we next employed the recently introduced AI-based algorithm predicTCR[33] to classify tumor-reactivity on a single cell level and to map their clonal distribution in the shared environments. We determined a substantial enrichment of CD8$^+$ clones predicted to be tumor-reactive in the CB as compared to peripheral blood and dBM that almost paralleled the frequency in the tumor niche (Fig. 4h,i). Enriching the analysis with phenotype information (Fig. 4j), we found that shared clones predicted to be tumor-reactive (Fig. 4k) predominantly consist of activated and effector types in the CB versus exhausted phenotypes in the tumor (Fig. 4l). Intriguingly, we identified almost the same frequencies of tumor-reactive cells among the shared clones in CB and tumor, which might indicate that their proximity allows most efficacious trafficking between the sites. Pilot evidence for the validity of this assumption was derived from the re-assessment of PET-CT/MRI-specific radiological measures of Pentixafor in patients with glioblastoma (Fig. 4m). Among the considered parameters (Extended Data Fig. 10), only cranial/calvarial enhancement of the CXCR4 radiolabel (Fig. 4n) showed a positive correlation with improved patient outcome (Fig. 4o). Thus, the clinical imaging data that we used as an entry route into this investigation might have already contained prognostic information. Together, we interpret these findings as indicative of an immediate clinical effect mediated by an early response of tumor-reactive CD8$^+$ T cells in the CB niche and their shared clonotypes in the glioblastoma tissue.

Discussion

By combining state-of-the-art research techniques with an unconventional clinical sampling strategy, we exposed and validated tumor-associated CD8$^+$ T cells in the CB of newly diagnosed, treatment-naive glioblastoma. Their effector types are characterized by an endured tumor response, and, compared to cells from the dBM, by an increased expression of the lymphoid egress marker S1PR1. Re-circulation between the proximal bone and tumor tissue is evident by the presence of shared tumor-reactive clonotypes. CXCR4 radiolabeling in the CB, in juxtaposition to the tumor, might serve as a surrogate marker indicating an association with patient survival.

Previously described low numbers of infiltrating immune effector cell types in the tissue of brain tumors have manifested the perception of a "cold immune phenotype"[10]. Current observations of clonally expanded T cells with effector properties in pediatric brain tumors[34] and our clinical discovery of tumor-reactive CD8$^+$ clonotypes in the CB, also shared with the tumor tissue of adults challenge this concept. The accumulation of CD8$^+$ T$_{EM}$ in the proximal bone is particularly intriguing, because this population of immune cells is associated with durable antitumor response in solid cancers[35,36].

Even though it has been known that the bone marrow is a major reservoir and site of recruitment for memory CD8$^+$ T cells and thus could host early immune responses[22,37], brain tumor-reactive T cells have not yet been reported in this niche. Rather, sequestration of naive T cells was described in the distal marrow[11]. This suggests that proximity plays a conceptual role in the process of early anti-tumor response, at least in the brain. We note as well that analysis of deep cervical tumor-draining lymph nodes in mouse models of glioblastoma showed mixed evidence of CD8$^+$ tumor-reactive T cells[38-40], suggesting that the proximal CB, in closer anatomical connection to the neuro-immune interface, may be the primary target for tumor-reactive T cell recirculation and T cell memory formation in humans.

The comprehensive exploration of CD8^{+} T cell differentiation trajectories and their cellular origins in the aged human marrow microenvironment will remain an endeavor.

235 Further access to the niche is required to fully comprehend what presently may appear as a brain tissue-specific constellation of mechanisms of immunopathology. Advanced characterization of T cells, e.g.,[28,33,41,42] may serve as strategy to uncover inherent biomarkers in the dynamic course of disease and will facilitate the development of innovative diagnostic tools. Tumor-adjacent bone material as a rich source of non-exhausted tumor-reactive T cells

240 may also have implications for the improvement of interventions, e.g., related to local engaging of T cells, cellular therapies, or tumor vaccination[43-47].

Our observation was made at the time of initial diagnosis, before the onset of treatment, and may explain the survival benefit and the increase of clonal T cell diversity observed in patients with glioblastoma undergoing neoadjuvant immunotherapy, compared to

245 patients that were treated in the adjuvant setting[48,49]. Consequently, patients with an intact immunological axis, as seen in the neoadjuvant setting before craniotomy, may have a higher likelihood of responding to immunotherapy. This hypothesis is supported by the reported phenomenon, present in about one-third of newly diagnosed glioblastomas, where tumors remained stable or even decreased in volume in the waiting period between the initial

250 diagnostic and preoperative MRI scans[50]. Therefore, the integrity of these cranioencephalic units may be pivotal for the support of immunotherapy. The preservation of these niches during treatment would require deviation from current guideline-based standards of care that enforce the transient removal of the proximal bone during neurosurgery and penetration of the site with radiotherapy[8]. Further investigation is warranted to determine the role of intact

255 cranioencephalic units during neoadjuvant immunotherapy, requiring prospective collection of tissues from paired cohorts of primary and relapsed patients with glioblastoma. Such approaches would also yield mechanistic insight into the clinical surrogate marker CXCR4, paralleling previous preclinical work[31], or provide a basis for the future development of alternative imaging-guided biomarkers.

260 Limitations of our work include the discovery-phase data restrictions on the clinical course. This data requires validation through recruitment of a broad, balanced patient cohort in the prospective setting. The identity and potential clinical impact of CBe T cell states were not addressed here and need to be referred to future investigations. Interestingly, similar cell states were previously linked to immunotherapy resistance[29]. The role played by immune cell

265 subsets other than CD8^{+} T cells warrant as well further in-depth studies along the course of disease in glioblastoma. Another interesting aspect that we did not address was the identity and the potential clinical impact of shared CD8^{+} T cell clones between tumor and dBM. Lastly, our study focused solely on glioblastoma but future investigations should be expanded to other intracerebral diseases.

270 In conclusion, the glioblastoma-linked immune cell niche in the human skull provides an unanticipated resource and concept of acute tumor reactivity in the proximal bone marrow. Our data advocate preservation and further exploitation of this niche and its attendant cranioencephalic units.

275

Acknowledgments

Author contributions

Conceptualization: CD, FR, IC, US, BS
Data curation: CD, LR, YH, CB, AS, AG, KDK, DHH, CLT, RAW, TL, IC, FR
Formal Analysis: CD, LR, YH, CB, AG, KDK, DHH, CLT, RAW, EWG, MP, AT, IC, FR, BS
Funding acquisition: KDK, DHH, IC, KH, US, BS

Investigation: CD, LR, YH, CB, AS, KDK, DHH, PB, SLang, CLT, MSte, SLand, FW, RAW, IC, FR

Methodology: CD, LR, YH, CB, AG, KDK, DHH, CLT, MSte, AB, HCR, EWG, MP, AT, KH, IC, FR, US, BS

Project administration: CD, LR, BS

Resources: LR, MDO, HG, TS, TL, AB, MGu, MStu, KK, MF, MGl, HCR, MP, KH, US, BS

Supervision: AG, JK, DAS, AT, KH, FR, IC, US, BS

Visualization: CD, LR, YH, CB, AG, KDK, DHH, IC, BS

Writing – original draft: CD, BS

Writing – review & editing: CD, LR, YH, CB, AS, AG, KDK, DHH, PB, SLang, CLT, MSte, SLand, FW, MGu, MStu, MF, MGl, JK, DAS, EWG, MP, AT, KH, FR, IC, US, BS

Competing Interests:

Tables:

None in the main text.

355
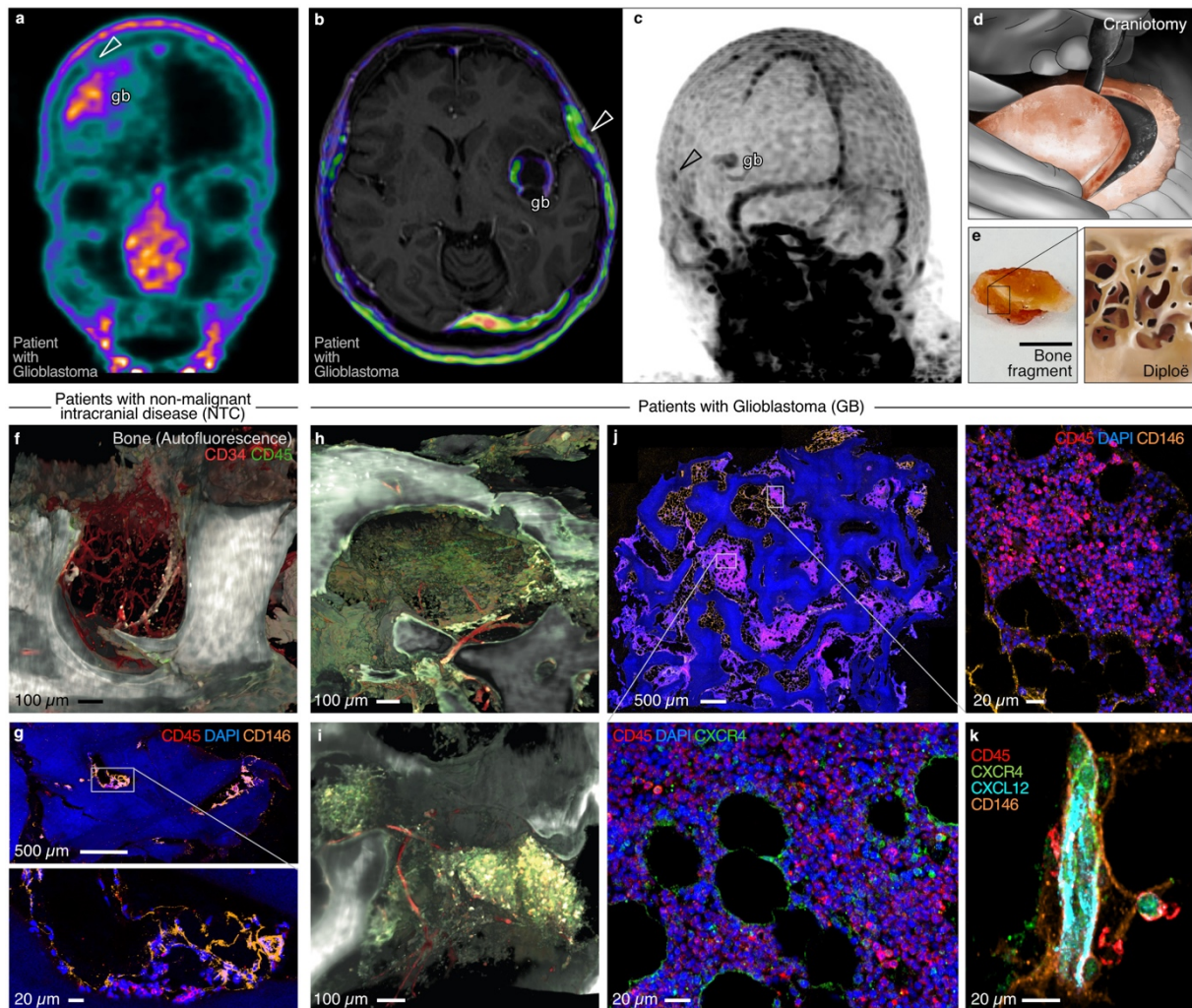
Fig. 1: Glioblastoma-associated enrichment of immune cells in the cranial bone. **a**, Clinical PET-computed tomography (PET-CT) visualizing radiolabeled CXCR4 in a coronal plane (patient 1). Arrowhead depicts focal contact between glioblastoma parenchyma (gb) and superficial cranial/meningeal compartment. Additional findings include demarcation of the nasopharyngeal mucosa and parts of Waldeyer's pharyngeal ring. **b,** Clinical CXCR4 PET-CT in an axial plane (patient 2). Secondary fusion with magnetic resonance imaging (MRI) exposing brain anatomy and the connecting meningeal structures. Arrowhead depicts nodular enhancement ipsilateral to the gb. Note the lower unconnected radiolabeling of the dural sinus. **c,** 3D-reconstruction of PET-CT data from (b). Arrowhead marks focal CXCR4 radiolabeling in the cranial bone in juxtaposition to the intracerebral gb. Note the unconnected aspects of the neuro-immune interface of the dural sinus and bystander radiolabeling of the head and neck lymphatic system. **d,** Schematic representation of a craniotomy. **e,** Photograph of a representative fresh bone specimen used for the study (scale bar: 5 mm). Magnified inset: drawing of inner spongy structure. **f,** 3D-rendering of light-sheet microscopy data obtained from whole-mount preparation of fixed and optically cleared clinical CB (patient c3). Note the empty aspect of fatty, aged marrow. **g,** Immunofluorescent confocal image of CB tissue section showing microvessels (CD146+) and limited presence of immune cells (CD45+) in the diploë of patient c7 (total n=5 patients with non-malignant intracranial disease, Extended Data Fig. 2). **h-i,** Light-sheet microscopy data as in (f), showing accumulation of CD45+ immune cells surrounding CD34+ microvessels in the diploë of patients with glioblastoma (**h,** patient 7; i**,** patient 6). **j,** Immunofluorescent confocal image, as in (g), demonstrating morphological appearance of tumor-associated bone cavities and accumulating immune cells (patient 12; total n=4 patients, Extended data Fig. 2). Insets detail immune/hematopoietic cell clusters (CD45+) and CXCR4 labeling within. **k,** Multicolor immunofluorescent confocal image capturing close proximity of CXCL12 to CXCR4+ cells in a CB tissue section of patient 13 (total n=2 patients, Extended Data Fig. 2). Scale bars as indicated.
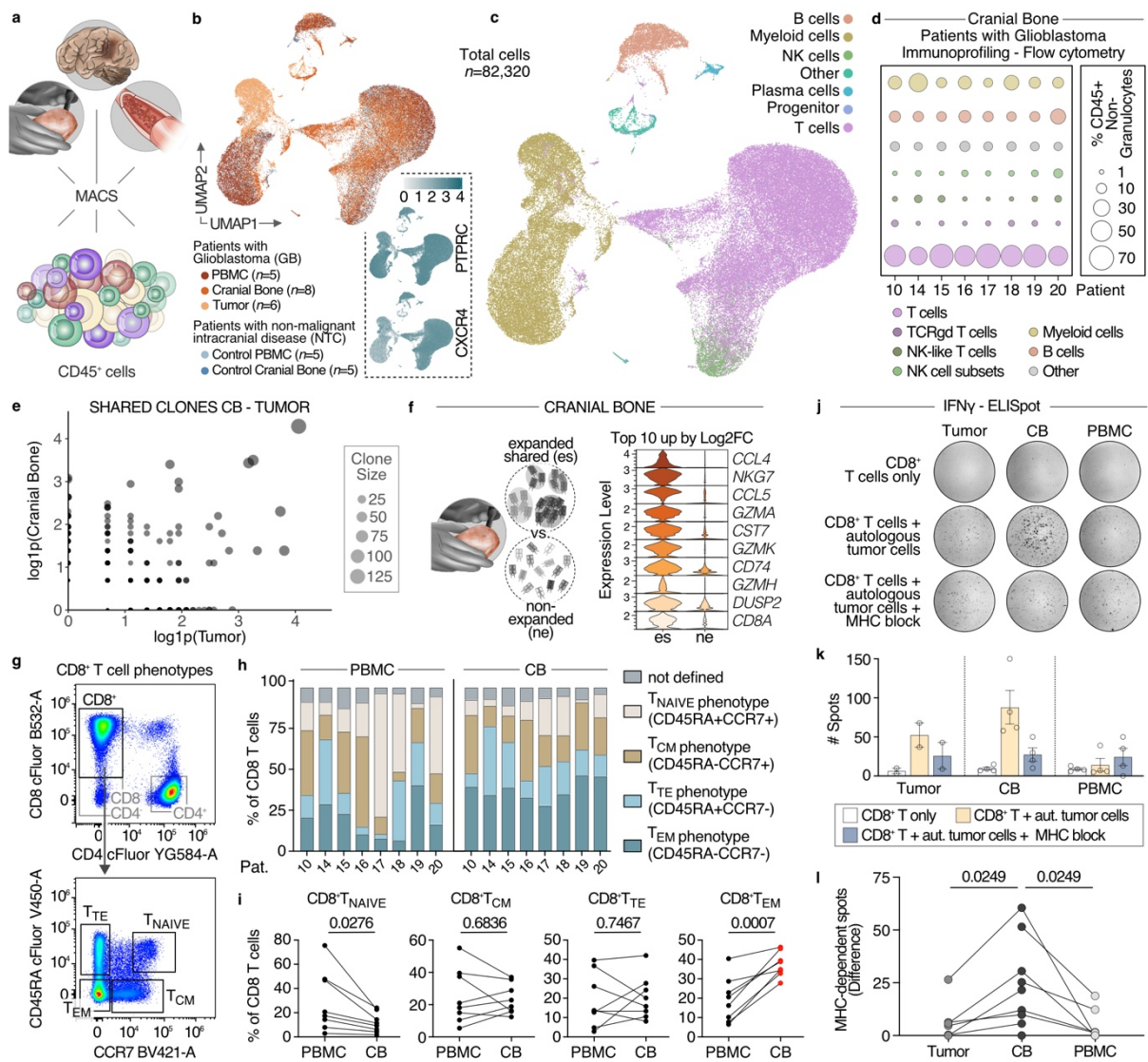
Fig. 2: Cranial bone cellular immune profile. a, Schematic depicts sources of CD45$^+$ immune cells. **b,** Uniform manifold approximation and projection (UMAP) of integrated scRNA-seq data from CD45 (*PTPRC*)-expressing immune cells. Tissue sources color coded, numbers (n) of biosamples indicated per source. Insets visualize expression of selected genes. **c,** Overlay of SingleR- and marker-based annotation of cell types. **d,** Bubble plot summarizing prevalence of immune cell subsets among CD45$^+$ non-granulocytes, by flow cytometry. **e,** Scatter plot of scVDJ data from n=3 patients with glioblastoma visualizing shared T cell clonotypes between CB and tumor. Clone size visualized by number of cells per clone, each point represents a unique clone. Axes: log-transformed counts of cells (log1p). Exclusive CB- or tumor-clones plotted along y-or x-axis, respectively. Shared clones located in the central area of the graph. **f,** Top ten differentially expressed genes (ranked by Log2FC) comparing tumor-shared expanding clonotypes vs. non-expanding singlets in the CB. DEGs detected by FindMarkers() Seurat function, per default setting (two-sided Wilcoxon rank sum test). Gene expression cutoff set to a minimum of 20% of cells. **g,** Gating strategy for profiling of CD8$^+$ T cell phenotypes: T_{TE}, terminal effector; T_{EM}, effector memory; T_{CM}, central memory. **h,** Stacked bar plot indicating phenotype distribution per patient and niche from listed patients with glioblastoma. **i,** Graphs show frequencies of phenotypes in paired samples. Two-tailed paired t-test: p values indicated (n=8 patients). **j,** Photomicrographs depict exemplary patterns of ELISpots using an INFγ-based readout. **k,** Exemplary distribution of raw data from available expandable cells of one paired ELISpot analysis (patient 15, data points represent technical replicates per source). Data as mean ± SEM. **l,** Graph summarizing mean data of major histocompatibility complex (MHC)-dependent IFNγ spots obtained from samples of patients with glioblastoma (n=9). Two-tailed, paired t-test with p values corrected for multiple comparisons (Benjamini-Hochberg method).
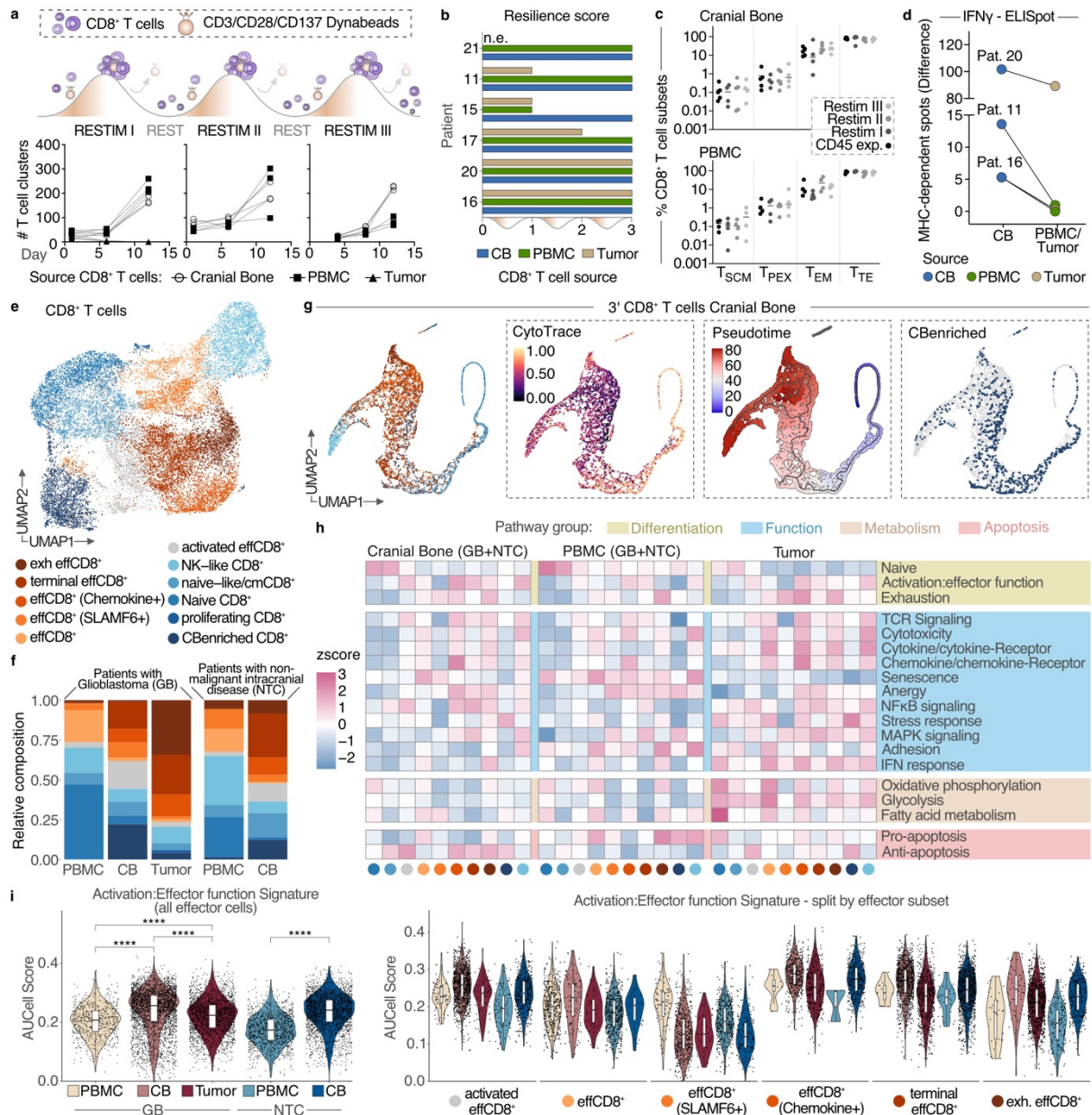
Fig. 3: Developmental trajectory of CD8⁺ T cell response. a, Illustration of experimental approach used to monitor T cell aggregation. Expanded CD8⁺ T cells were re-stimulated (RESTIM) and allowed to rest in intermediary phases. Graphs display quantification of clusters forming at indicated time points, n = 3 technical replicates, patient 11. **b,** Resilience assay. Data represent successful rounds of re-stimulation. Experiment conducted in triplicates per patient and source. n.e., not expandable. **c,** Sub-analysis of (b). Distribution of CD8⁺ T cell phenotypes by cytometry after indicated stage of stimulation (CD45 exp.) or re-stimulation (Restim I-III). Data points represent n=4 or n=5 biological replicates per condition. T cells: T_{SCM}, stem-like; T_{PEX}, progenitor exhausted; T_{EM}, effector memory; T_{TE}, terminal effector. **d,** ELISpot data of specified CD8⁺ T cells after two (patient 20) or three (patients 11 and 16) rounds of re-stimulation in response to autologous tumor cells. Graph summarizing mean data of MHC-dependent IFNγ spots (n=3 patients), paired samples indicated. **e,** UMAP of scRNAseq CD8⁺ T cell data, color-coded by annotated cell type. **f,** Stacked plot of CD8⁺ T cell data separated by condition and tissue source. CBe T cell types in dark-blue. **g,** UMAP of 3' GEX CB data from (e) generated by Palantir, based on diffusion map dimensionality reduction, color-coded as in (e). Left: continuous CytoTRACE score, from 1 (highest) to 0 (lowest) level of plasticity. Center: Pseudotime calculation transitioning from blue (start) to red (end), root state manually defined. Right: CBe T cell distribution in the UMAP. **h,** Heatmap visualizing z-scores of AUCell scores calculated using external gene signatures[28] across CD8⁺ T cell phenotypes from (e). **i,** Violin plot showing Activation:Effector function signature intensities (AUCell score) in the effector CD8⁺ T cells subtypes of (h), split by niche and T cell subset. Boxplots display median, quartiles, and values within 1.5 * interquartile range as whiskers. Biological replicate data from (n) patients: GB-PBMC (5), -CB (8); -Tumor (6); Control-PBMC (5), -CB (5). Significance calculated by two-sided Wilcoxon rank sum test with adjusted p value using Holm correction (SeuratExtend); absolute values provided in Supplementary Table 3. ****p<0.0001.
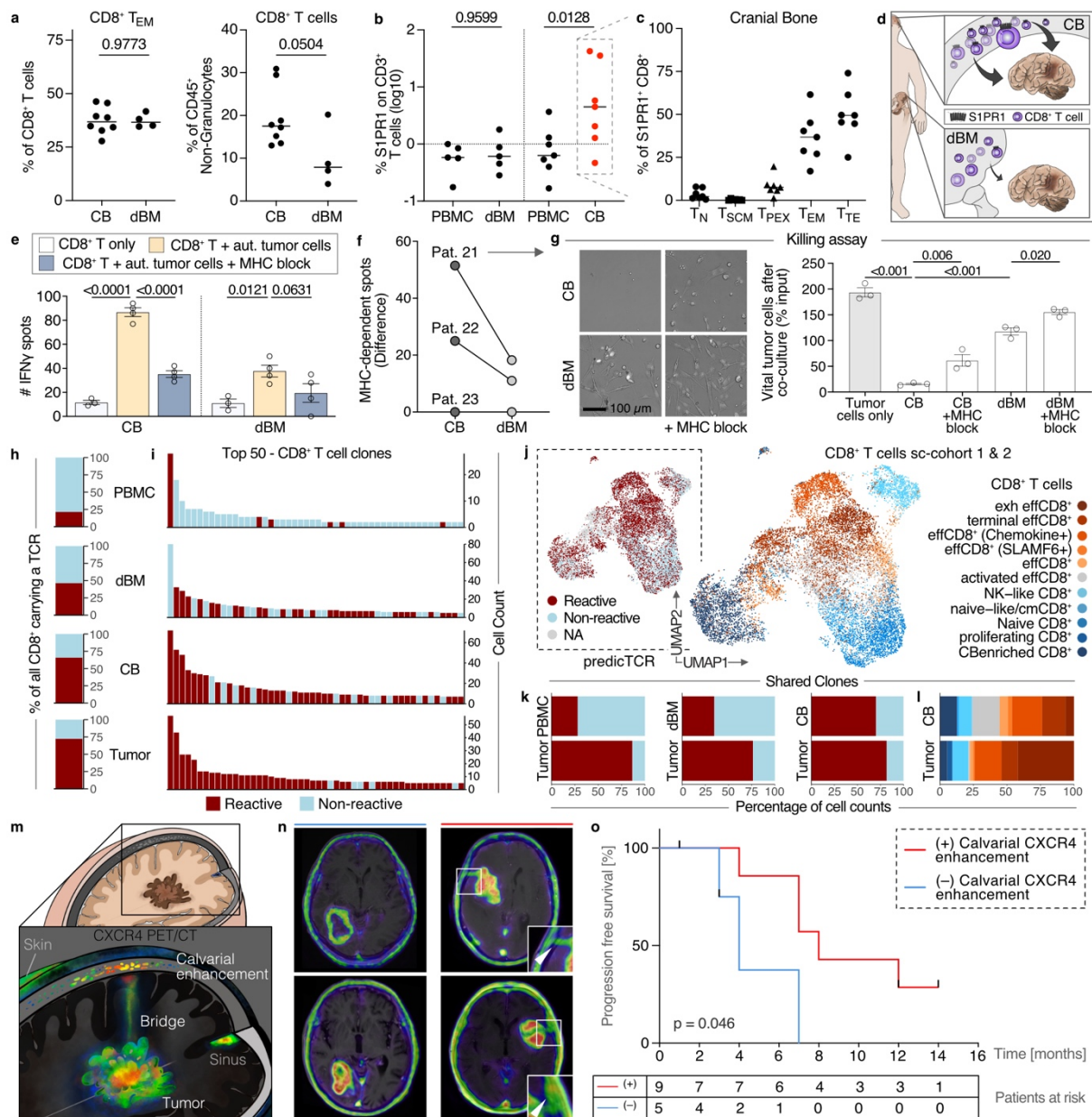
425 **Fig. 4: Distinctive features of CD8⁺ T cells in the proximal bone marrow.** a-c, Lines indicate median, p values specified, (n) patients analyzed. **a,** Cytometry of CD8⁺ T cells from CB (8) and dBM (4). Two-tailed unpaired t-test. **b,** Cytometric S1PR1 levels from freshly isolated PBMC vs. dBM (5); PBMC vs. CB (7) samples of patients with glioblastoma. One-way ANOVA corrected for multiple comparisons (Šídák test). **c,** Phenotype frequency among CB-derived S1PR1⁺CD8⁺ cells (n=7). **d,** Schematic concept. **e,** ELISpot data, split by source (patient 21).

430 Technical replicates shown as individual dots. Mean values ± SEM; Two-way ANOVA corrected for multiple comparisons (Dunnett test); p values indicated. **f,** Summary graph of MHC-dependent spot mean data, as in (e), n=3 patients with glioblastoma. Paired data indicated. **g,** Killing assay. Left, phase contrast appearance at readout, after exposure to CD8⁺ T cells. Scale bar indicated. Right, Graph represents % of viable tumor cells relative to input. Technical replicates as individual dots. Mean values ± SEM; one of two independent experiments with

435 similar results (patient 21). One-way ANOVA corrected for multiple comparisons (Šídák test); p values indicated. **h,** Frequency of predicted tumor reactivity in individual CD8⁺ T cells by predicTCR. (n) patients per source: PBMC (2), dBM (3), CB (6), Tumor (6). **i,** Bar plots per source aligning top 50 CD8⁺ clonotypes by frequency. **j,** UMAP of CD8⁺ T cells with paired scVDJ information (n=14,960), categorized by T cell subtype. Inset displays tumor-reactivity by predicTCR. **k,** Frequency of predicted tumor reactivity among tumor-shared CD8⁺ clonotypes,

440 by source. **l,** Stacked bar plots visualizing CD8⁺ T cell phenotypes among tumor-reactive clonotypes shared between CB and tumor, split per source. **m,** Illustration of sites assessed for PET-CT/MRI-specific Pentixafor labeling. **n,** Presurgical CXCR4 PET-CT data, secondary MRI fused, showing examples with (red) and without (blue) radiotracer enhancement in the CB at initial diagnosis. Insets magnify selected CB areas. Arrowheads point to radiotracer enhancement. **o,** Kaplan-Meier survival plot of patients with glioblastoma. Censored data and p-

445 value indicated. Log-rank (Mantel-Cox) test.

References

1. Castellani, G., Croese, T., Peralta Ramos, J. M. & Schwartz, M. Transforming the understanding of brain immunity. *Science* **380**, eabo7649 (2023).

2. Rustenhoven, J. *et al.* Functional characterization of the dural sinuses as a neuroimmune interface. *Cell* **184**, 1000-1016 e1027 (2021).

3. Mollgard, K. *et al.* A mesothelium divides the subarachnoid space into functional compartments. *Science* **379**, 84-88 (2023).

4. Sankowski, R*., et al.* Multiomic spatial landscape of innate immune cells at human central nervous system borders. *Nat Med* **30**, 186-198 (2024).

5. Louveau, A. *et al.* Structural and functional features of central nervous system lymphatic vessels. *Nature* **523**, 337-341 (2015).

6. Smyth, L.C.D*., et al.* Identification of direct connections between the dura and the brain. *Nature* **627**, 165-173 (2024).

7. Mazzitelli, J.A., *et al.* Skull bone marrow channels as immune gateways to the central nervous system. *Nat Neurosci* **26**, 2052-2062 (2023).

8. Wen, P. Y. *et al.* Glioblastoma in adults: a Society for Neuro-Oncology (SNO) and European Society of Neuro-Oncology (EANO) consensus review on current management and future directions. *Neuro Oncol* **22**, 1073-1113 (2020).

9. Jackson, C. M., Choi, J. & Lim, M. Mechanisms of immunotherapy resistance: lessons from glioblastoma. *Nat Immunol* **20**, 1100-1109 (2019).

10. Sampson, J. H., Gunn, M. D., Fecci, P. E. & Ashley, D. M. Brain immunology and immunotherapy in brain tumours. *Nat Rev Cancer* **20**, 12-25 (2020).

11. Chongsathidkiet, P*., et al.* Sequestration of T cells in bone marrow in the setting of glioblastoma and other intracranial tumors. *Nat Med* **24**, 1459-1468 (2018).

12. Pinho, S. & Frenette, P. S. Haematopoietic stem cell activity and interactions with the niche. *Nat Rev Mol Cell Biol* **20**, 303-320 (2019).

13. Buck, A.K*., et al.* CXCR4-targeted theranostics in oncology. *Eur J Nucl Med Mol Imaging* **49**, 4133-4144 (2022).

14. Lapa, C. *et al.* (68)Ga-Pentixafor-PET/CT for Imaging of Chemokine Receptor 4 Expression in Glioblastoma. *Theranostics* **6**, 428-434 (2016).

15. Gruneboom, A. *et al.* A network of trans-cortical capillaries as mainstay for blood circulation in long bones. *Nat Metab* **1**, 236-250 (2019).

16. Friebel, E. *et al.* Single-Cell Mapping of Human Brain Cancer Reveals Tumor-Specific Instruction of Tissue-Invading Leukocytes. *Cell* **181**, 1626-1642 e1620 (2020).

17. Klemm, F. *et al.* Interrogation of the Microenvironmental Landscape in Brain Tumors Reveals Disease-Specific Alterations of Immune Cells. *Cell* **181**, 1643-1660 e1617 (2020).

18. Lu, I. N. *et al.* Tumor-associated hematopoietic stem and progenitor cells positively linked to glioblastoma progression. *Nat Commun* **12**, 3895 (2021).

19. Yeo, A. T. *et al.* Single-cell RNA sequencing reveals evolution of immune landscape during glioblastoma progression. *Nat Immunol* **23**, 971-984 (2022).

20. Pombo Antunes, A.R*., et al.* Single-cell profiling of myeloid cells in glioblastoma across species and disease stage reveals macrophage competition and specialization. *Nat Neurosci* **24**, 595-610 (2021).

21. Rashidi, A*., et al.* Myeloid cell-derived creatine in the hypoxic niche promotes glioblastoma growth. *Cell Metab* **36**, 62-77 e68 (2024).

22. Feuerer, M. *et al.* Bone marrow as a priming site for T-cell responses to blood-borne antigen. *Nat Med* **9**, 1151-1157 (2003).

23. Gebhardt, T., Park, S.L. & Parish, I.A. Stem-like exhausted and memory CD8(+) T cells in cancer. *Nat Rev Cancer* **23**, 780-798 (2023).

24. Aran, D. *et al.* Reference-based analysis of lung single-cell sequencing reveals a transitional profibrotic macrophage. *Nat Immunol* **20**, 163-172 (2019).

25. Setty, M. *et al.* Characterization of cell fate probabilities in single-cell data with Palantir. *Nat Biotechnol* **37**, 451-460 (2019).

26. Gulati, G. S. *et al.* Single-cell transcriptional diversity is a hallmark of developmental potential. *Science* **367**, 405-411 (2020).

27. Meistermann, D*., et al.* Integrated pseudotime analysis of human pre-implantation embryo single-cell transcriptomes reveals the dynamics of lineage specification. *Cell Stem Cell* **28**, 1625-1640 e1626 (2021).

28. Chu, Y*., et al.* Pan-cancer T cell atlas links a cellular stress response state to immunotherapy resistance. *Nat Med* **29**, 1550-1562 (2023).

29. Stress response in tumor-infiltrating T cells is linked to immunotherapy resistance. *Nat Med* **29**, 1336-1337 (2023).

30. Sautes-Fridman, C., Petitprez, F., Calderaro, J. & Fridman, W. H. Tertiary lymphoid structures in the era of cancer immunotherapy. *Nat Rev Cancer* **19**, 307-325 (2019).

31. Collins, N*., et al.* The Bone Marrow Protects and Optimizes Immunological Memory during Dietary Restriction. *Cell* **178**, 1088-1101 e1015 (2019).

32. Spiegel, S. & Milstien, S. The outs and the ins of sphingosine-1-phosphate in immunity. Nat Rev Immunol 11, 403-415 (2011).

33. Tan, C.L*., et al.* Prediction of tumor-reactive T cell receptors from scRNA-seq data for personalized T cell therapy. *Nat Biotechnol* (2024).

34. Upadhye, A*., et al.* Intra-tumoral T cells in pediatric brain tumors display clonal expansion and effector properties. *Nat Cancer* (2024).

35. Pages, F*., et al.* Effector memory T cells, early metastasis, and survival in colorectal cancer. *N Engl J Med* **353**, 2654-2666 (2005).

36. Fairfax, B.P*., et al.* Peripheral CD8(+) T cell characteristics associated with durable responses to immune checkpoint blockade in patients with metastatic melanoma. *Nat Med* **26**, 193-199 (2020).

37. Mazo, I. B. *et al.* Bone marrow is a major reservoir and site of recruitment for central memory CD8+ T cells. *Immunity* **22**, 259-270 (2005).

38. Song, E*., et al.* VEGF-C-driven lymphatic drainage enables immunosurveillance of brain tumours. *Nature* **577**, 689-694 (2020).

39. Blobner, J. *et al.* Comparative evaluation of T-cell receptors in experimental glioma-draining lymph nodes. *Neurooncol Adv* **3**, vdab147 (2021).

40. Noffsinger, B. *et al.* Technical choices significantly alter the adaptive immune response against immunocompetent murine gliomas in a model-dependent manner. *J Neurooncol* **154**, 145-157 (2021).

41. Zheng, L. *et al.* Pan-cancer single-cell landscape of tumor-infiltrating T cells. *Science* **374**, (2021).

42. Wischnewski, V. *et al.* Phenotypic diversity of T cells in human primary and metastatic brain tumors revealed by multiomic interrogation. *Nat Cancer* (2023).

43. Goebeler, M.E. & Bargou, R.C. T cell-engaging therapies - BiTEs and beyond. *Nat Rev Clin Oncol* **17**, 418-434 (2020).

44. Bagley, S.J*., et al.* Intrathecal bivalent CAR T cells targeting EGFR and IL13Ralpha2 in recurrent glioblastoma: phase 1 trial interim results. *Nat Med* (2024).

45. Brown, C.E*., et al.* Locoregional delivery of IL-13Ralpha2-targeting CAR-T cells in recurrent high-grade glioma: a phase 1 trial. *Nat Med* (2024).

46. Choi, B.D*., et al.* Intraventricular CARv3-TEAM-E T Cells in Recurrent Glioblastoma. *N Engl J Med* **390**, 1290-1298 (2024).

47. Xiong, Z*., et al.* Glioblastoma vaccines: past, present, and opportunities. *EBioMedicine* **100**, 104963 (2024).

48. Cloughesy, T. F. *et al.* Neoadjuvant anti-PD-1 immunotherapy promotes a survival benefit with intratumoral and systemic immune responses in recurrent glioblastoma. *Nat Med* **25**, 477-486 (2019).

49. Schalper, K. A. *et al.* Neoadjuvant nivolumab modifies the tumor immune microenvironment in resectable glioblastoma. *Nat Med* **25**, 470-476 (2019).

50. Stensjoen, A. L. *et al.* Growth dynamics of untreated glioblastomas in vivo. *Neuro Oncol* **17**, 1402-1411 (2015).

Methods

<u>Ethics statement:</u>

Written informed consent was obtained from all participants of this study; all procedures were performed in accordance with the Declaration of Helsinki and approved by the local ethics committees (University Hospital Essen #19-8706-BO, #22-10564-BO; University Hospital Würzburg approval #20230824 01).

<u>Human biosampling</u>

Clinical specimens were collected from patients with glioblastoma, i.e. newly diagnosed, chemo-/radiotherapy-naive, *IDH*-wildtype glioblastoma CNS WHO grade 4[51] at the Department of Neurosurgery and Spine Surgery of the University Hospital Essen. As control, tissue was collected from patients with non-malignant intracranial disease (Supplementary Table 1,2). At surgery, no patient suffered from acute infection or chronic inflammation. Calvarial bone chips derived during craniotomy from unplanned, intra-surgically required extensions of the burr hole or during necessary additional temporo-basal decompression after craniotomy. Tumor tissue was obtained from contrast-enhanced, 5-aminolevulinic acid fluorescent, non-necrotic tumor areas by neuronavigation (Brainlab). Samples of tumor and paired bone were immediately stored in sterile Dulbecco's Modified Eagle Medium (DMEM)/F12 (Gibco, #11320033), supplemented with antibiotics/antimycotics (2%, Gibco, #15240062). Standard collection of venous blood occurred at surgery or within 24 h. Standard dBM aspiration from posterior iliac crest was performed under general anesthesia prior to neurosurgery. Samples were immediately processed in the lab and registered at the Westdeutsche Biobank Essen (WBE, #22-WBE-137). Postsurgical CT scans were obtained within 24 h, additional MRI scans of patients with glioblastoma within 72 h.

<u>Clinical CXCR4 radiolabeling</u>

PET-CT imaging data (University Hospital Wuerzburg)[14] complemented data derived from presurgical [^{68}Ga]Ga-CXCR4 (Pentixafor) radiolabeling of patients with glioblastoma as part of clinical care at the University Hospital Essen (Supplementary Table 1). Intravenous (i.v.) administration of Pentixafor in Würzburg / Essen used activities of $1.94 \pm 0.41 / 2.38 \pm 0.39$ MBq/kg followed by imaging $72 \pm 14 / 65 \pm 19$ minutes thereafter (mean $\pm$ SD). Integrated data (n=19 histologically confirmed glioblastoma) underwent blinded consensus read by board-certified nuclear radiologists from both centers, using equal range settings. Cranial/calvarial enhancement was defined as focal uptake in the tumor-adjacent CB and absence of uptake in the contralateral reference point. Bridging tracer enhancement was classified as clearly distinguishable tracer transition between tumor and CB exceeding brain background uptake. Tracer uptake in the skin or in the venous sinuses was not assessed. As a control, patients not suffering from brain tumors (n=6, Supplementary Table 2) received i.v. Pentixafor during clinical workup in Essen with an activity of 2.13 ± 0.25 MBq/kg. Imaging was performed 81 ± 10 minutes thereafter on a Siemens Vision PET-CT scanner and CT/MRI fusion conducted by board-certified nuclear medicine personnel using Syngo.Via (Siemens Healthineers) or Brainlab's cranial navigation software (iPlanNet).

<u>Tumor tissue processing</u>

Within 30 min after resection, samples were minced and processed for derivation of primary cell cultures[52]. In parallel, single cell suspensions were prepared[18] by homogenizing tissue in Iscove's Modified Dulbecco's Medium (IMDM, Gibco, #12440053) with 0.11 DMC U/mL neutral protease (NP, Nordmark Biochemicals, #S3030112) at 37°C for ~30 minutes in a shaker-incubator supported by intermittent resuspension. Cell suspension was filtered (35 μm cell strainer, Falcon, #352235) and washed twice with PBS (pH 7.4,

Gibco, #14190169), supplemented with 0.04% bovine serum albumin (BSA, Miltenyi Biotec, #130-091-376).

Bone sample processing

Bone chips were flushed with 0.11 DMC U/mL NP in IMDM for 10–15 minutes (37°C) followed by PBS/0.04% BSA. Filtered cell suspensions (35 μm cell strainer) were centrifuged (10 minutes, 300xg) and washed once in PBS/0.04% BSA. If available, excess bone tissue was flash-frozen in liquid nitrogen and stored at -80°C.

Blood sample and dBM processing

Blood and dBM arrived at RT in EDTA or heparin containing tubes for isolation of peripheral blood mononuclear cells (PBMC) or bone marrow mononuclear cells (BMMC) by Histopaque®-1077 (Sigma-Aldrich, #10771) density gradient centrifugation (manufacturer's protocol). Cells were washed twice in PBS/0.04% BSA.

Selection and preservation of immune cells

Single cell suspensions from tumor tissue, bone, and blood were enriched for vital CD45$^+$ cells by the REAlease® CD45 (TIL) MicroBead Kit (manufacturer's protocol, Miltenyi Biotec, #130-121-563). Anti-CD45 antibodies were removed and cells either used immediately or cryopreserved at -150°C in 50% resuspension media (40% FBS in IMDM) and 50% freezing media (30% DMSO + 40% FBS in IMDM), according to #CG00039 (10x Genomics). Derived samples were labeled sc-cohort 1 (Extended Data Fig. 3). Cells of sc-cohort 2 (Extended Data Fig. 9) underwent additional magnetic myeloid cell depletion by collecting the CD14$^-$ negative flow-through (#130-050-201).

scRNA sequencing and analysis

Cell suspensions with >85% viable cells (trypan blue exclusion) were processed for scRNA-seq using Chromium Next GEM Single Cell 3' Reagent Kit v3.1 and 5' Reagent Kit v2 (10x Genomics, #CG0000315 and #CG0000331). Subsequent to quality control (2100 Bioanalyzer, Agilent), paired-end sequencing of pooled libraries was conducted on a NovaSeq 6000 system (Illumina). Reads were aligned to the hg38 human reference genome (2020) using Cell Ranger (v.7.0.1). 5' data, integrating V(D)J repertoire and gene expression, were processed with cellranger multi pipeline using 10x Genomics hg38 and V(D)J reference (7.0.0, GRCh38).

Analyses were performed in R (v4.2.0) on raw 3' and filtered 5' multi output data. Using Seurat package (v.4.3.0)[53], normalized cells (SCTransform) were filtered to remove cells with <500 or >7500 nFeature_RNA counts, or >15% mitochondrial genes and to identify doublets (DoubletFinder, v.2.0.3)[54]. 3' GEX (n=21) and 5' GEX/scVDJ (n=8) Seurat objects (sc-cohort 1, Extended Data Fig. 3) were merged, cleaned of doublets and normalized regressing out mitochondrial percentage/cell and cell cycle scores. Data integration used Harmony (v.0.1.1)[55] by patient, followed by Seurat FindNeighbors (dims = 1:15) and FindClusters function (resolution = 0.6) with data visualization via RunUMAP (dims = 1:15) (Fig. 2b,c). Cell type annotation of integrated data was performed using SingleR (v.1.10.0)[24] and marker-based identification via Seurat's FindAllMarkers function and subsequent literature search. Expression of canonical marker gene sets was confirmed and visualized by gene set enrichment scores (AUCell score, v.1.18.1)[56] (Extended Data Fig. 3c).

Myeloid cell compartment

Myeloid cell subset was refined by removing falsely-clustered T cells (*CD3D* < 0.1), followed by normalization and data integration. Cell type annotation utilized Azimuth tool[53] (v1.0.2) with GBMap dataset[57]. Only myeloid cells at annotation level 3 were kept, excluding

cells expressing *CD3*, *GFAP*, *OLIG1/2*, or *RBFOX3*. The refined dataset was integrated by Harmony, followed by dimensional reduction using PHATE[58] (v1.0.7) and cell type
655   identification via shared-nearest neighbor clustering.

Tumor-shared clonotypes in the CB
        For integrating scVDJ information, TCRA/TCRB nucleotide sequences were assigned to T cells using Cell Ranger's filtered contig annotation data (patient 4, 15, 16; sc-cohort 1)
660   and combineExpression function of scRepertoire (v.1.11.0)[59]. Differentially expressed genes (DEGs) were detected from tumor-shared clones ($\geq$ 2 cells) versus non-expanding singlets in the CB niche using Seurat's FindMarkers() function with min.pct=0.2 (20% of cells). Top ten DEGs (ranked by Log2FC) were visualized using Seurat's VlnPlot.

665   CD8+ T cell compartment (sc-cohort 1)
        T cells were subset removing falsely-clustered myeloid cells (*CD68* < 0.01), normalized and data integration reperformed. Using Seurat's FindNeighbors (dims = 1:15), FindClusters (resolution = 0.5) and RunUMAP (dims = 1:15) functions, CD8+/CD4+ T cells, CD4+ Tregs, and MAIT cells were distinguished by cluster-based marker gene expression
670   (Extended Data Fig. 3d,e). Cells lacking T cell genes ("unknown") or displaying high mitochondrial gene expression ("low quality") were excluded from analyses. *CD8+* and *CD4+* clusters were subsetted and remaining *CD4* or *CD8* expressing cells removed (*CD4* <0.01/ *CD8A* & *CD8B* <0.01). 6,550 cells remained unassigned. Their identity was determined by cluster-independent *CD4* or *CD8A*/*CD8B* expression. Identified (*CD4* <1e-15 & *CD8A*/*CD8B*
675   >1e-15) CD8+ cells (n=4,876) were added to the CD8+ T cell subspace for further analyses. Cells were normalized and integrated, followed by Seurat's FindNeighbors (dims = 1:10), FindClusters (resolution = 0.5) and RunUMAP (dims = 1:15) command for data visualization. Highly variable genes of the eleven distinct clusters were extracted via FindAllMarkers, and cellular identities were manually annotated (Extended Data Fig. 3f). Remaining MAIT cells,
680   not belonging to CD8+ T cell subset, were re-assigned to the global T cell space (Extended Data Fig. 3d-f). Normalization and data integration revealed the final CD8+ T cell space (n=18,973).

CB subspace assessment
685   3' GEX CD8+ T cell subset of CB (n=6,743 cells) was normalized (NormalizeData) using Seurat (v4.1.1), followed by FindVariableFeatures, ScaleData (default parameters), and RunPCA functions (npcs=100). Following data integration by patient (Harmony), cells were ordered by differentiation trajectory using Python package Palantir[25] (v1.0.1), visualized by RunUMAP (dims=1:4). A numeric vector, predicting cellular status from least (1.0) to most
690   (0.0) differentiated was generated from the RNA matrix by CytoTRACE[26] (v.0.3.3). Pseudotime analysis was conducted using Monocle 3[60] (v.1.3.1.) Following conversion into a CDS object using as.cell_data_set from SeuratWrappers, the cluster_cell and learn_graph functions from Monocle were applied. Location of naive CD8+ T cells was used to specify root node (order_cells function). Combined 3' GEX CD8+ T data were used to compute
695   cellular CytoTRACE scores of tumor and CB, visualized with ggplot2 (v.3.4.3) (Extended Data Fig. 7a). VlnPlot2 (SeuratExtend v.0.6.0)[61] was used to plot and compare (Wilcoxon test) CytoTRACE scores of CB-enriched CD8+ T cells from both sources (Extended Data Fig. 7b).

700   Benchmarking to external signatures
        Gene set enrichment scores of 19 curated CD8+ T cell gene signatures[28] were computed by AUCell. Z-Scores across phenotypes and sources were calculated via CalcStats (SeuratExtend) and visualized as heatmap (Fig. 3h). Effector phenotypes were isolated and

69

their Activation:Effector function Signature[28] AUCell Score visualized (VlnPlot2, Seurat Extend).

Sub-analysis of sc-cohort 2

Preprocessing of scData included removal of cells with <500 or >7500 nFeature_RNA counts, >15% mitochondrial genes, and doublets before data integration. Normalization (SCTransform), including regression of mitochondrial read and cell cycle scores, and Harmony by patient was executed prior to FindNeighbors (dims = 1:15), FindClusters (resolution = 0.4), and RunUMAP (dims = 1:15) functions for data visualization (Extended Data Fig. 9b). SingleR and AUCell Score of canonical T cell genes were employed to identify $CD8^+/CD4^+$ T cells, $CD4^+$ Tregs and MAIT cells (Extended Data Fig. 9c). Assignment of scVDJ information used Cell Ranger's filtered contig annotation data and combineExpression function (scRepertoire). $CD8^+$ T cells of sc-cohort 2 were subset and annotated by label-transfer of sc-cohort 1 using singleCellNet[62] (v.0.1.0) (Extended Data Fig. 9d,e).

Tumor reactivity prediction

Gene count matrix was imported into R v4.1 and normalized using SCTransform on all genes (Seurat v.4). Normalized data was imported in Python with reactivity predicted by predicTCR[33] model under xgboost (v1.7.4). Probability of reactivity was averaged for each clonotype, and threshold was determined using Fisher-Jenk natural break optimization. Clones with reactivity scores above threshold were designated as reactive and vice versa. For visualization, scVDJ data from sc-cohort 1 (patient 4, 15, 16) and sc-cohort 2 (patient 21, 22, 24) were integrated (n=14,960). FindNeighbors (dims = 1:10), FindClusters (resolution = 0.5) and RunUMAP (dims = 1:10) functions were executed and data visualized as UMAP.

T cell expansion

T cells were expanded from $CD45^+$-enriched cells in T cell activation media (RPMI 1640 (Gibco, #72400021), human AB serum (10%, Sigma-Aldrich, #H5667), sodium pyruvate (1 mM, Gibco, #11360039), β-mercaptoethanol (50 µM, Gibco, #21985023), antibiotic-antimycotic (1%), recombinant IL-2 (1000 U/mL, #200-02), IL-15 (10 ng/mL, #200-15) and IL-21 (10 ng/mL, #200-21, all Peprotech)), similarly to[63]. T cells expanded for 14–21 days in 96-well plates (Corning, #3596) with human T-activator CD3/CD28/CD137 Dynabeads (Gibco, #11163D) in a 1:5-10 bead:cell ratio. Prior to analyses, $CD8^+$ T cells were enriched by magnetic separation (Miltenyi Biotec, #130-096-495), immediately used or stored at -150°C.

ELISpot assays

Cellular Interferon-γ release (R&D Systems, #EL285, #SEL285) was detected by incubating 10,000–20,000 bulk $CD8^+$ T cells and 5,000–10,000 autologous tumor cells in 96-well plates (2:1 effector:target ratio). Autologous, short-term expanded tumor cells (passage 4–7) were pre-stimulated with IFNγ (1 µg/mL, Peprotech #300-02) for 48 h. T cells rested in reduced cytokine concentrations (20 U/mL IL-2, 1 ng/mL IL-15, 1 ng/mL IL-21) for at least 3 days and overnight in cytokine-free media. ELISpot assays were performed according to manufacturer's instructions after 24-48h co-incubation. MHCI/II blockade was achieved by pre-incubating tumor cells with 5 µg/mL anti HLA-DR (clone L243) and 5 µg/mL anti HLA-A,B,C (clone W6/32) antibodies (Biolegend, #307648 and #311428) for 1h. Background controls included wells with only $CD8^+$ T cells or tumor cells. Spots were counted using ELISpot reader (AID iSpot, AID Autoimmun Diagnostika) and analyzed with Fiji Software (v1.0). MHC-dependent spots defined as:

$$\#spots_{(CD8+ \text{ T cells+autologous tumor cells})} - \#spots_{(CD8+ \text{ T cells+autologous tumor cells+MHC block})}$$

755

Restimulation experiments

T cell activation was monitored by T cell clustering/aggregation during restimulation[64]. Expanded T cells rested in reduced cytokine conditions (see above) for at least 72h. Restimulation cycles involved seeding 10,000 T cells in 96-well plates in activation
760 media and CD3/CD28/CD137 Dynabeads (1:2 bead:cell ratio). Resilience assay evaluated CD8$^+$ T cell fitness by counting successful restimulation cycles. Three 14-day-restimulation cycles, followed by 7 days of rest were performed in triplicates per patient and source. A restimulation cycle was successful if the mean cell count across all three wells exceeded the input of 10,000 cells/well. Resting T cells were cryopreserved in 80% FBS and 20% DMSO
765 after expansion and re-stimulation.

Killing assay

Adapting protocols[65,66], we enriched tumor-reactive T cells by incubating 20,000 resting CD8$^+$ T cells with 5,000 IFNγ stimulated autologous tumor cells on anti-CD28-coated
770 96-well plates (4 µg/ml, Biolegend #302934). Media consisted of ¼ maintenance media for primary tumor cells[52] + ¾ T cell activation media. Co-cultures were fed every other day and T cell outgrowth incubated on fresh tumor cells weekly (up to 4 weeks). Derived T cells were used for the killing assay. Briefly, for patient 21, 20,000 tumor-reactive T cells were incubated at week 4 with 5,000 autologous tumor cells labeled with 1 µM CellTracker™ Red
775 (Invitrogen #C34552) supplemented with caspase 3 substrate (NucView® Biotium #10402), according to manufacturer's protocol. After 7 days, T cells were gently removed and live adherent tumor cells were detected (Nyone, Synentec) using 1 µg/ml Hoechst 33342 (Thermo Fisher #62249). Celltracker signals and cellular morphology discriminated tumor cells and T cells, excluding Caspase-positive cells. MHCI blockade was achieved by pre-incubating
780 tumor cells with 10 µg/mL anti HLA-A,B,C (W6/32) antibodies for 1h. During the assay, cells were fed once with fresh media and blocking antibodies at day 4.

Flow cytometry

Spectral flow cytometry-based immunoprofiles was detected using Cytek® 25-Color
785 Immunoprofiling Assay (Cytek Biosciences, #R7-40002), with 18 cFluor reagents supplemented with 7 antibodies from BioLegend (#900004160) and ViaDye Red Fixable Viability Dye (Cytek), according to manufacturer's protocol. Cryo-conserved single cells were thawed and washed twice prior to antibody-labeling. Viability dye was used at 250 nM prior to blocking (Human TruStain FcX, BioLegend) and subsequent antibody-labeling.
790 Samples were measured on a Cytek Aurora flow cytometer in 5L setup (16UV-16V-14B-10YG-8R), acquiring spectral profiles by SpectroFlo software (v3.0.3; Cytek). Unmixing was performed using the manufacturer's recommended reference controls, autofluorescence extraction enabled. Cell populations were quantified by recommended enhanced gating strategy (Cytek). Alternative gating to identify potential M-MDSCs was carried out via
795 FlowJo (v10.9.0).

For phenotyping, indicated CD8$^+$ cells from resilience assay were thawed, washed, and incubated for 5 min with Fc-gamma receptor binding inhibitor (#564220, BD Pharmingen) prior to antibody-labeling. The antibody cocktail consisted of BV421-CD95 (#305623), BV711-CD8 (#344733), BV510-CCR7 (#353231), APC-CD4 (#317415), FITC-
800 CD161 (#339905), PE-Cy7-CD3 (#344815), BV650-PD-1 (#329949, all Biolegend) as well as BV786-CD45RA (#563870) and PE-CD56 (#555516) from BD Biosciences (all diluted at 1:20). Viability verified using 7AAD (#00-6993-50, Invitrogen). Cytometric profiling of S1PR1 on T cells was performed accordingly, by Fc-block and antibody panel (all diluted at 1:20): BV421-CD95 (#305623), BV711-CD8 (#344733), BV510-CCR7 (#353231), PE-CD4
805 (#317410), PE-Cy7-CD3 (#344815), BV650-PD-1 (#329949, all Biolegend) as well as

BV786-CD45RA (#563870, BD Biosciences) and eFluor660-S1PR1 (#50-3639-42) or respective Isotype Control (#50-4714-82) (Thermo Fisher Scientific). Samples were incubated on ice in the dark for 30 minutes, washed and measured using FACS Celesta and FACS Diva software (v8.0.1.1, BD Biosciences), with FlowJo sub-analysis (v10.9.0.) Gating strategies depicted in the corresponding Extended Data Figures.

Whole mount staining and optical clearing

CB samples were fixed in 4% PFA (in PBS, pH = 7.4) overnight at 4–8°C and blocked (5% DMSO, 0.1% Tween20, 1% BSA, and 5 mM EDTA in PBS) for two days at RT. Immunofluorescence (IF) labeling was performed with PE/Dazzle594-CD45 (#304052) and AlexaFluor647-CD34 (#343508) Biolegend antibodies diluted 1:200 in blocking buffer for five days at RT. Samples were washed twice with 5% DMSO and 0.1% Tween20 in PBS for one day at RT, respectively. Optical tissue clearing was performed by established methods[15]. Briefly, dehydration in increasing ethanol concentrations of 50%, 70% and 100% (RT, one day each) was followed by optical clearing in ethyl cinnamate (ECi, Sigma Aldrich, #112372) at RT to achieve complete transparency.

Light-Sheet Fluorescence Microscopy (LSFM)

ECi-cleared CB were imaged via LSFM, using a LaVision BioTec Ultramicroscope Blaze (Miltenyi/LaVision BioTec) with supercontinuum white light laser (460-800nm), 7 excitation and emission filters covering 450nm to 865nm, AndorNeo sCMOS Camera with pixel size of $6.5x6.5\mu m^2$, and 1.1x (NA 0.1), 4x (NA 0.35), 12x (NA 0.53) objectives with magnification changer ranging from 0.66x to 30x. Cleared samples were immersed in ECi in a quartz cuvette and imaged using excitation (ex) and detection band-pass emission (em) filter settings: tissue autofluorescence, ex 500/20nm, em 535/30nm; CD45-PE-Dazzle594, ex 560/40nm, em 650/50nm; CD34-AlexaFluor647, ex 630/60nm, em 680/30nm. The Z-step size was set to 5 or 10 μm based on the selected light-sheet NA. Depending on the objectives, optical zoom factor varied from 4x to 12x, with a digital zoom factor of 1x. Data were processed with visualization tools from Imaris (Bitplane, v9.7.1).

Confocal laser scanning microscopy (CLSM) to assess TLS formation

CB samples were decalcified in 14% EDTA-free acid solution (pH = 7.2) for 14 days at RT, washed with PBS, embedded in O.C.T. Compound (Sakura, #4583) and snap frozen. Twenty μm tissue sections were generated on a CryoStar NX70 (Thermo Fisher) using Kawamoto's film method (Section Lab, Cryofilm type 2C9) and stored at -20°C. For IF labeling, tissue sections were blocked (1% BSA, 0.1% Tween20, and 0.1% DMSO in PBS) for 1h at RT and incubated with PE/Dazzle594 CD3 (1:100, Biolegend, #300450), AlexaFluor488 CD20 (1:100, Thermo Fisher, #53-0202-80) and DAPI (1:500, Carl Roth, #6335.1) in blocking buffer overnight (4-8°C). Samples were washed 3x with washing buffer for 15min at RT and 1x with distilled water, covered with mounting medium (Agilent Dako, #S3023) and imaged via high-resolution CLSM on a Leica TCS SP8 confocal laser scanning microscope equipped with acousto-optic tunable filters, an acousto-optical beam splitter, internal hybrid detectors (HyD SP) with use of an LMT200 high precision scanning stage. A Leica HC PL APO 63x/1.20 W CORR objective combined with a digital zoom factor of 1.0 was used for imaging of sequential scans: (1) CD20-AlexaFluor488, ex 488nm (argon laser), em 500-550nm, (2) CD3-PE/Dazzle594, ex 561nm, em 600-650nm and (3) Dapi, ex 405nm, em 450-500nm, with the last two being excited by a diode-pumped solid-state laser. 3D reconstruction used Imaris software (v9.7.1, Bitplane) at maximum intensity projection.

<u>Quantitative multiplex immunofluorescence imaging</u>

CB samples were fixed with 4% methanol-free formaldehyde (Thermo Fisher) overnight with rotation at 4 °C. Decalcification (10% EDTA, pH 8, Sigma) for 14 days at RT with stirring, followed by dehydration (overnight) and paraffin embedding. Ten μm tissue sections were cut (pfm slide 4004M sledge microtome), deparaffinized, re-hydrated and antigen-retrieved according to manufacturer's instructions (Agilent Technologies). Sections were blocked and permeabilized with TBS (0.1M Tris, 0.15 M NaCl, pH 7.5) containing 0.05% Tween-20, 20% DMSO (Sigma) and 10% donkey serum (Jackson ImmunoResearch) for 15 minutes at RT. Antibodies (1:25) and DAPI were diluted in DAKO EnVision FLEX diluent (Agilent Technologies). Primary antibodies (CD45, Bio-Rad/#MCA345G; CD146 R&D/#AF932; CXCR4, Thermo Fisher/#PA3-305) were applied overnight. Secondary antibodies (Donkey anti-rabbit 488, anti-goat 555, anti-rat 594, (all Biotium)) were incubated for 5h and DAPI (Thermo Fisher) was applied prior to mounting (Vector Laboratories, #H-1400-10). Labeled sections were imaged on a Leica Stellaris 8 laser scanning confocal microscope equipped with 2x HyD-S, 2x HyD-X and one HyD-R detectors and 2 laser lines (405 and white-light laser) using 20x multiple-immersion objective (NA 0.75, FWD 0.680 mm) at 400Hz, 8-bit with 1024x1024 resolution.

Statistics and reproducibility

Statistical methods, sample size and replication for each experiment are indicated in the Figure legends. Flow cytometry and ELISpot statistical analyses were performed using Prism software (v 9.5.1 GraphPad) or Microsoft Excel v16.79.2. Statistical analysis of survival data was executed in SPSS (v.29.0.2.0). For collection of tissue samples and clinical imaging data, no statistical method was used to predetermine sample size, but our sample sizes are similar to those reported in previous publications[67-69]. Tissue samples were collected consecutively. The sex of a patient was self-reported. No gender information was collected and sex was not considered in the study design. scRNAseq data with low quality (see above) and patients not meeting inclusion criteria for survival analysis (Extended Data Figure 10a) were excluded from the study. Experiments were not randomized. With the exception of PET data association with patient survival (Fig. 4m-o and Extended Data Fig. 10), data collection and analysis were not performed blind to the conditions of the experiments. In parametric statistical tests, data distribution was assumed to be normal but this was not formally tested.

Data availability

scRNA-seq data were deposited into NCBI Gene Expression Omnibus (GEO) and are available under accession # GSE233304. The hg38 human reference genome and the human V(D)J reference (GRCh38) are available under https://www.10xgenomics.com/support/software/cell-ranger/latest/release-notes/cr-reference-release-notes#cr7-0. All other data and materials are available in the manuscript and supplementary data.

Code availability

There was no custom computational code or software developed for this study. Analyses were performed with publicly available software packages as described in the Methods section.

Methods-only references

51. WHO Classification of Tumors Editorial Board (2021) Central nervous system tumours. Lyon (France): International Agency for Research on Cancer; 2021. (WHO classification of tumours series, 5th ed.; vol. 6)

910

52. Glas, M. *et al.* Residual tumor cells are unique cellular targets in glioblastoma. *Ann Neurol* **68**, 264-269 (2010).

53. Hao, Y. *et al.* Integrated analysis of multimodal single-cell data. *Cell* **184**, 3573-3587 e3529 (2021).

915

54. McGinnis, C. S., Murrow, L. M. & Gartner, Z. J. DoubletFinder: Doublet Detection in Single-Cell RNA Sequencing Data Using Artificial Nearest Neighbors. *Cell Syst* **8**, 329-337 e324 (2019).

55. Korsunsky, I. *et al.* Fast, sensitive and accurate integration of single-cell data with Harmony. *Nat Methods* **16** (2019).

920

56. Aibar, S*., et al.* SCENIC: single-cell regulatory network inference and clustering. *Nat Methods* **14**, 1083-1086 (2017).

57. Ruiz-Moreno, C. *et al.* Harmonized single-cell landscape, intercellular crosstalk and tumor architecture of glioblastoma. bioRxiv 2022.08.27.505439 (2022)

58. Moon, K.R*., et al.* Visualizing structure and transitions in high-dimensional biological data. *Nat Biotechnol* **37**, 1482-1492 (2019).

925

59. Borcherding, N., Bormann, N.L. & Kraus, G. scRepertoire: An R-based toolkit for single-cell immune receptor analysis. *F1000Res* **9**, 47 (2020).

60. Trapnell, C., et al. The dynamics and regulators of cell fate decisions are revealed by pseudotemporal ordering of single cells. Nat Biotechnol 32, 381-386 (2014).

930

61. Hua, Y. *et al.* Cancer immunotherapies transition endothelial cells into HEVs that generate TCF1(+) T lymphocyte niches through a feed-forward loop. *Cancer Cell* **40**, 1600-1618 e1610 (2022).

62. Tan, Y. & Cahan, P. SingleCellNet: A Computational Tool to Classify Single Cell RNA-Seq Data Across Platforms and Across Species. *Cell Syst* **9**, 207-213 e202 (2019).

935

63. Liu, Z. *et al.* Tumor-infiltrating lymphocytes (TILs) from patients with glioma. *Oncoimmunology* **6**, e1252894 (2017).

64. Yanguas, A. *et al.* ICAM-1-LFA-1 Dependent CD8+ T-Lymphocyte Aggregation in Tumor Tissue Prevents Recirculation to Draining Lymph Nodes. *Front Immunol* **9**, 2084 (2018).

65. Dijkstra, K.K*., et al.* Generation of Tumor-Reactive T Cells by Co-culture of Peripheral Blood Lymphocytes and Tumor Organoids. *Cell* **174**, 1586-1598 e1512 (2018).

940

66. Cattaneo, C.M*., et al.* Tumor organoid-T-cell coculture systems. *Nat Protoc* **15**, 15-39 (2020).

67. Vitanza, N.A*., et al.* Locoregional infusion of HER2-specific CAR T cells in children and young adults with recurrent or refractory CNS tumors: an interim analysis. *Nat Med* **27**, 1544-1552 (2021).

945

68. Todo, T*., et al.* Intratumoral oncolytic herpes virus G47Δ for residual or recurrent glioblastoma: a phase 2 trial. *Nat Med* **28**, 1630-1639 (2022).

69. Nassiri, F*., et al.* Oncolytic DNX-2401 virotherapy plus pembrolizumab in recurrent glioblastoma: a phase 1/2 trial. *Nat Med* **29**, 1370-1378 (2023).

Extended Data Figures
Dobersalske et al., Cranioencephalic functional lymphoid units in glioblastoma.
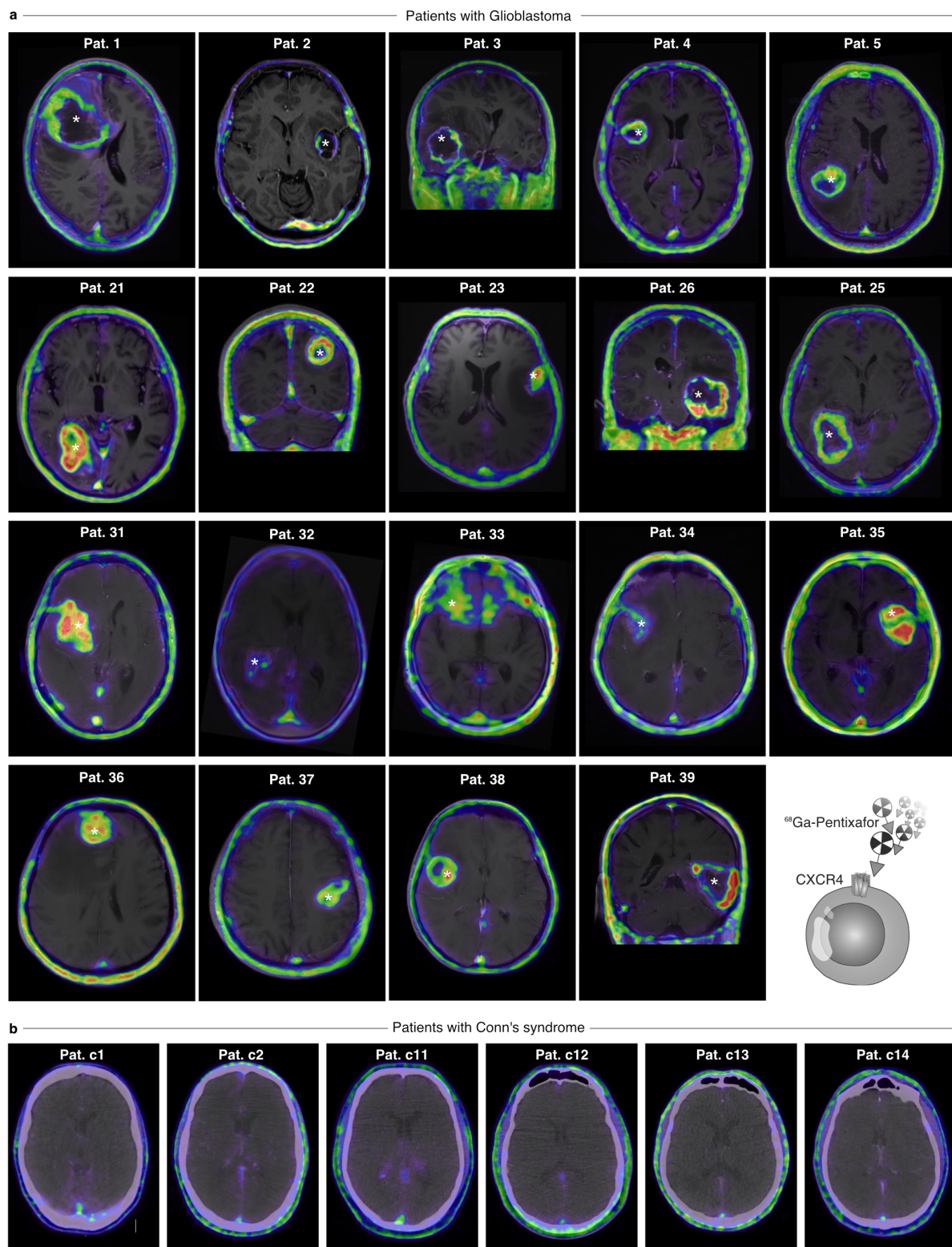
Extended Data Fig. 1: Clinical [⁶⁸Ga]Ga-Pentixafor radiolabeling. a, Representative imaging results of 19 patients with newly-diagnosed glioblastoma prior to neurosurgical tumor removal (patient 1 and 2 also included in Fig. 1). Clinical radiolabeling of CXCR4 and CT/MRI fusion allows identification of glioblastoma (asterisks) and surrounding encephalic and cranial structures. **b,** Representative Pentixafor PET-CT imaging data obtained from six patients diagnosed with Conn's syndrome, as a control, not suffering from intracranial neoplasia. Note the absence of tracer accumulation within the cranial bone.
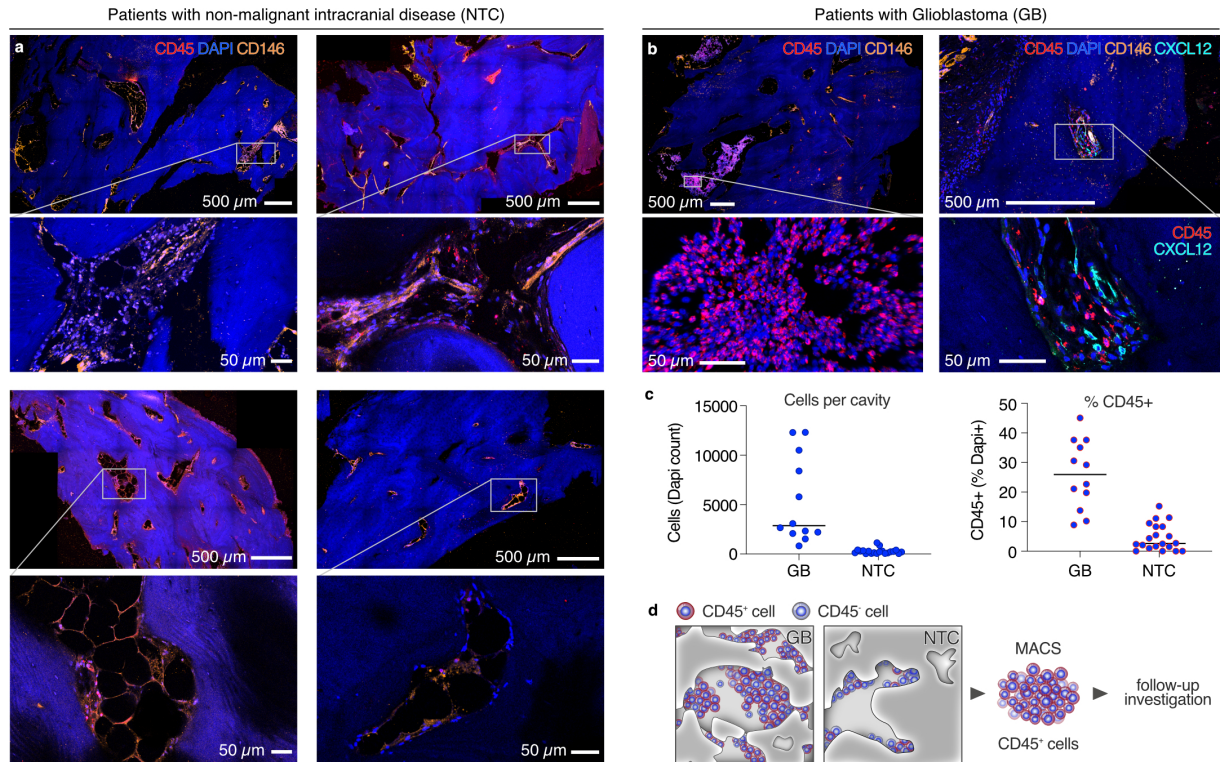
Extended Data Fig. 2: Immune cell accumulation in the cranial bone of patients with glioblastoma. a, Confocal immunofluorescence imaging of large CB tissue sections from four additional patients with non-malignant intracranial disease (NTC, non-tumor control; patients c15, c3, c16, c17), complementing presentation in Fig. 1f,g. Scale bars indicated. **b,** CB histological appearance of samples from two additional patients with glioblastoma (patients 29, 30), complementing presentation in Fig. 1h-k. Magnifications in the insets, scale bars indicated. **c,** Graphs present estimated immune cell frequencies in CB large tissue sections, quantified by labeling with DAPI and CD45 (data from n =2 glioblastoma (GB), and n = 4 NTC counting cells in 12 vs. 20 cavities, respectively). **d,** Schematic illustrating derivation of vital cells from the CB cavities for follow-up investigation.
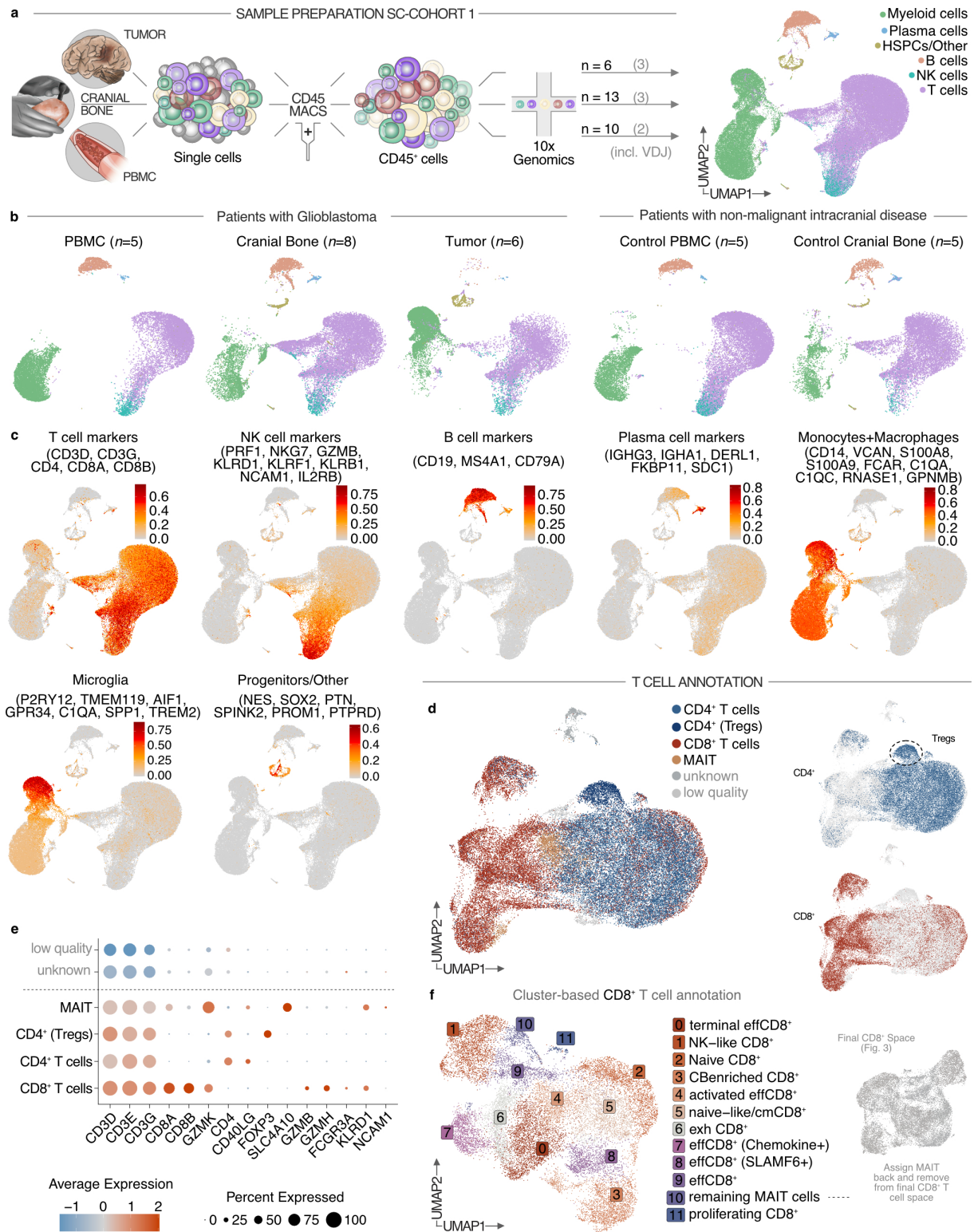
Extended Data Fig. 3: Immune cell derivation and cell type identification. a, Illustration of the workflow for sample processing and analysis of cells from sc-cohort 1 (see Methods). Samples from CB (n = 13), Tumor tissue (n = 6), and PBMC (n = 10) enriched by CD45^{+} magnetic cell isolation. Single cells were further analyzed by scRNA-seq (10X Genomics) and integrated data were used for subsequent analyses. **b,** Split UMAP plots visualizing the distribution of annotated single cells by source. **c,** UMAP visualization of listed canonical marker genes of annotated cell types. Cells are colored by the respective gene set enrichment scores calculated via AUCell. **d,** Global UMAP of T cell types. Note, cells annotated as unknown or low quality were excluded from subsequent analyses. **e,** Bubble plot depicts the average expression levels and the fractions of cells expressing selected marker genes across the T cell types annotated in (d). **f,** Cluster-based annotation of CD8^{+} T cell subspace.

77
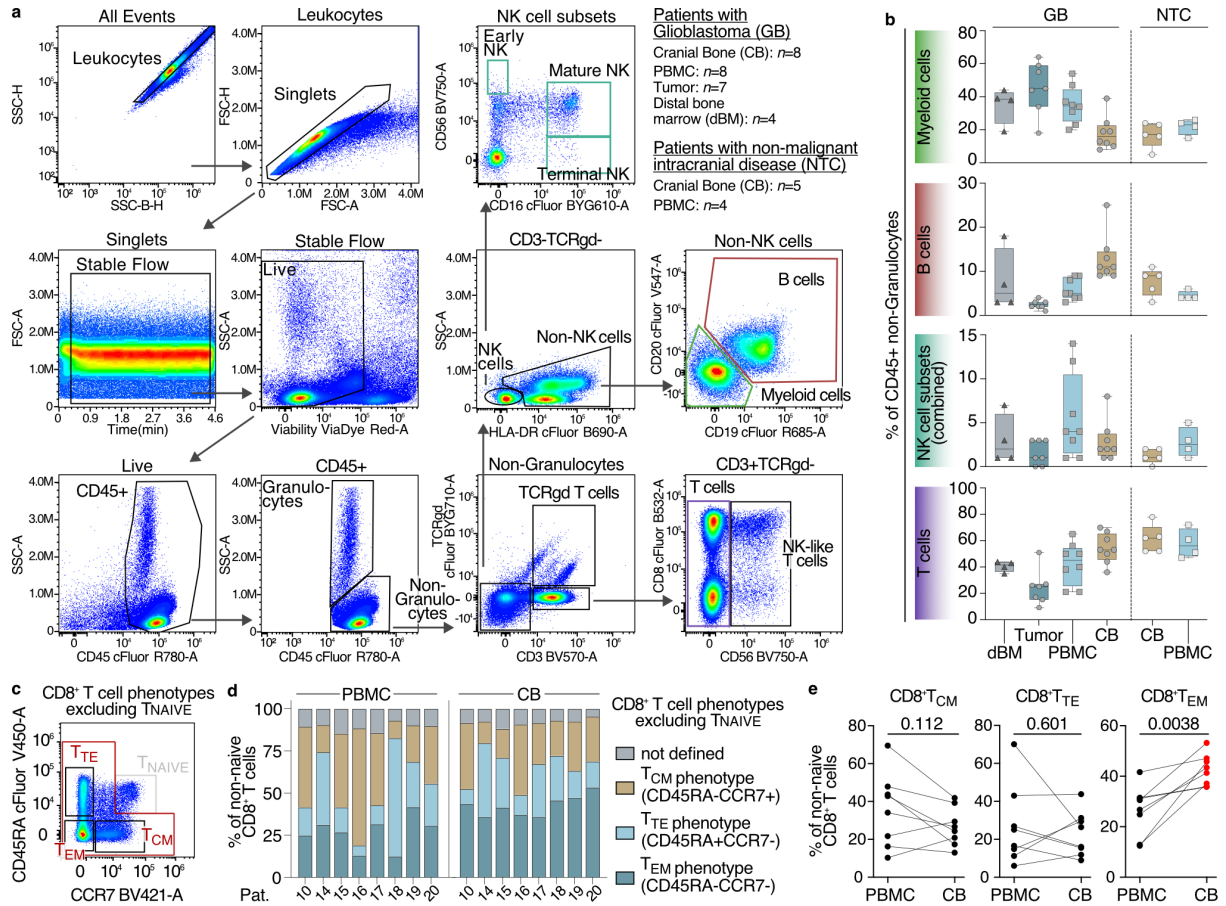
Extended Data Fig. 4: Immune cell quantification based on the Immunoprofiling Assay. a, Representative gating strategy. Identified phenotypes, sample origin/number as indicated. **b,** Boxplot extend from 25th to 75th percentile, displaying median and minimum/maximum ranges as whiskers, summarizing frequency data (% of CD45$^+$ non-granulocytes) of indicated immune cell phenotypes, separated by source. Biological replicates, n indicated in (a). **c,** Representative dotplot displaying selected CD8$^+$ T cell phenotypes, as indicated in red. Note, analysis excluded naive CD8$^+$ T cells. **d,** Stacked bar plot indicating phenotype distribution per patient and source from listed patients. **e,** Graphs show frequencies of phenotypes in paired samples. Biological replicates (n=8). Two-tailed paired t-test; p values indicated.
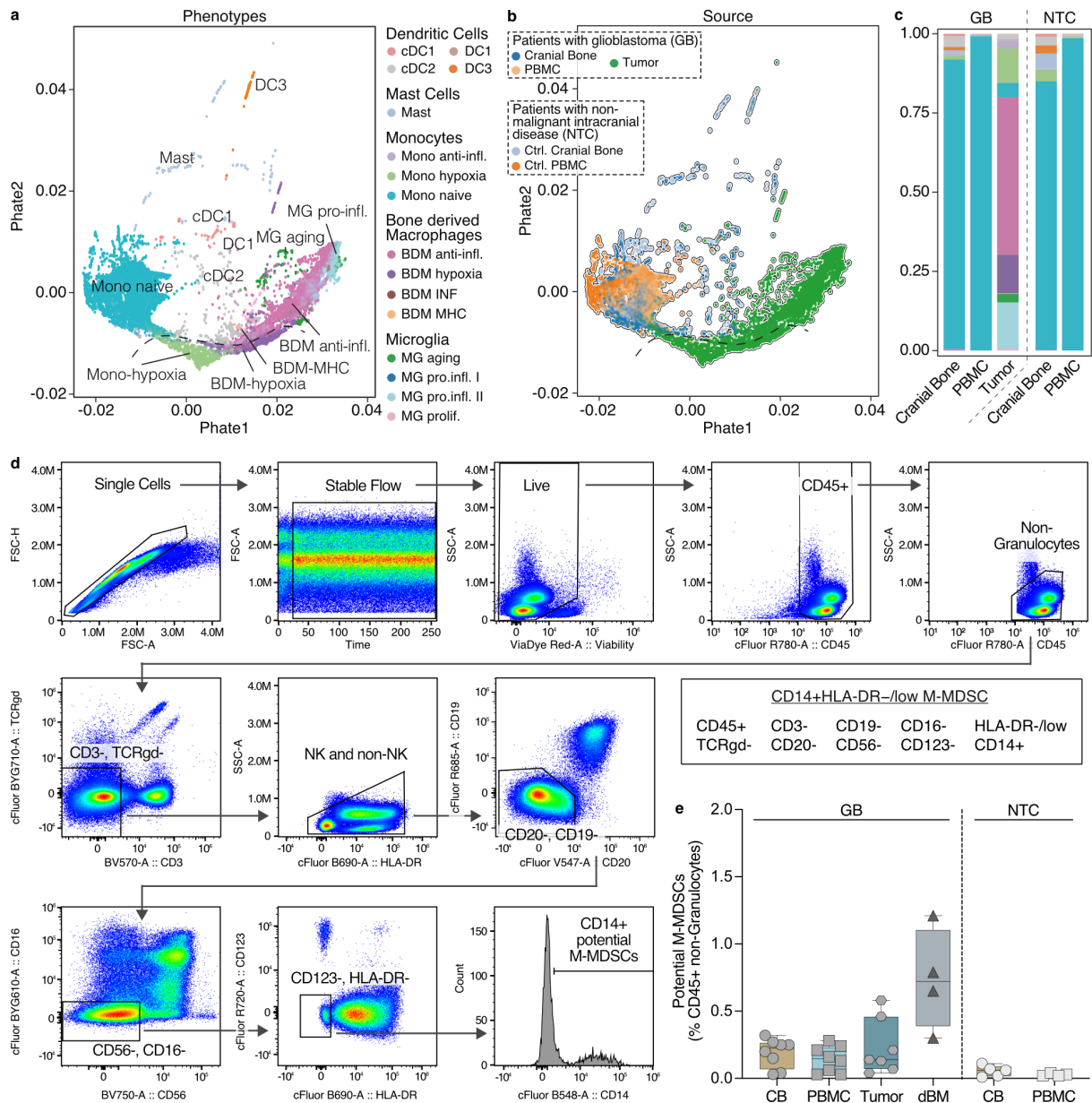
Extended Data Fig. 5: Myeloid compartment. a, Phate plot representing the reference-based annotation of myeloid phenotypes in the single cell data presented in main Fig. 2. **b,** Phate plot as in (a), displaying the distribution of myeloid cells, color coded by source. **c,** Stacked barplots indicate frequencies of myeloid cells per source and disease condition. **d,** Cytometric profiling of myeloid cells. Gating strategy used to identify potential monocytic myeloid-derived suppressor cells (M-MDSCs) utilizing the listed markers. Note, raw data derived from assay shown in Extended Data Fig. 4. **e,** Boxplot extend from 25th to 75th percentile, displaying median and minimum/maximum ranges as whiskers, summarizing frequency data of potential M-MDSCs from (d), separated by source. Biological replicate data from (n) patients: GB-CB (8), -PBMC (8), -Tumor (7), -dBM (4); NTC-CB (5), -PBMC (4).
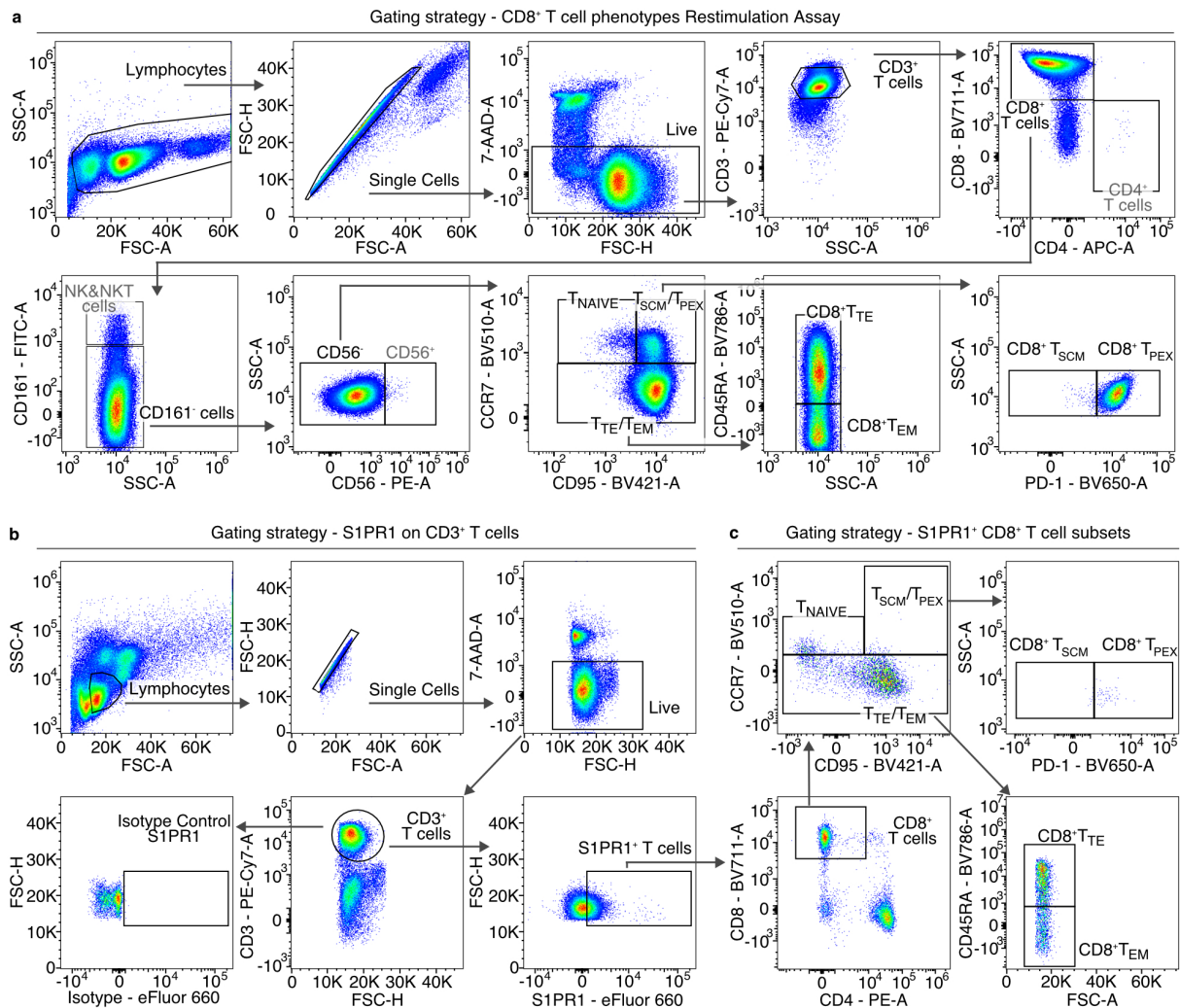
Extended Data Fig. 6: Distinct cytometric gating strategies for selected experimental approaches. a, related to main Fig. 3c, re-stimulation assay. Gating used to identify CD8^{+} T cell subsets at different stages (CD45 expanded, re-stimulation I, II and III). **b,** related to main Fig. 4b, acutely isolated CD45^{+} immune cells. Gating used to identify CD3^{+} T cells expressing S1PR1. **c,** related to main Fig. 4c. Sub-characterization of S1PR1^{+} CD8^{+} T cell phenotypes from (b).
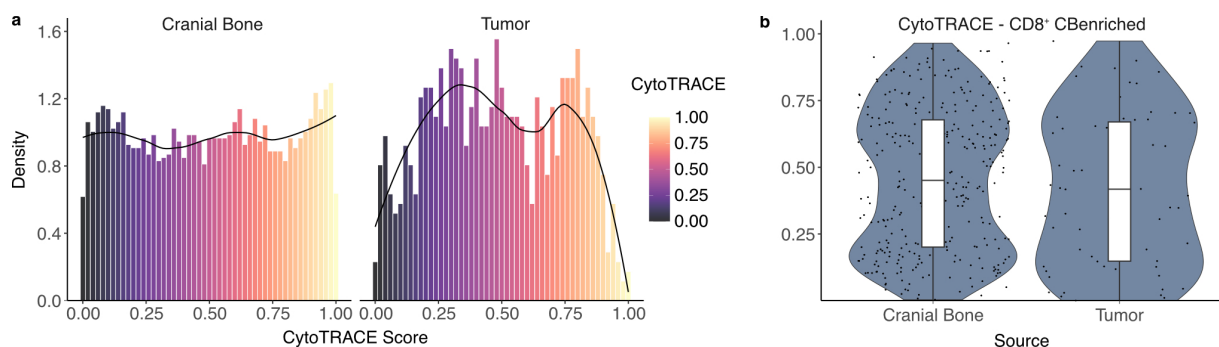
Extended Data Fig. 7: Developmental range assessment. a, Density plot illustrates the distribution of glioblastoma 3' GEX CD8^{+} T cell data across the complete range of CytoTRACE scores, split by source. Note uniform distribution across all developmental stages in CB. **b,** Violin plot illustrating distribution of CBe CD8^{+} T cells across CytoTRACE scores from (a), split by source. Boxplots display median, quartiles, and values within 1.5 * interquartile range as whiskers. Biological replicate data from (n) patients: Cranial Bone (5), Tumor (3). No statistically significant difference detected by two-sided Wilcoxon rank sum test with p value adjustments Holm method (SeuratExtend).
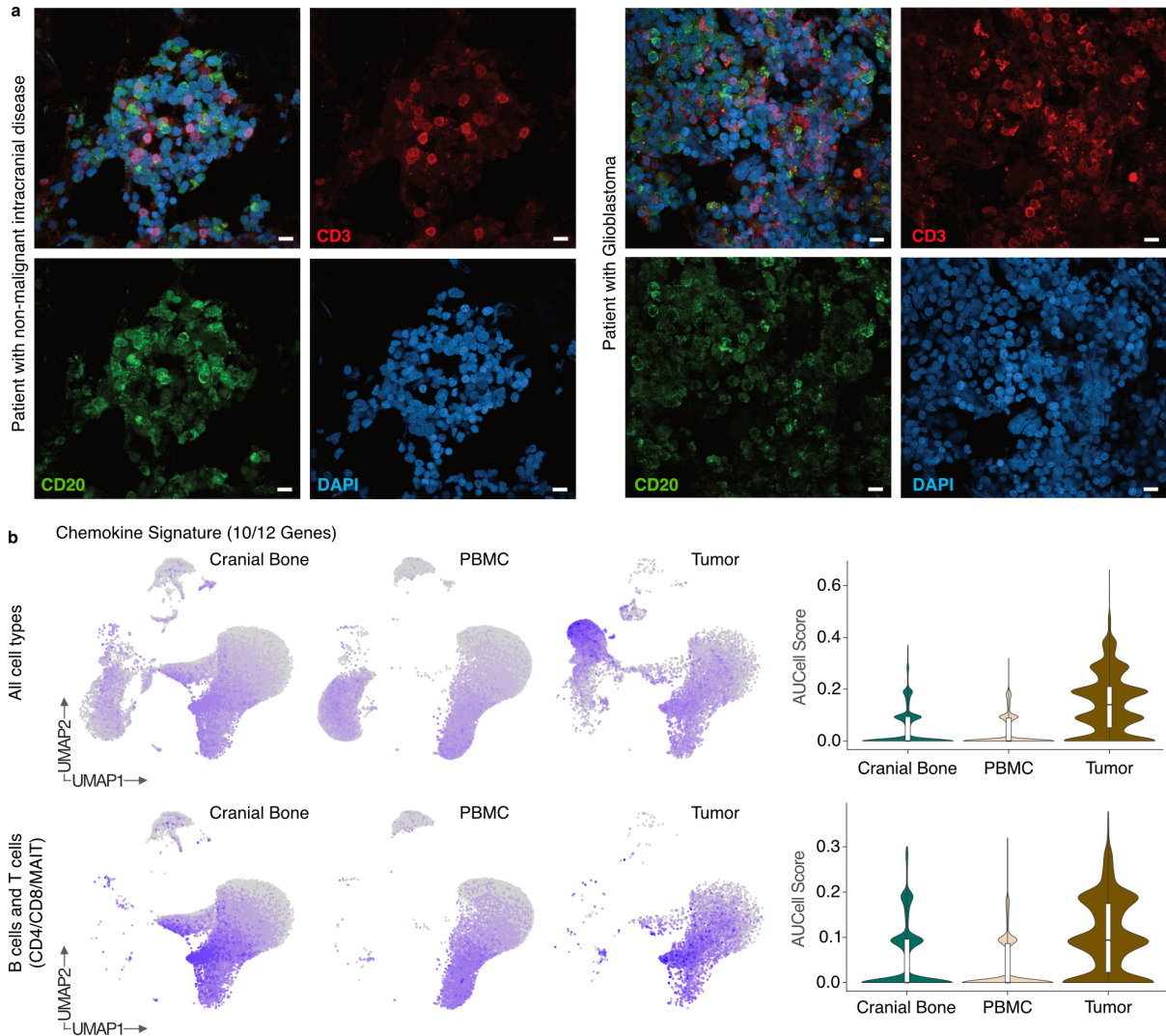
Extended Data Fig. 8: Arrangement of immune cells in the cranial bone. a, Immunofluorescent labeling of CD3 (red; T cells) and CD20 (green; B cells) in histological section from CB fragments of one patient with non-malignant intracranial disease (patient c6), and one patient with glioblastoma (patient 10). Nuclei were DAPI counterstained (blue). Note the lack of higher morphological organization of the tissue. Follicular arrangements, which are characteristic for matured tertiary lymphoid structures are not evident. Scale bars: 10 μm. **b,** Gene set enrichment score of a 12-chemokine reference TLS signature[30] does not indicate enrichment in the CB single cell data set. Scores were calculated via AUCell and depicted as UMAP, colored by score or as a violin plot, respectively, split by biological replicate data source. Cranial Bone (n=13), PBMC (n=10) and Tumor tissue (n=6). Boxplots display median, quartiles, and values within 1.5 * interquartile range as whiskers. Gene set enrichment scores are shown across all annotated cell types (upper panel) or in B and T cells (CD4$^+$/CD8$^+$/MAIT) alone (lower panel).

81
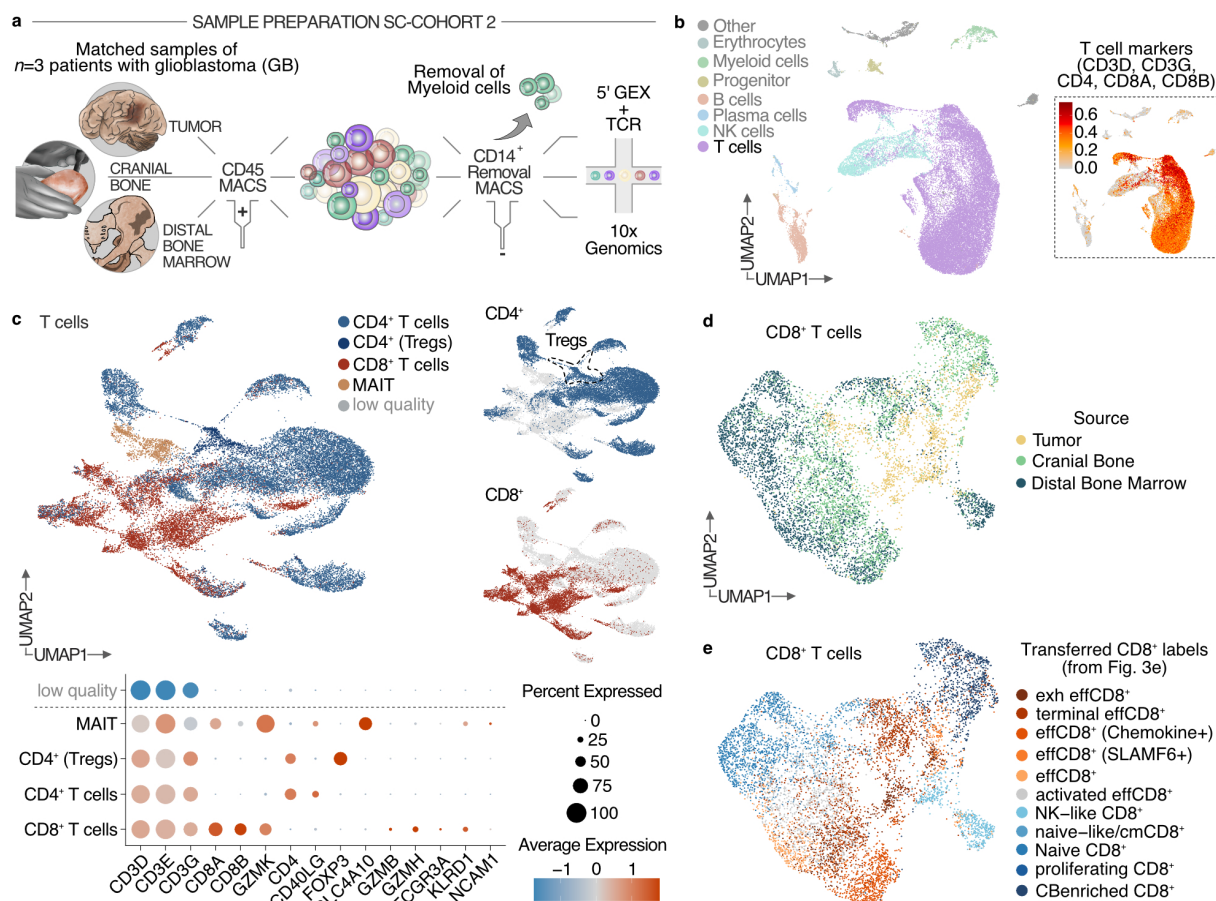
Extended Data Fig. 9: Sample preparation and annotation of sc-cohort 2. a, Sample processing and analysis workflow. Single cells from CB, tumor tissue and distal bone marrow (n = 3; patients 21, 22, 24) were enriched for CD45$^+$/CD14$^-$ cells by magnetic cell separation and further processed for scRNA-seq (10x Genomics) **b,** UMAP projection of integrated space. Inset colored according to the gene set enrichment score of canonical T cell marker genes, calculated via AUCell. **c,** UMAP of all T cells displaying annotated subtypes. Cells annotated as low quality were excluded from subsequent analyses. **d,** UMAP plot of CD8$^+$ T cell subset colored by source. **e,** Annotated CD8$^+$ phenotypes by label-transfer from CD8$^+$ T cells of sc-cohort 1 (see Fig. 3e) using singleCellNet.

Item	(-) Calvarial CXCR4 accumulation (n = 5)	(+) Calvarial CXCR4 accumulation (n = 9)	p-value
Sex			
-Female (n, %)	3 (60.0)	3 (33.3)	0.580 [A]
-Male (n, %)	2 (40.0)	6 (66.7)	
Age [years] (mean ±SD)	66.4 ±12.3	66.9 ±8.3	0.930 [B]
Corticosteroid treatment			
-No (n, %)	3 (60.0)	1 (11.1)	0.095 [A]
-Yes (n, %)	2 (40.0)	8 (88.9)	
MGMT			
-Unmethylated (n, %)	2 (40.0)	2 (22.2)	0.580 [A]
-Methylated (n, %)	3 (60.0)	7 (77.8)	
Extent of resection			
-Biopsy (n, %)	1 (20.0)	0 (0.0)	0.357 [A]
-Gross total (n, %)	4 (80.0)	9 (100.0)	
Applied radioactivity [MBq/kg] (mean ±SD)	2.3 ±0.2	2.3 ±0.3	0.762 [B]
SUV max tumor (mean ±SD)	3.2 ±1.2	3.7 ±0.8	0.359 [B]
SUV mean tumor (mean ±SD)	1.7 ±0.7	1.9 ±0.4	0.362 [B]
SUV peak tumor (mean ±SD)	1.8 ±0.7	2.2 ±0.7	0.321 [B]
Bridge enhancement			
-No (n, %)	3 (60.0)	5 (55.6)	0.999 [B]
-Yes (n, %)	2 (40.0)	4 (44.4)	
PFS [months] (median, range)	4 (3 – 7)	8 (4 – 14)	0.046 [C]

Extended Data Fig. 10: Correlation of clinical and PET-CT/MRI data. a, Design of study. **b,** Data considered for univariate analyses. Note that low number of cases per group (n < 10) precludes multivariate analysis. Abbreviations: A, Two-sided Fisher's exact test; B, two-sided Student's t-test; C, Log-rank (Mantel-Cox) test. n, number of patients with glioblastoma.

Supplementary Information File

Dobersalske et al., Cranioencephalic functional lymphoid units in glioblastoma.

Captions for Supplementary Videos 1–4

Supplementary Video 1. 3D-View of maximum intensity projection of CXCR4 radiolabeling in patient with glioblastoma (Patient 2; Fig. 1c).

Supplementary Video 2. 3D-View of a whole mount immunofluorescence preparation of a cranial bone fragment of a patient with non-malignant intracerebral disease (Patient c3; Fig. 1f).

Supplementary Video 3. 3D-View of a whole mount immunofluorescence preparation of a cranial bone fragment of a patient with glioblastoma (Patient 7; Fig. 1h).

Supplementary Video 4. 3D-View of a whole mount immunofluorescence preparation of a cranial bone fragment of a patient with glioblastoma (Patient 6; Fig. 1i).

Captions for Supplementary Tables 1 - 3

Supplementary Table 1. Data and biosample use of patients with glioblastoma.

Supplementary Table 2. Data and biosample use of patients with non-malignant intracranial disease or Conn's Syndrome.

Supplementary Table 3. Wilcoxon test data, related to Fig. 3i.

Supplementary Table 1: Data and biosample use of patients with glioblastoma

Identifier	CXCR4 PET/CT	Histology (IF)	Lightsheet	scRNA-Seq (CD45+) sc-cohort 1 Cranial Bone	scRNA-Seq (CD45+) sc-cohort 1 PBMCs	scRNA-Seq (CD45+) sc-cohort 1 Tumor	scRNA-Seq (CD45+ CD14-) sc-cohort 2 Cranial Bone	scRNA-Seq (CD45+ CD14-) sc-cohort 2 Tumor	scRNA-Seq (CD45+ CD14-) sc-cohort 2 distal BM	Functional T cell assay	Immuno-profiling	Restimulation	Functional assay Restimulation	SIPR1	Medical center	Diagnosis	MGMT	ATRX	Age	Sex
Patient 1	x			x	x	x									University Hospital Essen	Glioblastoma, IDH-WT (CNS WHO grade 4)	Met	Wt	50	m
Patient 2	x			x	x	x											Met	Wt	68	f
Patient 3	x																Met	Wt	64	m
Patient 4	x			x+VDJ		x+VDJ											Met	Wt	62	m
Patient 5	x																Met	Wt	72	m
Patient 6			x														Met	Wt	45	f
Patient 7			x	x													Unmet	Wt	80	f
Patient 8				x													Met	Wt	54	m
Patient 9				x	x	x											Unmet	Wt	65	m
Patient 10		x								x	x						Met	Wt	65	f
Patient 11										x		x	x				Unmet	Wt	58	m
Patient 12		x															Unmet	Wt	47	f
Patient 13		x															Met	Wt	64	f
Patient 14														x			Unmet	Wt	77	f
Patient 15				x+VDJ	x+VDJ	x+VDJ				x	x	x		x			Unmet	Wt	70	f
Patient 16				x+VDJ	x+VDJ	x+VDJ				x	x	x	x	x			Unmet	Wt	53	m
Patient 17										x	x			x			Met	Wt	54	f
Patient 18											x						Met	Wt	75	f
Patient 19										x	x			x			Unmet	Wt	75	f
Patient 20	x						x+VDJ	x+VDJ	x+VDJ	x	x	x	x	x			Met	Wt	60	f
Patient 21							x+VDJ	x+VDJ	x+VDJ	x	x	x		x			Met	Wt	83	f
Patient 22	x							x+VDJ	x+VDJ		x			x			Met	Wt	70	m
Patient 23	x									x				x			Met	Wt	79	m
Patient 24							x+VDJ	x+VDJ	x+VDJ					x			Met	Wt	66	m
Patient 25	x										x			x			Met	Wt	56	f
Patient 26	x										x			x			Unmet	Wt	66	f
Patient 27														x			Met	Wt	52	m
Patient 28																	Met	Wt	68	f
Patient 29		x															Met	Wt	70	m
Patient 30		x															Unmet	Wt	55	m
Patient 31	x														University Hospital Wuerzburg	Glioblastoma (WHO IV), PMID: 26909116	Met	N/A	64	f
Patient 32	x																Met	N/A	69	f
Patient 33	x																N/A	N/A	75	f
Patient 34	x																N/A	N/A	71	m
Patient 35	x																Unmet	N/A	76	f
Patient 36	x																Unmet	N/A	73	m
Patient 37	x																Met	N/A	50	m
Patient 38	x																Met	N/A	60	f
Patient 39	x																N/A	N/A	77	m

Supplementary Table 2: Data and biosample use of patients with non-malignant intracranial disease or Conn's Syndrome

Identifier	CXCR4 PET/CT	Histology (IF)	Lightsheet	scRNA-Seq (CD45+) sc-cohort 1 — Cranial Bone	scRNA-Seq (CD45+) sc-cohort 1 — PBMCs	Immuno-profiling	Medical center	Diagnosis	Age	Sex
Patient c1	x						University Hospital Essen	Conn's syndrome	53	f
Patient c2	x							Conn's syndrome	42	m
Patient c3		x	x					Subdural hematoma	77	m
Patient c4		x		x	x			Cavernous hemangioma	49	f
Patient c5				x	x	x		Subdural hematoma	65	m
Patient c6		x				x		Normal-pressure hydrocephalus	72	m
Patient c7		x						Subdural hematoma	50	m
Patient c8				x	x	x		Cerebral aneurysm	61	f
Patient c9				x	x	x		Cerebral aneurysm	47	f
Patient c10				x	x	x		Subdural hematoma	77	m
Patient c11	x							Conn's syndrome	44	m
Patient c12	x							Conn's syndrome	46	m
Patient c13	x							Conn's syndrome	67	m
Patient c14	x							Conn's syndrome	60	m
Patient c15		x						Cerebral aneurysm	55	m
Patient c16		x						Subdural hematoma	83	f
Patient c17		x						Subdural hematoma	80	m

85

Supplementary Table 3: Wilcoxon test data, related to Fig. 3i.

Activation:Effector function signature in all effector cells - summarized statistical results					
vs.	PBMC	Cranial Bone	Tumor	Ctrl PBMC	Ctrl Cranial Bone
PBMC		****	****	****	****
Cranial Bone	4,58E-53		****	****	****
Tumor	1,51E-10	3,04E-52		****	****
Ctrl PBMC	5,08E-31	5,14E-205	3,46E-113		****
Ctrl Cranial Bone	9,00E-39	4,96E-11	1,66E-23	1,53E-193	

Extracted statistical results

.y.	group1	group2	n1	n2	statistic	p	p.adj	p.adj.signif
value	PBMC	Cranial Bone	653	3304	666366,5	6,55E-54	4,58E-53	****
value	PBMC	Tumor	653	2300	627812	1,51E-10	1,51E-10	****
value	PBMC	Ctrl PBMC	653	1333	575690,5	1,27E-31	5,08E-31	****
value	PBMC	Ctrl Cranial Bone	653	2644	576905	1,80E-39	9,00E-39	****
value	Cranial Bone	Tumor	3304	2300	4712733	5,06E-53	3,04E-52	****
value	Cranial Bone	Ctrl PBMC	3304	1333	3465783,5	5,14E-206	5,14E-205	****
value	Cranial Bone	Ctrl Cranial Bone	3304	2644	4807143	2,48E-11	4,96E-11	****
value	Tumor	Ctrl PBMC	2300	1333	2224680,5	4,32E-114	3,46E-113	****
value	Tumor	Ctrl Cranial Bone	2300	2644	2535009,5	5,54E-24	1,66E-23	****
value	Ctrl PBMC	Ctrl Cranial Bone	1333	2644	745311,5	1,70E-194	1,53E-193	****

Discussion

The devastating prognosis of patients with glioblastoma provokes extensive research efforts, as demonstrated by 4,359 research outputs in the past year alone (Pubmed result – search criterium "Glioblastoma", year "2023"). The amount of evidence leads to an increasingly detailed dissection of the molecular and cellular components of this archetype of a malignant brain tumor – yet, experimental treatment strategies deviating from the SOC are only suggested as part of clinical studies [80]. Through the years, various approaches such as targeted therapy [24], extent of surgical tumor resection [13, 15, 16], immunotherapy [47, 81, 82], and low-intensity electric fields [2, 3] have been explored. While the latter shows improved progression-free and overall survival when applied adjunct to the SOC [5, 83], the prognosis of patients with glioblastoma remains dismal with a median overall survival of less than 2 years [83]. As previously elaborated, immunotherapies have not yet replicated their success in intracranial tumors [38, 39]. However, the potential influence of tumor-adjacent niches on treatment efficacy may have been largely overlooked in this context.

The neuro-immune interface and the TME of glioblastoma

Advanced molecular analyses have drawn attention to the TME of glioblastoma. Studies investigated the cell-cell interactions of tumor cells with brain tissue resident cell types, such as microglia, astrocytes and neurons [56, 58, 61]. Additionally, intricate immune cellular interactions with infiltrating monocytic or lymphoid cells, such as macrophages or T cells, have been explored [58, 60, 84]. With expanding knowledge about the neuro-immune interface as a reservoir of CNS immune cells, the cellular composition of local immune cell niches and their role in shaping the TME in GB warrants more detailed investigation [75].

We pinpointed an unexpected presence of HSPCs in the TME of patients with glioblastoma [85]. Surprisingly, HSPCs displayed immunosuppressive and tumor-promoting characteristics. This was evidenced, for instance, by the release of tumor promoting cytokines, such as interleukin-8 (IL-8) [86], or the induction of the immune checkpoint PD-L1 on the tumor cell surface in co-culture models *in-vitro*. Notably, HSCs and their cellular progeny were detected as predictors of overall survival in patients with glioblastoma, indicating worse clinical outcome in HSC-high GB tissues [85]. Their negative prognostic role and increased presence within the parenchyma of glioblastoma tissue prompted an investigation of their spatial origin. Given the

expanding knowledge on the skull bone as a potential reservoir of immune cells at the CNS border's [69, 71, 75], we hypothesized that the local cranial bone marrow could directly contribute to these and other immune cells in the TME of glioblastoma tumors.

The bone marrow is a crucial organ for hematopoiesis. Hematopoietic stem cells preferentially reside in bone marrows, are self-renewing and eventually give rise to various kinds of immune cells [87, 88]. However, given that aging bone marrow typically shows progressive tissue attrition [88], the prominent tumor-adjacent accumulation of immune cells that we found in the CB of the mature patient population was unexpected [89]. Immunoprofiling and scRNAseq revealed a diverse repertoire of immune cells, characterized by a prominent accumulation of T cells [89]. Even though HSPCs were not the predominant fraction among these immune cells, we were able to detect their presence within the CB of patients with GB. Notably, a preferential association of cycling HSCs has been reported in vicinity to C-X-C motif chemokine ligand 12+ (CXCL12) stromal cells in mice [90]. Thus, the detection of this chemokine in the CB of patients with GB further supported the notion of an active, local immune cell niche.

We identified activated, tumor-reactive CD8+ T cells within this niche, capable of recognizing and killing tumor cells [89]. According to the cancer-immunity cycle, these CD8+ T cells need to be primed to recognize and destruct their target tumor cells [32, 33]. As tertiary lymphoid structures (TLS) can serve as sites for T cell priming [33], we considered their formation in the CB, but we did not find sufficient evidence for a fully developed TLS [89]. Therefore, one may hypothesize that other yet less characterized cells among the immune cell population within the CB may act as T cell priming APCs. Contrary to the immunosuppressive role of HSPCs that we observed in the GB parenchyma, it should be noted that HSPCs can also have an immunogenic role, e.g. by surface presentation of antigens via the MHC [91]. Thus, their role in patients with glioblastoma may depend on their location, as they may actively contribute to the priming of tumor specific T cells in the CB. Albeit antigen presentation is executed specifically via MHC class II to the T cell receptor of CD4+ T cells, HSPCs also can give rise to other APCs, such as dendritic cells or B cells [91, 92]. B cells are known residents at the CNS borders [71], and HSPCs in the cranial bone may contribute to their population.

CSF represents the medium of lymphatic brain drainage [76, 77], which has direct access to the skull marrow [78]. Given the proximity of CB and tumor parenchyma, one may ask whether GB-specific cues released into the CSF [93] could induce a dual

effect in the skull. For one, the communication axis could facilitate the presentation of tumor antigens to CD8^{+} T cells. Alternatively, it could influence the local differentiation and subsequent recruitment of tumor-promoting immune cells, such as TAMs, to the TME. Notably, this signaling axis has been observed during CNS injury, where CSF-mediated signals have been reported to instruct myelopoiesis in the skull bone marrow [78]. Considering the identification of the CB as a reservoir to replenish myeloid cells in non-neoplastic CNS conditions [74, 78], coupled with a relative short lifespan (<1 week) of monocytes [94], it is tempting to speculate that the CB serves as a local source for immunosuppressive TAMs in the setting of human brain tumors. Even though, we did not detect specific myeloid-derived suppressor cells in the cranial bone of patients with glioblastoma, one may assume that a conversion of myeloid cells to a suppressive state within the tumor parenchyma may occur [95]. Notably, in experimental cell culture models, we could observe the release of pro-inflammatory cytokines, such as interleukin-6 (IL-6) from tumor-associated HSPCs [85], which can induce the production of IL-10 from TAMs and thus drive T cell exhaustion [54, 96]. Indeed, in HSC-high glioblastoma tissue samples, we detected an increased expression of the gene encoding *IL-10* [85]. This may suggest a potential mechanism by which the glioblastoma TME recruits HSPCs from the proximal cranial bone to facilitate immune evasion. Notably, a TAM-mediated immunosuppressive effect, inhibiting the effector function of lymphocytes, has been observed after the administration of pembrolizumab, an antibody against PD-1 designed to stimulate T cell response [97]. This raises the question of how the neuro-immune interface may impact on T cell responses and whether this inhibits the success of immunotherapies in glioblastoma.

Impact on the therapy of patients with glioblastoma

The infiltration of brain tumors with T cells has generally been reported to be low, contributing to the characterization of a "cold immune phenotype" [38]. Despite their limited number, the abundance of T cells at the time of tumor recurrence has been associated with improved survival [49]. Yet, these infiltrating T cells have been reported to exhibit an exhausted phenotype [49], an observation consistent with our data [89]. While it might seem paradoxical, the observation in fact suggests immunotherapies targeting immune checkpoints on T cells as promising for future brain tumor treatment strategy.

There are current reports of clonally expanded T cells with effector properties in pediatric brain tumors [98], which adds to our discovery of tumor-shared reactive CD8+ T cell clonotypes in the CB. We identified the presence of a potent source of non-exhausted, activated CD8+ T cells in the CB, right next to the tumor parenchyma [89]. It allows the speculation that preserving the integrity of this structure, together with a pre-surgical neoadjuvant or local application of immunotherapy, may improve the trafficking tumor-reactive T cells to the tumor. By SOC, patients undergo routine craniotomy, the surgical temporary removal of a skull fraction, to allow access to their brain [12, 80]. During the time of surgery, and sometimes even thereafter (e.g. in case of a cerebral edema), the bone flap is temporarily removed and stored outside of the body. This disconnection may potentially impact on the vitality of immune cells in the CB (Figure 2). In addition, it has been considered that the immune cell reservoirs in bone and meninges may be connected to the CNS by "specialized forms of neuroimmune communication" [75], a connection that may be destroyed during surgery. Furthermore, the local instruction of immune cells via CSF-derived antigens may be disrupted permanently after surgery in the disconnected bone.
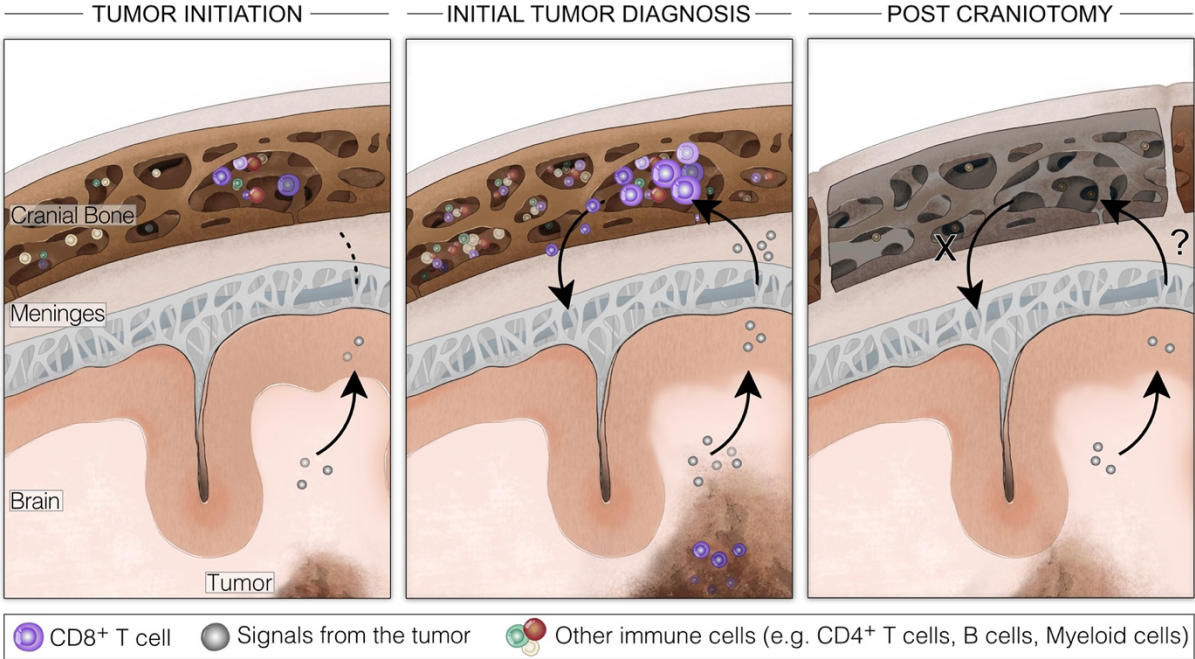
Figure 2: Hypothesis of the potential impact of craniotomy on the immune cell niche in CB of patients with glioblastoma. Left: At time of tumor initiation, signals from the tumor, e.g. tumor-derived are released and drained into the CSF. Center: CSF-derived tumor signals instruct local proliferation of immune cells in the CB of glioblastoma patients. Tumor-reactive CD8+ T cells from the CB subsequently infiltrate the tumor. Right: The reimplanted disconnected bone flap after craniotomy lacking the presence of immune cells within the CB.

A therapeutic approach preserving the integrity of the local CB and the brain tumor in its proximity may promote beneficial T cell trafficking, but this thought would require a deviation from current guideline-based standards of care in patients with glioblastoma [1, 7, 99]. Møllgård *et al.* [68] speculated that disrupting the integrity of the neuro-immune cell niches could negatively impact immune surveillance. They proposed, that a disruption of the SLYM might alter CSF flow patterns or immune cell influx to the brain, thus contributing, for example, to prolonged stages of neuroinflammation [68]. However, it may also be possible that these niches regenerate after injury or surgical disruption. In fact, the neoadjuvant application of αPD-1 antibodies in patients with recurrent glioblastoma has shown improved survival and increased clonal T cell diversity [81, 82]. This suggests that guardian immune cells, residing at the CNS borders, may regenerate and profit from an immunotherapeutic stimulation, and even that patients may experience benefit from such treatments at the time of initial diagnosis, prior to the first surgery.

Analysis of scRNAseq data after neoadjuvant administration of the αPD-1 antibody pembrolizumab revealed an upregulation of chemotaxis genes, such as *CC-chemokine ligand 5* (*CCL5*), in GB-infiltrating T cells [97]. This suggests an immunotherapy-induced mechanism where additional T cells or antigen-presenting cells such as DCs are recruited to the scene [97, 100]. Although Lee *et al.* proposed the infiltration from systemic circulation [97], our discovery of the CB immune cell niche, encompassing the complete T cell developmental trajectory [89], also suggests a local bone marrow source for these cells. This opens up the exciting consideration of neoadjuvant, local, T cell-engaging therapies as an alternative approach to stimulate immune responses in patients with glioblastoma. Potential benefits from local therapy in the CNS have recently been highlighted by the administration of engineered T cells to the ventricle [47, 101]. The structure located therein, that is the choroid plexus, belongs to the neuro-immune interface and facilitates the passage of immune cells to the CSF in both brain homeostasis and pathology [102]. Locoregional administered CAR T cells [47, 101] and their therapeutic trajectories highlight the future potential of endogenous immune cell recruitment strategies from the neuro-immune interface. These strategies may encompass neoadjuvant approaches that modulate infiltration of guardian immune cells while preserving the intricate and potentially private communication between the tumor and the cranial bone.

Conclusion and outlook

This thesis work provides evidence of hematopoietic stem and progenitor cells within the TME that are positively linked to disease progression and, at the same time, the discovery of an anti-tumor immune cell niche in the skull bone marrow of patients with glioblastoma.

The presence of HSPCs in the parenchyma of glioblastoma tumor tissue was unexpected, and the experimental detection of their immunosuppressive and tumor-promoting characteristics were particularly surprising [85]. In contrast to reports from animal models, describing favorable outcomes with intravenously injected HSPCs [103], an *in-vitro* co-culture model with human glioblastoma cells displayed an upregulation of the immune checkpoint PD-L1 on the cancer cell surface [85], a mechanism that can contribute to T cell dysfunction [33]. Together with the secretion of cytokines, such as IL-6 or IL-8, which may directly or indirectly contribute to an immunosuppressive environment, these cells present an unexpected potential target to address immunosuppression in the TME of glioblastoma.

At time of the detection of HSPCs in the tumor parenchyma of clinical glioblastoma samples, we were unaware of a potential significance of the neuro-immune interface in the setting of CNS tumors. However, as our data show an immunogenic niche in the cranial bone of patients with glioblastoma [89], the presence of immunosuppressive HSPCs in the brain tumor parenchyma [85] may be unrelated. The thesis work describes, for the first time in the context of human brain tumors, an immune cell niche in the tumor-adjacent bone of patients with glioblastoma. CB-residing, tumor-reactive CD8^{+} T cells are shared with the brain tumor and can specifically recognize and destroy tumor cells [89]. Despite this discovery, a lot of open questions remain that necessitate further investigation in follow-up studies. The presence of tumor-reactive CD8^{+} T cells is supported by reports of antigen presentation by APCs around the dural sinus [67]. However, we currently lack evidence for the presentation of antigens to specifically activated CD8^{+} T cells within the CB. It remains to be investigated whether T cell priming in the setting of CNS tumors occurs, for example, around the dural sinus with subsequent sequestration to the bone marrow, or if activation takes place directly within the bone. In this context, other CB immune cells, such as DCs, B cells or CD4^{+} T cells, should be studied in more detail. Moreover, it should be acknowledged that enhanced T cell infiltration may not be sufficient to improve clinical outcome. Even if increased T cell traffic from the proximal bone could be promoted, we and others report

an exhausted T cell phenotype in the tumor parenchyma [49, 54]. This dysfunctional T cell state is potentially caused by the neighboring cells in the TME and their release of immunosuppressive cytokines [54, 61], a condition that needs to be addressed to improve patient's outcome.

Timing and location may represent the cornerstones of success for immunotherapies in glioblastoma. Preservation of the CB structure and the immune cell niche therein may be considered to improve immunotherapeutic strategies in patients with newly-diagnosed disease. Further research should be directed to identify biomarkers allowing the stratification of patients for neoadjuvant immunotherapy, e.g. by an imaging-informed approach involving the clinical use of radioactive PET-tracers. The presence of an active local immune cell niche in the cranial bone of patients with glioblastoma is unexpected. Preserving the niche and stimulating the specialized communication with the tumor may represent a next translation effort to forward basic discovery to clinical application towards successful therapeutic intervention.

References

1.   Stupp, R., et al., *Radiotherapy plus concomitant and adjuvant temozolomide for glioblastoma.* N Engl J Med, 2005. **352**(10): p. 987-96.
2.   Hottinger, A.F., P. Pacheco, and R. Stupp, *Tumor treating fields: a novel treatment modality and its use in brain tumors.* Neuro Oncol, 2016. **18**(10): p. 1338-49.
3.   Stupp, R., et al., *Maintenance Therapy With Tumor-Treating Fields Plus Temozolomide vs Temozolomide Alone for Glioblastoma: A Randomized Clinical Trial.* JAMA, 2015. **314**(23): p. 2535-43.
4.   Gilbert, M.R., et al., *A randomized trial of bevacizumab for newly diagnosed glioblastoma.* N Engl J Med, 2014. **370**(8): p. 699-708.
5.   Stupp, R., et al., *Effect of Tumor-Treating Fields Plus Maintenance Temozolomide vs Maintenance Temozolomide Alone on Survival in Patients With Glioblastoma: A Randomized Clinical Trial.* JAMA, 2017. **318**(23): p. 2306-2316.
6.   Ostrom, Q.T., et al., *CBTRUS Statistical Report: Primary Brain and Other Central Nervous System Tumors Diagnosed in the United States in 2016-2020.* Neuro Oncol, 2023. **25**(12 Suppl 2): p. iv1-iv99.
7.   Wen, P.Y., et al., *Glioblastoma in adults: a Society for Neuro-Oncology (SNO) and European Society of Neuro-Oncology (EANO) consensus review on current management and future directions.* Neuro Oncol, 2020. **22**(8): p. 1073-1113.
8.   Weller, M., et al., *European Association for Neuro-Oncology (EANO) guideline on the diagnosis and treatment of adult astrocytic and oligodendroglial gliomas.* Lancet Oncol, 2017. **18**(6): p. e315-e329.
9.   Venkataramani, V., et al., *Glioblastoma hijacks neuronal mechanisms for brain invasion.* Cell, 2022. **185**(16): p. 2899-2917 e31.
10. Drumm, M.R., et al., *Extensive brainstem infiltration, not mass effect, is a common feature of end-stage cerebral glioblastomas.* Neuro Oncol, 2020. **22**(4): p. 470-479.
11. Weller, M., et al., *Glioma.* Nat Rev Dis Primers, 2024. **10**(1): p. 33.
12. Weller, M., et al., *EANO guidelines on the diagnosis and treatment of diffuse gliomas of adulthood.* Nat Rev Clin Oncol, 2021. **18**(3): p. 170-186.
13. Stummer, W., et al., *Fluorescence-guided surgery with 5-aminolevulinic acid for resection of malignant glioma: a randomised controlled multicentre phase III trial.* Lancet Oncol, 2006. **7**(5): p. 392-401.
14. Jenkinson, M.D., et al., *Intraoperative imaging technology to maximise extent of resection for glioma.* Cochrane Database Syst Rev, 2018. **1**(1): p. CD012788.
15. Brown, T.J., et al., *Association of the Extent of Resection With Survival in Glioblastoma: A Systematic Review and Meta-analysis.* JAMA Oncol, 2016. **2**(11): p. 1460-1469.
16. Ellingson, B.M., et al., *Validation of postoperative residual contrast-enhancing tumor volume as an independent prognostic factor for overall survival in newly diagnosed glioblastoma.* Neuro Oncol, 2018. **20**(9): p. 1240-1250.
17. *WHO Classification of Tumors Editorial Board. Central nervous system tumours. Lyon (France): International Agency for Research on Cancer.* 2021. (WHO classification of tumours series, 5th ed.; vol. 6).

18. Cancer Genome Atlas Research, N., *Comprehensive genomic characterization defines human glioblastoma genes and core pathways.* Nature, 2008. **455**(7216): p. 1061-8.

19. Ceccarelli, M., et al., *Molecular Profiling Reveals Biologically Discrete Subsets and Pathways of Progression in Diffuse Glioma.* Cell, 2016. **164**(3): p. 550-63.

20. Verhaak, R.G., et al., *Integrated genomic analysis identifies clinically relevant subtypes of glioblastoma characterized by abnormalities in PDGFRA, IDH1, EGFR, and NF1.* Cancer Cell, 2010. **17**(1): p. 98-110.

21. Barthel, F.P., et al., *Longitudinal molecular trajectories of diffuse glioma in adults.* Nature, 2019. **576**(7785): p. 112-120.

22. Lombardi, G., et al., *Regorafenib compared with lomustine in patients with relapsed glioblastoma (REGOMA): a multicentre, open-label, randomised, controlled, phase 2 trial.* Lancet Oncol, 2019. **20**(1): p. 110-119.

23. Lassman, A.B., et al., *Depatuxizumab mafodotin in EGFR-amplified newly diagnosed glioblastoma: A phase III randomized clinical trial.* Neuro Oncol, 2023. **25**(2): p. 339-350.

24. Dewdney, B., et al., *From signalling pathways to targeted therapies: unravelling glioblastoma's secrets and harnessing two decades of progress.* Signal Transduct Target Ther, 2023. **8**(1): p. 400.

25. Lin, B., et al., *EGFR, the Lazarus target for precision oncology in glioblastoma.* Neuro Oncol, 2022. **24**(12): p. 2035-2062.

26. De Silva, M.I., B.W. Stringer, and C. Bardy, *Neuronal and tumourigenic boundaries of glioblastoma plasticity.* Trends Cancer, 2023. **9**(3): p. 223-236.

27. Wolchok, J., *Putting the Immunologic Brakes on Cancer.* Cell, 2018. **175**(6): p. 1452-1454.

28. Saxena, M., et al., *Therapeutic cancer vaccines.* Nat Rev Cancer, 2021. **21**(6): p. 360-378.

29. Waldman, A.D., J.M. Fritz, and M.J. Lenardo, *A guide to cancer immunotherapy: from T cell basic science to clinical practice.* Nat Rev Immunol, 2020. **20**(11): p. 651-668.

30. Takaba, H. and H. Takayanagi, *The Mechanisms of T Cell Selection in the Thymus.* Trends Immunol, 2017. **38**(11): p. 805-816.

31. van den Broek, T., J.A.M. Borghans, and F. van Wijk, *The full spectrum of human naive T cells.* Nat Rev Immunol, 2018. **18**(6): p. 363-373.

32. Chen, D.S. and I. Mellman, *Oncology meets immunology: the cancer-immunity cycle.* Immunity, 2013. **39**(1): p. 1-10.

33. Mellman, I., et al., *The cancer-immunity cycle: Indication, genotype, and immunotype.* Immunity, 2023. **56**(10): p. 2188-2205.

34. Sun, Q., et al., *Immune checkpoint therapy for solid tumours: clinical dilemmas and future trends.* Signal Transduct Target Ther, 2023. **8**(1): p. 320.

35. Robert, C., *A decade of immune-checkpoint inhibitors in cancer therapy.* Nat Commun, 2020. **11**(1): p. 3801.

36. Reck, M., J. Remon, and M.D. Hellmann, *First-Line Immunotherapy for Non-Small-Cell Lung Cancer.* J Clin Oncol, 2022. **40**(6): p. 586-597.

37. Wolchok, J.D., et al., *Long-Term Outcomes With Nivolumab Plus Ipilimumab or Nivolumab Alone Versus Ipilimumab in Patients With Advanced Melanoma.* J Clin Oncol, 2022. **40**(2): p. 127-137.

38. Sampson, J.H., et al., *Brain immunology and immunotherapy in brain tumours.* Nat Rev Cancer, 2020. **20**(1): p. 12-25.

39. Jackson, C.M., J. Choi, and M. Lim, *Mechanisms of immunotherapy resistance: lessons from glioblastoma.* Nat Immunol, 2019. **20**(9): p. 1100-1109.

40. June, C.H. and M. Sadelain, *Chimeric Antigen Receptor Therapy.* N Engl J Med, 2018. **379**(1): p. 64-73.

41. Schuster, S.J., et al., *Tisagenlecleucel in Adult Relapsed or Refractory Diffuse Large B-Cell Lymphoma.* N Engl J Med, 2019. **380**(1): p. 45-56.

42. Berdeja, J.G., et al., *Ciltacabtagene autoleucel, a B-cell maturation antigen-directed chimeric antigen receptor T-cell therapy in patients with relapsed or refractory multiple myeloma (CARTITUDE-1): a phase 1b/2 open-label study.* Lancet, 2021. **398**(10297): p. 314-324.

43. Qi, C., et al., *Claudin18.2-specific CAR T cells in gastrointestinal cancers: phase 1 trial interim results.* Nat Med, 2022. **28**(6): p. 1189-1198.

44. Narayan, V., et al., *PSMA-targeting TGFbeta-insensitive armored CAR T cells in metastatic castration-resistant prostate cancer: a phase 1 trial.* Nat Med, 2022. **28**(4): p. 724-734.

45. O'Rourke, D.M., et al., *A single dose of peripherally infused EGFRvIII-directed CAR T cells mediates antigen loss and induces adaptive resistance in patients with recurrent glioblastoma.* Sci Transl Med, 2017. **9**(399).

46. Brown, C.E., et al., *Regression of Glioblastoma after Chimeric Antigen Receptor T-Cell Therapy.* N Engl J Med, 2016. **375**(26): p. 2561-9.

47. Choi, B.D., et al., *Intraventricular CARv3-TEAM-E T Cells in Recurrent Glioblastoma.* N Engl J Med, 2024. **390**(14): p. 1290-1298.

48. Neftel, C., et al., *An Integrative Model of Cellular States, Plasticity, and Genetics for Glioblastoma.* Cell, 2019. **178**(4): p. 835-849 e21.

49. Wang, L., et al., *A single-cell atlas of glioblastoma evolution under therapy reveals cell-intrinsic and cell-extrinsic therapeutic targets.* Nat Cancer, 2022. **3**(12): p. 1534-1552.

50. Yeo, A.T., et al., *Single-cell RNA sequencing reveals evolution of immune landscape during glioblastoma progression.* Nat Immunol, 2022. **23**(6): p. 971-984.

51. Abdelfattah, N., et al., *Single-cell analysis of human glioma and immune cells identifies S100A4 as an immunotherapy target.* Nat Commun, 2022. **13**(1): p. 767.

52. Greenwald, A.C., et al., *Integrative spatial analysis reveals a multi-layered organization of glioblastoma.* Cell, 2024. **187**(10): p. 2485-2501 e26.

53. Mathur, R., et al., *Glioblastoma evolution and heterogeneity from a 3D whole-tumor perspective.* Cell, 2024. **187**(2): p. 446-463 e16.

54. Ravi, V.M., et al., *T-cell dysfunction in the glioblastoma microenvironment is mediated by myeloid cells releasing interleukin-10.* Nat Commun, 2022. **13**(1): p. 925.

55. Venkataramani, V., et al., *Glutamatergic synaptic input to glioma cells drives brain tumour progression.* Nature, 2019. **573**(7775): p. 532-538.

56. Venkatesh, H.S., et al., *Electrical and synaptic integration of glioma into neural circuits.* Nature, 2019. **573**(7775): p. 539-545.

57. Klemm, F., et al., *Interrogation of the Microenvironmental Landscape in Brain Tumors Reveals Disease-Specific Alterations of Immune Cells.* Cell, 2020. **181**(7): p. 1643-1660 e17.

58. Quail, D.F. and J.A. Joyce, *The Microenvironmental Landscape of Brain Tumors.* Cancer Cell, 2017. **31**(3): p. 326-341.

59. Mantovani, A., et al., *Tumour-associated macrophages as treatment targets in oncology.* Nat Rev Clin Oncol, 2017. **14**(7): p. 399-416.

60. Watowich, M.B., M.R. Gilbert, and M. Larion, *T cell exhaustion in malignant gliomas.* Trends Cancer, 2023. **9**(4): p. 270-292.

61. Henrik Heiland, D., et al., *Tumor-associated reactive astrocytes aid the evolution of immunosuppressive environment in glioblastoma.* Nat Commun, 2019. **10**(1): p. 2541.

62. Zhai, L., et al., *Tumor Cell IDO Enhances Immune Suppression and Decreases Survival Independent of Tryptophan Metabolism in Glioblastoma.* Clin Cancer Res, 2021. **27**(23): p. 6514-6528.

63. Nduom, E.K., et al., *PD-L1 expression and prognostic impact in glioblastoma.* Neuro Oncol, 2016. **18**(2): p. 195-205.

64. Woroniecka, K., et al., *T-Cell Exhaustion Signatures Vary with Tumor Type and Are Severe in Glioblastoma.* Clin Cancer Res, 2018. **24**(17): p. 4175-4186.

65. Zhou, S., et al., *Reprogramming systemic and local immune function to empower immunotherapy against glioblastoma.* Nat Commun, 2023. **14**(1): p. 435.

66. Chongsathidkiet, P., et al., *Sequestration of T cells in bone marrow in the setting of glioblastoma and other intracranial tumors.* Nat Med, 2018. **24**(9): p. 1459-1468.

67. Rustenhoven, J., et al., *Functional characterization of the dural sinuses as a neuroimmune interface.* Cell, 2021. **184**(4): p. 1000-1016 e27.

68. Mollgard, K., et al., *A mesothelium divides the subarachnoid space into functional compartments.* Science, 2023. **379**(6627): p. 84-88.

69. Castellani, G., et al., *Transforming the understanding of brain immunity.* Science, 2023. **380**(6640): p. eabo7649.

70. Sankowski, R., et al., *Multiomic spatial landscape of innate immune cells at human central nervous system borders.* Nat Med, 2024. **30**(1): p. 186-198.

71. Brioschi, S., et al., *Heterogeneity of meningeal B cells reveals a lymphopoietic niche at the CNS borders.* Science, 2021. **373**(6553).

72. Wang, A.Z., et al., *Single-cell profiling of human dura and meningioma reveals cellular meningeal landscape and insights into meningioma immune response.* Genome Med, 2022. **14**(1): p. 49.

73. Dani, N., et al., *A cellular and spatial map of the choroid plexus across brain ventricles and ages.* Cell, 2021. **184**(11): p. 3056-3074 e21.

74. Cugurra, A., et al., *Skull and vertebral bone marrow are myeloid cell reservoirs for the meninges and CNS parenchyma.* Science, 2021. **373**(6553).

75. Mazzitelli, J.A., et al., *Skull bone marrow channels as immune gateways to the central nervous system.* Nat Neurosci, 2023. **26**(12): p. 2052-2062.

76. Louveau, A., et al., *Structural and functional features of central nervous system lymphatic vessels.* Nature, 2015. **523**(7560): p. 337-41.

77. Iliff, J.J., et al., *A paravascular pathway facilitates CSF flow through the brain parenchyma and the clearance of interstitial solutes, including amyloid beta.* Sci Transl Med, 2012. **4**(147): p. 147ra111.

78. Mazzitelli, J.A., et al., *Cerebrospinal fluid regulates skull bone marrow niches via direct access through dural channels.* Nat Neurosci, 2022. **25**(5): p. 555-560.

79. Herisson, F., et al., *Direct vascular channels connect skull bone marrow and the brain surface enabling myeloid cell migration.* Nat Neurosci, 2018. **21**(9): p. 1209-1217.

80. Wick, W., *Gliome, S2k-Leitlinie, 2021 in: Deutsche Gesellschaft für Neurologie (Hrsg.), Leitlinien für Diagnostik und Therapie in der Neurologie. Online: www.dgn.org/leitlinien (abgerufen am 23.06.2024).*

81. Schalper, K.A., et al., *Neoadjuvant nivolumab modifies the tumor immune microenvironment in resectable glioblastoma.* Nat Med, 2019. **25**(3): p. 470-476.

82. Cloughesy, T.F., et al., *Neoadjuvant anti-PD-1 immunotherapy promotes a survival benefit with intratumoral and systemic immune responses in recurrent glioblastoma.* Nat Med, 2019. **25**(3): p. 477-486.

83. Ballo, M.T., et al., *Association of Tumor Treating Fields (TTFields) therapy with survival in newly diagnosed glioblastoma: a systematic review and meta-analysis.* J Neurooncol, 2023. **164**(1): p. 1-9.

84. Zhou, W., et al., *Periostin secreted by glioblastoma stem cells recruits M2 tumour-associated macrophages and promotes malignant growth.* Nat Cell Biol, 2015. **17**(2): p. 170-82.

85. Lu, I.N., et al., *Tumor-associated hematopoietic stem and progenitor cells positively linked to glioblastoma progression.* Nat Commun, 2021. **12**(1): p. 3895.

86. Tatsuno, R., et al., *Pivotal role of IL-8 derived from the interaction between osteosarcoma and tumor-associated macrophages in osteosarcoma growth and metastasis via the FAK pathway.* Cell Death Dis, 2024. **15**(2): p. 108.

87. Comazzetto, S., B. Shen, and S.J. Morrison, *Niches that regulate stem cells and hematopoiesis in adult bone marrow.* Dev Cell, 2021. **56**(13): p. 1848-1860.

88. Pinho, S. and P.S. Frenette, *Haematopoietic stem cell activity and interactions with the niche.* Nat Rev Mol Cell Biol, 2019. **20**(5): p. 303-320.

89. Dobersalske, C., et al., *Cranioencephalic functional lymphoid units in glioblastoma.* Nature Medicine, 2024. **accepted version**.

90. Kokkaliaris, K.D., et al., *Adult blood stem cell localization reflects the abundance of reported bone marrow niche cell types and their combinations.* Blood, 2020. **136**(20): p. 2296-2307.

91. Hernandez-Malmierca, P., et al., *Antigen presentation safeguards the integrity of the hematopoietic stem cell pool.* Cell Stem Cell, 2022. **29**(5): p. 760-775 e10.

92. Doulatov, S., et al., *Hematopoiesis: a human perspective.* Cell Stem Cell, 2012. **10**(2): p. 120-36.

93. Hu, X., et al., *Meningeal lymphatic vessels regulate brain tumor drainage and immunity.* Cell Res, 2020. **30**(3): p. 229-243.

94. Patel, A.A., et al., *The fate and lifespan of human monocyte subsets in steady state and systemic inflammation.* J Exp Med, 2017. **214**(7): p. 1913-1923.

95. Ye, Z., et al., *Phenotypic plasticity of myeloid cells in glioblastoma development, progression, and therapeutics.* Oncogene, 2021. **40**(42): p. 6059-6070.

96. Yang, F., et al., *Synergistic immunotherapy of glioblastoma by dual targeting of IL-6 and CD40.* Nat Commun, 2021. **12**(1): p. 3424.

97. Lee, A.H., et al., *Neoadjuvant PD-1 blockade induces T cell and cDC1 activation but fails to overcome the immunosuppressive tumor associated macrophages in recurrent glioblastoma.* Nat Commun, 2021. **12**(1): p. 6938.

98. Upadhye, A., et al., *Intra-tumoral T cells in pediatric brain tumors display clonal expansion and effector properties.* Nat Cancer, 2024.

99. Tan, A.C., et al., *Management of glioblastoma: State of the art and future directions.* CA Cancer J Clin, 2020. **70**(4): p. 299-312.

100. Bottcher, J.P., et al., *NK Cells Stimulate Recruitment of cDC1 into the Tumor Microenvironment Promoting Cancer Immune Control.* Cell, 2018. **172**(5): p. 1022-1037 e14.

101. Bagley, S.J., et al., *Intrathecal bivalent CAR T cells targeting EGFR and IL13Ralpha2 in recurrent glioblastoma: phase 1 trial interim results.* Nat Med, 2024. **30**(5): p. 1320-1329.

102.   Gelb, S. and M.K. Lehtinen, *Snapshot: Choroid plexus brain barrier.* Cell, 2023. **186**(16): p. 3522-3522 e1.

103.   Flores, C.T., et al., *Lin(-)CCR2(+) hematopoietic stem and progenitor cells overcome resistance to PD-1 blockade.* Nat Commun, 2018. **9**(1): p. 4313.

Acknowledgment

Der Lebenslauf ist in der Online-Version aus Gründen des Datenschutzes nicht enthalten.

Statutory declarations

Declaration:

In accordance with § 6 (para. 2, clause g) of the Regulations Governing the Doctoral Proceedings of the Faculty of Biology for awarding the doctoral degree Dr. rer. nat., I hereby declare that I represent the field to which the topic "*A neuro-immune interface in glioblastoma*" is assigned in research and teaching and that I support the application of Celia Christina Dobersalske.

Essen, 01.07.2024 _Prof. Dr. Björn Scheffler_   _____

Name of the scientific supervisor/member of the University of Duisburg-Essen

Signature of the supervisor/ member of the University of Duisburg-Essen

Declaration:

In accordance with § 7 (para. 2, clause d and f) of the Regulations Governing the Doctoral Proceedings of the Faculty of Biology for awarding the doctoral degree Dr. rer. nat., I hereby declare that I have written the herewith submitted dissertation independently using only the materials listed, and have cited all sources taken over verbatim or in content as such.

Essen, 01.07.2024 _____

Signature of the doctoral candidate

Declaration:

In accordance with § 7 (para. 2, clause e and g) of the Regulations Governing the Doctoral Proceedings of the Faculty of Biology for awarding the doctoral degree Dr. rer. nat., I hereby declare that I have undertaken no previous attempts to attain a doctoral degree, that the current work has not been rejected by any other faculty, and that I am submitting the dissertation only in this procedure.

Essen, 01.07.2024 _____

Signature of the doctoral candidate